

2015-01-28

# Development of the VHP-Female Full-Body Computational Model and Its Applications for Biomedical Electromagnetic Modeling

Janakinadh Yanamadala  
*Worcester Polytechnic Institute*

Follow this and additional works at: <https://digitalcommons.wpi.edu/etd-theses>

---

## Repository Citation

Yanamadala, Janakinadh, "Development of the VHP-Female Full-Body Computational Model and Its Applications for Biomedical Electromagnetic Modeling" (2015). *Masters Theses (All Theses, All Years)*. 142.  
<https://digitalcommons.wpi.edu/etd-theses/142>

This thesis is brought to you for free and open access by [Digital WPI](#). It has been accepted for inclusion in Masters Theses (All Theses, All Years) by an authorized administrator of Digital WPI. For more information, please contact [wpi-etd@wpi.edu](mailto:wpi-etd@wpi.edu).

**Development of the VHP-Female Full-Body Computational Model and Its Applications for  
Biomedical Electromagnetic Modeling**

by

Janakinadh Yanamadala

A Dissertation

Submitted to the Faculty

of the

WORCESTER POLYTECHNIC INSTITUTE

in partial fulfillment of the requirements for the

Master of Science

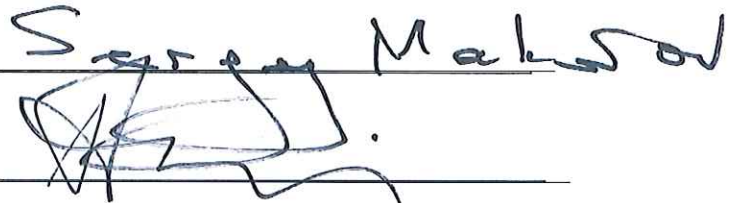
in

Electrical and Computer Engineering

October 2014

APPROVED:

Dr. Sergey Makarov  
Worcester Polytechnic Institute

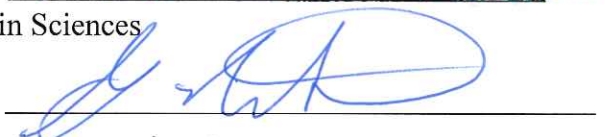


Prof. Ara Nazarian  
Beth Israel Deaconess Medical Center

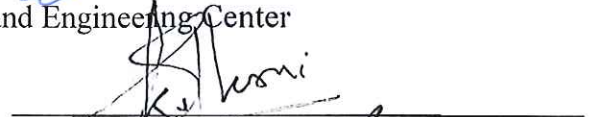
Dr. Mikhail Kozlov  
Max Planck Institute for Human Cognitive and Brain Sciences



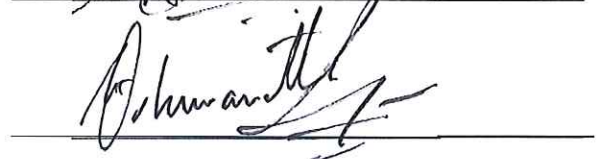
Dr. Gregory Noetscher  
US Army Natick Soldier Research, Development, and Engineering Center



Dr. Shashank Kulkarni  
MathWorks, Inc.



Dr. Vishwanath Iyer  
MathWorks, Inc.



*To my parents and family, for being with me in the journey to pursue my dreams*

# Abstract

Computational modeling offers better insight into a wide range of bioelectrical and biomechanical problems with improved tools for the design of medical devices and the diagnosis of pathologies. Electromagnetic modeling at low and high frequencies is particularly necessary. Modeling electromagnetic, structural, thermal, and acoustic response of the human body to different internal and external stimuli is limited by the availability of numerically efficient computational human models.

This study describes the development to date of a computational full-body human model – Visible Human Project (VHP) – Female Model. Its unique feature is full compatibility both with MATLAB and specialized FEM computational software packages such as ANSYS HFSS/Maxwell 3D. This study also describes progress made to date in using the newly developed tools for segmentation. A visualization tool is implemented within MATLAB and is based on customized version of the constrained 2D Delaunay triangulation method for intersecting objects.

This thesis applies a VHP – Female Model to a specific application, transcranial Direct Current Stimulation (tDCS). Transcranial Direct Current Stimulation has been beneficial in the stimulation of cortical activity and treatment of neurological disorders in humans. The placement of electrodes, which is cephalic versus extracephalic montages, is studied for optimal targeting of currents for a given functional area. Given the difficulty of obtaining in vivo measurements of current density, modeling of conventional and alternative electrode montages via the FEM has been utilized to provide insight into the tDCS montage performance.

An insight into future work and potential areas of research, such as study of bone quality have been presented too.



# Acknowledgement

First and foremost, I would like to express my sincere gratitude to Professor Sergey Makarov for his continuous advice, guidance and encouragement. He motivated me into exploring engineering like I never imagined to. He has inspired me and always been the key to my success. I am fortunate to have an advisor of such immense knowledge and patience. His commitment to students and work has set an example for me to achieve in the remainder of my career.

I thank Dr. Alvaro Pascual-Leone, and Prof. Alexander E. Emanuel, Prof. Naga Korivi for their valuable inputs and exceptional feedback which has significantly shaped my work.

I sincerely thank Dr. Ara Nazarian of Beth Israel Deaconess Medical Center, Dr. Mikhail Kozlov of the Max Planck Institute for Human Cognitive and Brain Sciences, Dr. Gregory Noetscher of US Army Natick Soldier Research, Development, and Engineering Center, Dr. Shanshank Kulkarni of The Mathworks, Dr. Vishwanath Iyer of The Mathworks for their insightful comments and constructive criticism. I am highly esteemed to have a committee of such exceptional stature.

I would also like to thank my fellow team members Aung Thu Htet, Jeffrey Ellion, Saili Maliye, Vishal Kumar Rathi, Aung Htay Win, Anh Le Tran for their valuable thoughts and contributions. Best of luck to you all!

I express thanks to my grandparents, Janakiraman Korivi and Nagakumari Korivi for their blessings. My parents, Sudhir Yanamadala and Padmaja Yanamadala and my brother Siddhardha Yanamadala who have been cheering me and stood by me through the good and bad times. I also would like to thank my aunts Lakshmi Ganesh and Vakula Mukhara for their support and wishes. Finally, I thank my friend Vyshnavi Karna who has always aspired me to believe in myself.

# Table of Contents

Abstract.....	iii
Acknowledgement.....	iv
Table of Contents.....	v
List of Figures.....	ix
List of Tables.....	xiv
Chapter 1 – Introduction.....	01
1.1    Review of available computational human body phantoms and data set.....	02
1.1.1    Visible Human Project® (VHP) dataset.....	02
1.1.2    Whole-body voxel model datasets from NICT of Japan.....	03
1.1.3    Available human body computational models.....	03
1.1.4    Available image segmentation tools.....	05
1.2    Construction of VHP- Female model prior to my thesis and need of a robust MATLAB approach.....	06
1.2.1    Segmentation.....	08
1.2.2    Mesh conditioning/Healing.....	09
1.2.3    Mesh Registration.....	11
1.3    Drawbacks of the prior VHP – Female model which lead to the current VHP – Female Full body model.....	12
1.4    Thesis organization.....	13
References.....	14
Chapter 2 – Triangular surface mesh generation and mesh operations.....	17
2.1    Triangular mesh and its quality.....	18
2.1.1    Arrays of vertices and faces. Structured meshes.....	18
2.1.2    A 3D triangular mesh. 2-Manifold meshes.....	20
2.1.3    Triangle quality and mesh quality.....	22
2.1.4    Triangle size and mesh uniformity.....	23
2.2    Delaunay triangulation and three dimensional volume and surface meshes.....	23
2.2.1    Structured vs. unstructured meshes.....	23
2.2.2    Mesh generation and its properties.....	23
2.2.3    Delaunay triangulation in two dimensions.....	23

2.2.4	Algorithm.....	24
2.2.5	Constrained Delaunay triangulation explained through an example.....	25
2.2.6	Delaunay triangulation in three dimensions (tessellation and tetrahedralization).....	26
2.2.7	Three-dimensional surface mesh generation.....	26
2.2.8	Algorithms for three-dimensional surface mesh generation.....	27
2.3	Mesh operations and transformations.....	28
2.3.1	Topology-preserving mesh transformations.....	28
2.3.2	Necessity of mesh smoothing.....	29
2.3.3	Topology-preserving Laplacian smoothing.....	29
2.3.4	Laplacian smoothing with re-triangulation. Iterative algorithm.....	31
2.3.5	Weaknesses of Laplacian smoothing.....	31
2.3.6	Boolean operations with meshes.....	32
2.3.7	Collision algorithms for 3D surface meshes.....	32
2.3.8	Checking in/out status and finding outer normal vectors for 2-manifold 3D surface meshes..	35
2.4	Adaptive mesh refinement and mesh decimation.....	36
2.4.1	Concept of adaptive mesh refinement.....	36
2.4.2	Example of adaptive mesh refinement with a given error function.....	38
2.4.3	Dependence on the error function and the refinement rate.....	39
2.4.4	Mesh decimation.....	40
	References.....	42
	Chapter 3 – Mesh generation and operation tools developed in MATLAB.....	46
3.1	Segmentation and Surface reconstruction.....	48
3.2	Mesh test for manifoldness.....	48
3.3	Healing the object.....	49
3.4	Mesh Conditioning.....	50
3.5	Mesh intersection algorithm for 2 manifold triangular meshes via constrained 2D Delaunay triangulation.....	51
3.6	Generation of mesh normal.....	54
3.7	Assembly and file format of tissues.....	54
	References.....	55
	Chapter 4 – The VHP – Female computational model to date.....	56
4.1	High definition model.....	56
4.2	Low definition model.....	60

4.3	Deformable human model.....	84
4.4	VHP – Female Model in its current form.....	84
	References.....	86
Chapter 5 – Application example – Transcranial Direct Current Stimulation.....		87
5.1	Simulation setup.....	90
5.1.1	Material properties.....	90
5.1.2	FEM Software and Numerical Accuracy.....	90
5.1.3	Boundary Conditions and Excitation.....	92
5.2	Electrodes and their Montages.....	92
5.2.1	Electrode Model.....	92
5.2.2	Electrode Montages.....	92
5.3	Simulation results for total current density.....	93
5.3.1	Total current density for surfaces of Cerebral Cortex and White Matter.....	93
5.3.2	Total current density for sagittal cut planes.....	93
5.3.3	Total current density for axial cut planes.....	95
5.3.4	Total current density for 45 degree cut planes.....	95
5.3.5	Invariance of relative current densities to changes in Skin properties.....	95
5.4	Quantitative evaluation of vertical and horizontal average current densities.....	100
5.5	Expected electrode voltages and their variations.....	100
5.6	Discussion.....	103
5.6.1	General observations.....	103
5.6.2	Invariance of extracephalic montages.....	105
5.6.3	Validation of results across configurations.....	105
5.6.4	Conclusions.....	105
	References.....	106
Chapter 6 – Future work and potential applications of the VHP – Female Model.....		108
6.1	Potential areas to be explored in tDCS.....	108
6.2	Potential application in non-invasive study of bone quality.....	109
6.2.1	Electric Impedance Tomography (EIT).....	111
6.2.2	Magnetic Induction Tomography.....	111
6.2.3	Electromagnetic Tomography – RF Approach.....	114
6.3	Other applications.....	116
	References.....	117

Summary – .....	118
Appendix A – Direct Current Flow – Boundary conditions and integral equations.....	119
A.1.1 Boundary conditions for a conducting body.....	119
A.1.2 Integral equations for a conducting body except on electrode surfaces.....	120
A.1.3 Complete integral equations for a conducting body. Dirichlet and Neumann boundary conditions.....	121
References.....	123

# List of Figures

Fig. 1.1. Axial cryosection images depicting internal structures within a) the head and b) the abdomen of the Female model from the U.S. National Library of Medicine.....	02
Fig. 1.2. Human-body numerical models developed at NICT. An image of the surface of each model is shown. A volume rendering image of the pregnant woman model is also shown, showing the shape of the fetus. The block size in these models is 2 mm. There are 51 different tissue types of structure in the adult male, female and child models and a total of 56 different tissue types including gestational tissues (fetus, fetal brain, fetal eyes, amniotic fluid, and placenta) [4].....	03
Fig. 1.3. Summary of stages in the development of prior VHP - Female Model.....	06
Fig. 1.4. Imported .raw file a) before re-orientation and b) after re-orientation.....	08
Fig. 1.5. a) Segmentation highlighted for the skull region; b) Mesh constructed for the skull from segmentation.....	09
Fig. 1.6. Pictorial demonstration of closed and open fan mesh.....	10
Fig. 1.7. a) Representation of Lungs registration; b) Registered Lungs in the prior VHP – Female Model [22] .....	12
Fig. 1.8. Prior VHP-F computational human body model depicted in MATLAB (April 2014).....	13
Fig. 2.1. Mesh generation for a planar rectangle.....	18
Fig. 2.2. Mesh generation for a planar rectangle with non-uniform nodes.....	20
Fig. 2.3. a) – A 3D triangular mesh for a sphere with 512 triangles – a 2-manifold mesh; b) – manifold edge; c) – non-manifold edge; d) – non-manifold node.....	21
Fig. 2.4. Radii of the inscribed circle (largest circle contained in the triangle) and the circumscribed circle (smallest circle containing the triangle), respectively, for a right-angled isosceles triangle. $r_{in}$ is called the inradius and $r_{out}$ is the circumradius.....	22
Fig. 2.5.a) – Delaunay triangulation of a set of four nodes; b) – non-Delaunay triangulation of the same node set.....	24
Fig. 2.6. Top – unconstrained Delaunay triangulation of a non-convex polygon; bottom - constrained Delaunay triangulation with boundary edges included into the mesh and removal of unnecessary triangles.....	25

Fig. 2.7. Illustration of three-dimensional surface mesh generation for a pelvic bone from the stack of images for Visible Human (VHP) Project using MATLAB tools. Only a part of the original point cloud, which is the starting point of mesh generation, is shown in Fig. 2.7a.....	26
Fig. 2.8. Two methods of three-dimensional mesh generation. In Fig. 2.8a, only a projection of a tetrahedral mesh is shown.....	27
Fig. 2.9. Concept of Laplacian smoothing.....	30
Fig. 2.10. a) – Ray-triangle intersection for a human eye; b) – segment-triangle intersection.....	34
Fig. 2.11. Three types of intersection of a triangle from a master mesh X with various triangles of a slave mesh Y. Cases #1 and #3 are equivalent if we treat the master and slave meshes as one set of triangles.....	35
Fig. 2.12. Checking in/out status for a 2-manifold mesh. Only mesh cross-section is shown.....	36
Fig. 2.13. Two scenarios of edge subdivisions for triangles with the largest error.....	38
Fig. 2.14. Iterative meshes in the adaptive mesh refinement process. Left column shows the error plot at the previous iteration step; right column – the mesh refined according to this error.....	40
Fig. 2.15. Iterative meshes in the adaptive mesh refinement process for the square plate.....	41
Fig. 2.16. a) - Edge collapse method; b) – vertex removal.....	41
Fig. 3.1. Summary of stages in the development of prior VHP – Female Model.....	46
Fig. 3.2. Illustration of the segmentation/mesh generation workflow: a) – segmentation; b) – stitching of two individual surface meshes; c) – semi-complete surface mesh.....	47
Fig. 3.3. Illustration of non-manifold edges and boundary edges present during healing of intestine displayed through virtual plotting. a) non manifold edge in the interior region of the intestine is not accessible as shown b) - the non-manifold edge is now accessible through virtual plotting of the cut open intestine.....	49
Fig. 3.4. Illustration of the mesh conditioning workflow for pelvic girdle: a) – original surface having approx. 44,000 triangles; b) – Surface mesh after healing and decimation having approx. 6,500 triangles; c) –surface mesh after two iterations of HC smoothing.....	50
Fig.3.5. Three types of triangle intersections between a master mesh X and various triangles of a slave mesh Y. Cases #1 and #3 are equivalent if we treat the master and slave meshes as one set of triangles..	52

Fig.3.6. Image intersection results for white matter and CSF ventricles objects.....	53
Fig.3.7. Illustration of outer normal(s) for the femur bone. Arrow heads depict the direction.....	54
Fig.4.1. VHP-Female model to date: a) – skeleton bones, b) – anterior view of organs and muscles, c) – posterior view of organs and muscles.....	85
Fig. 5.1. Estimate for separate and distinct components of computational model employed for all tDCS simulations, each with individual material properties, including: i) – Artificial skin shell (2 mm thick); ii) – fat layer shell; iii) – muscle volume; iv) bones (left and right acromion, left and right humerus, jaw, ribs, left and right scapula, skull, spine), v) – closed CSF shell; vi) – cerebral cortex (grey matter); vii) – white matter; viii) – cerebellum; ix) – CSF ventricles; x) – eyes and tongue (separate tissues); xi) - sinus cavity, lungs and trachea; xii) – aorta and cava.....	88
Fig. 5.2. Separation of the cerebral cortex into computational sub regions including the frontal lobe, the occipital lobe, the parietal lobe, the primary motor cortex, the somatosensory cortex, and the temporal lobe.....	89
Fig. 5.3. Surface plots of the total current density on the cerebral cortex (row 2) and white matter (row 3). Total current density normalized by the input current density at the electrodes is shown. Column 1 provides results for the cephalic configuration while columns 2 and 3 display the contra-lateral and ipsi-lateral extracephalic results, respectively, using a logarithmic scale.....	94
Fig. 5.4. Depictions of the contralateral supraorbital (i), extracephalic contralateral shoulder (ii), and extracephalic ipsilateral shoulder (iii) cathode montages. Total current density normalized by the input current density at the electrodes is shown projected onto three sagittal planes that progressively travel from the left to right on the model using a logarithmic scale.....	96
Fig. 5.5. Contralateral supraorbital (i), extracephalic contralateral shoulder (ii), and extracephalic ipsilateral shoulder (iii) cathode montages. Total current density normalized by the input current density at the electrodes is shown with surrounding body structures using a logarithmic scale.....	97
Fig. 5.6. Contralateral supraorbital (i), extracephalic contralateral shoulder (ii), and extracephalic ipsilateral shoulder (iii) cathode montages. Total current density normalized by the input current density at the electrodes is shown with surrounding body structures using a logarithmic scale.....	98
Fig. 5.7. Current densities projected onto an axial plane located halfway down the brain for the contralateral supraorbital (i), extracephalic contralateral shoulder (ii), and extracephalic ipsilateral shoulder (iii)	



montages. Total current density normalized by the input current density at the electrodes is shown using a logarithmic scale.....	99
Fig. 5.8. Diagonal cut-plane between the anode and supraorbital cathode displaying normalized total current densities for the contralateral supraorbital (i), extracephalic contralateral shoulder (ii), and extracephalic ipsilateral (iii) montages using a logarithmic scale.....	101
Fig. 5.9. Comparison of tDCS simulation results from Fig. 5.7 as a function of skin conductivity. Total current densities projected onto an axial plane located halfway down the brain for the contralateral supraorbital (i), extracephalic contralateral shoulder (ii), and extracephalic ipsilateral shoulder (iii) montages. Note that the images are employing a logarithmic scale.....	102
Fig. 5.10. Averaged values of the vertical and horizontal current density components for the brain substructures shown in Fig.5.2 and total white and grey matter. Rows 1 and 2 depict results for dry and wet skin, respectively. Ipsi- and contralateral results were identical except in the lower right of Fig. 5.10d....	104
Fig.6.1. Illustration of the pacemaker Altrua60 S 603 is shown in yellow and the leads in green. Note the tissues and organs are hidden for demonstration.....	109
Fig 6.2. Relative dielectric constant of various tissues such as cancellous bone and yellow bone marrow are plotted with respect to frequency.....	110
Fig 6.3. Conductivity of various tissues such as cancellous bone and yellow bone marrow are plotted with respect to frequency.....	110
Fig 6.4. Illustration of EIT applied to the thigh region of the ANSOFT human body containing the femur bone, a) – Shows electrode 1 as anode and electrode 5 as sink/cathode highlighted b) – electrode 2 as anode and 6 as sink.....	111
Fig. 6.5. a) - 3 D view of the selected region of the thigh depicting the coils around the femur of a healthy individual b) - 3 D view of the coils surrounding the femur of a healthy individual for magnetic induction tomography.....	112
Fig.6.6. a) - 3 D view of the selected region of the thigh depicting the coils around the femur for an osteoporotic individual b) - 3 D view of the coils surrounding the Femur for an osteoporotic individual for magnetic induction tomography.....	113
Fig. 6.7. a) - Top view of the selected region of the thigh depicting the coils around the Femur for an osteoporotic individual (highlighted) b) - Top view of the magnetic field surrounding the Femur for an osteoporotic individual.....	114

Fig.6.8. a) - 3D Front view of the selected region of the thigh depicting the antennas around the femur of an individual under examination. B) - 3D Profile view of the selected region of the thigh depicting the antennas around the femur of an individual under examination.....	115
Fig. 6.9. a) - Side view of copper conductor surrounding human thigh. B) - Side view of excitation on the sheet surrounding human thigh.....	115
Fig.6.10. Resonant frequency behavior of standard human tissues for healthy and osteoporotic cases.....	116
Fig.A-1. Evaluation of boundary condition for a conducting body with attached electrodes.....	119
Fig.A-2. Different boundary conditions at the electrode surfaces.....	122

# List of Tables

Table 1.1. List of anatomical whole body models approved by IEEE ICES.....	04
Table 1.2. Inventory of meshes that embody the prior VHP-F model.....	07
Table 4.1. Individual tissues of the VHP-Female model. HD stands for higher-definition meshes; LD stands for lower-definition (decimated and smoothed) meshes. Average triangle area is given. The meshes are given before intersections (if any).....	56
Table 4.2. Selected high definition meshes.....	58
Table 4.3. Table of inventory of low definition tissues.....	61
Table 5.1. Electrical properties employed during Stimulation.....	91
Table 5.2 Convergence of a typical case based on Tetrahedral mesh size.....	91
Table 5.3 – Electrode voltages and dimensionless voltage response. All dimensional voltage data are related to a current source with the electrode normal current density of $J_{in} = 0.08mA/cm^2$ and the total source current of $I_{in} = 25cm^2 \times J_{in} = 2mA$ .....	103

## List of Published Papers

J. Yanamadala, , V.K. Rathi, S. Maliye, H.A. Win, A.L. Tran, M. Zagalskaya, M.K. Kozlov, G.M. Noetscher, A. Nazarian, and S.N. Makarov, “Full-Body Visible Human Project® Female Computational Phantom and Its Applications for Biomedical Electromagnetic Modeling,” *IEEE Signal Processing in Medicine and Biology Symposium*, Temple University, Philadelphia, PA, Dec. 13th 2014.

J. Yanamadala, , V.K. Rathi, S. Maliye, H.A. Win, A.L. Tran, M.K. Kozlov, G.M. Noetscher, A. Nazarian, and S.N. Makarov, “Segmentation of the Visible Human Project® (VHP) Female Cryosection Images within MATLAB® Environment,” *23rd International Meshing Roundtable (IMR23)*, London, England, Oct. 12-15, 2014.

G. M. Noetscher, J. Yanamadala, S. N. Makarov, A. Pascual-Leone, “Comparison of Cephalic and Extracephalic Montages for Transcranial Direct Current Stimulation – A Numerical Study,” *IEEE Transactions on Biomedical Engineering*, vol. 61, no. 9 (Sep. 2014), pp. 2488-2498.

G. M. Noetscher, S. N. Makarov, J. Yanamadala, A. Pascual-Leone, “Theory and simulation of an orthogonal-coil directional beam antenna for biomedical applications,” *2013 IEEE MTT-S International Microwave Workshop Series on RF and Wireless Technologies for Biomedical and Healthcare Applications*, Singapore, Dec. 9-11, 2013

J. Yanamadala, G. M. Noetscher, S. N. Makarov, A. Pascual-Leone, “Comparison of cephalic and extracephalic montages for transcranial direct current stimulation – a numerical study,” *IEEE Signal Processing in Medicine and Biology Symposium*, Polytechnic Institute of New York University, Dec. 7th, 2013.

J. Yanamadala, J. Elloian, G. M. Noetscher, A. T. Htet , S. N. Makarov, F. Scire-Scappuzzo, and A. Pascual-Leone, “FEM-Compatible visible human female segmentation model and its application to in-body and on-body antenna studies,” *37th Antenna Applications Symposium*, Monticello, IL, Sep. 17-19, 2013.

# Chapter 1

## Introduction and Review of the Prior Work

### Importance of computational human-body models

Computational modeling offers tremendous insight into a wide range of bioelectrical and biomechanical problems with improved tools for the design of medical devices and the diagnosis of pathologies. Electromagnetic modeling at low and high frequencies is particularly necessary. Modeling electromagnetic, structural, thermal, and acoustic response of the human body to different internal and external stimuli is limited by the availability of numerically efficient computational human body models. The standard method to create the numerical human body model is 3D image-based meshing of multi-part structures from medical scan data (PET, SPECT, CT, MRI, etc.). Segmentation of datasets is extremely labor intensive. Depending on the images and/or segmentation quality, this effort is often measured by man-months or years for a single model.

The 28 anatomical whole body models currently approved for use by the Institute of Electrical and Electronics Engineers (IEEE) International Committee on Electromagnetic Safety are generally tied to specific, and rather expensive, electromagnetic simulation software packages such as ANSYS, REMCOM, CST MWS, SEMCAD X, FEKO, etc.

The present Chapter starts with review of the available computational human body models in section 1.1. Here, we also describe two open-source image datasets: the VHP<sup>®</sup> dataset and Whole-Body Human Database of Average Japanese Adult Males, Females and Pregnant Woman.

Section 1.2 describes the VHP-Female model available prior to my thesis. These objects were constructed during 2011-2014 and may be used for different research purposes including

- Quantitative accurate modeling of direct current flow due to attached electrodes;
- Modeling human body behavior in the vicinity of powered conductors – electrostatic approximations;
- Quantitative accurate modeling of eddy currents in a human body;
- Modeling of current sources within the human head (EEG applications).

The typical methodologies used for the development of the prior VHP-Female model have been described and the need of an improved methodology is explained.

Section 1.3 describes the drawbacks of the prior VHP – Female model which lead to the current VHP – Female Full body model. Section 1.4 describes the thesis organization. The primary goal of this thesis has been to construct a low definition full body VHP-Female model in MATLAB and develop tools which can be used for segmenting, mesh conditioning and Boolean operations.

The VHP-Female model may be exported into major software packages such as Maxwell 3D of ANSYS by converting them into one of the appropriate CAD formats. In particular, a text NASTRAN format has been used for importing into Maxwell 3D of ANSYS.

## ***1.1. Review of available computational human body phantoms and data sets***

### ***1.1.1. Visible Human Project® (VHP) dataset***

The Visible Human Project® (VHP) [1]-[3] was established in 1989 by the U.S. National Library of Medicine. It was designed to facilitate and encourage greater use of medical images by doctors and engineers. The VHP was initiated to create a detailed digital image library that completely characterizes normal male and female anatomy. Male and female data sets became available in November of 1994 and 1995, respectively.

The male dataset contains cryosection images (slices photographed) predominantly taken in the axial plane of the body at 1 mm intervals. The datasets are also supplemented with MRI and CT images. The MRI images have a pixel resolution of 256 by 256 and each pixel has a gray scale value measured by 12 bit digits. The MRI was used to obtain axial sections of the head and neck and coronal sections of the remaining body. The CT images were taken at intervals of 1mm and have a resolution of 512 by 512 pixels, each pixel measuring the gray scale with 12 bits and coincide with the cryosection data. Every image consists of 2048 by 1216 pixels with each pixel measuring 0.33mm per side. Pixels in each image are expressed with 24 bits of color. There are 1,871 axial anatomical and CT images in the male model making up about 15 gigabytes of data.

The female dataset was similar to the male dataset except that the slices for the imaging was done in intervals of 0.33 mm. This results in the formation of a voxel (a three-dimensional pixelated structure) with 0.33mm length edges and a collection of 5,189 anatomical images or around 40 gigabytes of image data. A representative image is shown in Fig. 1.1.

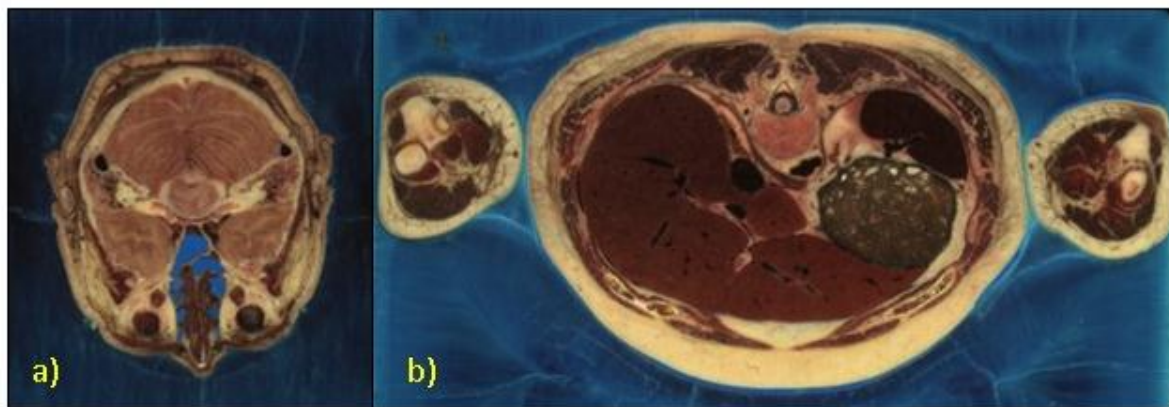


Fig. 1.1. Axial cryosection images depicting internal structures within a) the head and b) the abdomen of the Female model from the U.S. National Library of Medicine.

Some problems were identified in both the male and the female datasets. For example, the brain of the male dataset was slightly swollen and the cadaver was not cut in the standard position. The female specimen contained several pathologies.

### ***1.1.2. Whole-body voxel model datasets from NICT of Japan***

The National Institute of Information and Communications Technology (NICT) of Japan has constructed and made available to the research community a set of whole-body voxel models. The Japanese male and female subject models were first developed and these were used to create the children and pregnant models by using FFD (Free- Form Deformation) method [4] – see Fig. 1.2. These three models have been created using a spatial resolution of  $2\text{mm}^3$  and have over 51 uniquely identified tissues and organs. The model of the pregnant woman includes tissues and structures of the fetus captured from MRI images of a 26 week pregnant woman. Additionally, FFD was used to modify the existing models to be placed in arbitrary positions by moving the joints.

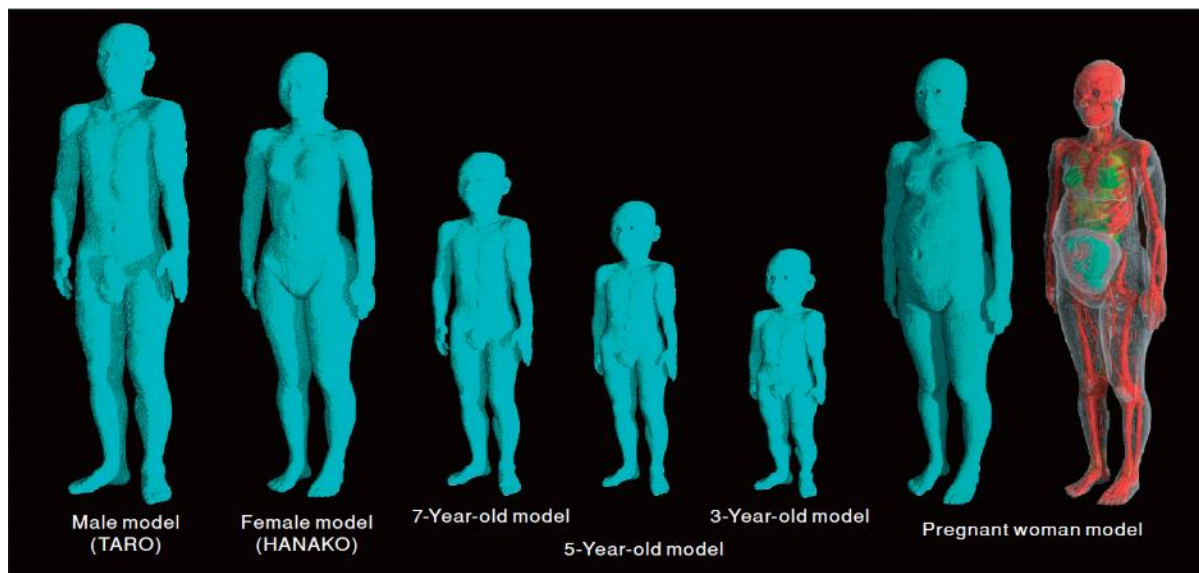


Fig. 1.2. Human-body numerical models developed at NICT. An image of the surface of each model is shown. A volume rendering image of the pregnant woman model is also shown, showing the shape of the fetus. The block size in these models is 2 mm. There are 51 different tissue types of structure in the adult male, female and child models and a total of 56 different tissue types including gestational tissues (fetus, fetal brain, fetal eyes, amniotic fluid, and placenta) [4].

### ***1.1.3. Available human body computational models***

As of October 2014, there are 28 computational human body models that have been approved for use by the Institute of Electrical and Electronics Engineers (IEEE) International Committee on Electromagnetic Safety (ICES) [5], [6]. The Committee's purpose was to standardize anatomical models used for determining the spatial peak specific absorption rate (SAR). Each human body model has its respective data format and voxel resolutions with unique features that can be used

for various applications for specific conditions as in Table 1.1. Of special note is the most recent Virtual Family Suite comprising the largest library of proprietary CAD based phantoms [17]-[19] specifically used in SEMCAD X.

Table 1.1. List of anatomical whole body models approved by IEEE ICES

Model	Height [m]	Weight [kg]	Race	Age	Sex	Data Format, voxel resolution	Comment	Source
Child [7],[8]	1.15	21.7	Caucasian	7 y	F	1.54x1.54x8mm <sup>3</sup>	Small for age	www.cst.com www.ascension.de
Baby [7],[8]	0.57	4.2	Caucasian	8 w	F	0.85x0.85x4mm <sup>3</sup>		www.cst.com www.ascension.de
VoxelMan [9]			Caucasian	adult	M		Head and torso	
Norman [10],[11]			Caucasian	adult	M		only 10 ribs	
Golem [7],[8]	1.76	68.9	Caucasian	38 y	M	2.08x2.08x8mm <sup>3</sup>		www.cst.com www.ascension.de
Visible-human [12]			Caucasian	38 y	M	Various	One testicle only	www.speag.com www.remcom.com
Frank [7],[8]	1.74	95	Caucasian	48 y	M	0.74x0.74x5mm <sup>3</sup>	head and torso	
Donna [7],[8]	1.70	79	Caucasian	40 y	F	1.875x1.875x10mm <sup>3</sup>		www.cst.com www.ascension.de
Helga [7],[8]	1.70	81	Caucasian	26 y	F	0.98x0.98x10mm <sup>3</sup>		www.cst.com www.ascension.de
Irene [7],[8]	1.63	51	Caucasian	32 y	F	1.875x1.875x5mm <sup>3</sup>		
Max[13]			Caucasian	adult	M		VoxelMan adapted to dims. of reference man	
Nagaoka man [14]			Asian	22 y	M	2x2x2mm <sup>3</sup>		
Nagaoka woman [14]			Asian	22 y	F	2x2x2mm <sup>3</sup>		
Naomi [15]			Caucasian	23 y	F			
Katja [16]	1.63	62.3	Caucasian	43 y	F	1.775x1.775x4.8mm <sup>3</sup>	Pregnant (24 <sup>th</sup> week)	www.cst.com www.ascension.de
Roberta [17]	1.08	17.6	Caucasian	5 y	F	CAD, 0.5x0.5x0.5mm <sup>3</sup> or better		www.itis.ethz.ch
Thelonious [18]	1.17	19.5	Caucasian	6 y	M	CAD, 0.5x0.5x0.5mm <sup>3</sup> or better		www.itis.ethz.ch
Eartha [17]	1.35	30.3	Caucasian	8 y	F	CAD, 0.5x0.5x0.5mm <sup>3</sup> or better		www.itis.ethz.ch
Dizzie [17]	1.40	26.2	Caucasian	8 y	M	CAD, 0.5x0.5x0.5mm <sup>3</sup> or better		www.itis.ethz.ch



Billie [18]	1.46	35.6	Caucasian	11 y	F	CAD, 0.5x0.5x0.5mm <sup>3</sup> or better		<a href="http://www.itis.ethz.ch">www.itis.ethz.ch</a>
Louis [17]	1.69	49.9	Caucasian	14 y	M	CAD, 0.5x0.5x0.5mm <sup>3</sup> or better		<a href="http://www.itis.ethz.ch">www.itis.ethz.ch</a>
Ella [18]	1.60	58	Caucasian	26 y	F	CAD, 0.5x0.5x0.5mm <sup>3</sup> or better		<a href="http://www.itis.ethz.ch">www.itis.ethz.ch</a>
Duke [18]	1.74	70	Caucasian	34 y	M	CAD, 0.5x0.5x0.5mm <sup>3</sup> or better		<a href="http://www.itis.ethz.ch">www.itis.ethz.ch</a> <a href="http://www.virtualman.info">www.virtualman.info</a>
Ella (pregnant) [19]	1.60		Caucasian	26 y	F	CAD	3 <sup>rd</sup> , 7 <sup>th</sup> and 9 <sup>th</sup> gestational month	<a href="http://www.speag.com">www.speag.com</a>
Fats	1.78	120	Caucasian	37 y	M	CAD		<a href="http://www.speag.com">www.speag.com</a>
Chinese Male [20]	1.72	63.05	Asian	35 y	M	1x1x1mm <sup>3</sup>		
Chinese Female [20]	1.62	53.5	Asian	22 y	F	1x1x1mm <sup>3</sup>		
VHP-F [20]-[23]	1.73	~75	Caucasian	~59 y	F	Variable. Average: 2x2x2 mm <sup>3</sup>	Visible Human Data Source.	<a href="http://www.nevaelectromagnetics.com/MWO.html">www.nevaelectromagnetics.com/MWO.html</a>

Most of the available models are tied to private structural modeling software such as SEMCAD X, CST and REMCOM etc. Aarkid Limited created the human body phantom for ANSYS HFSS (USA) which is reasonably accurate but lacks the cerebrospinal fluid which is a vital component when studying the human head and brain. Both the commercial and academic licenses of the models are currently expensive ranging \$1,000-\$20,000 [22]

Hence most present models are proprietary, tailor made for corresponding software packages and there is a need for body models which are platform-independent. A platform-independent model can be used for custom based modeling problems.

#### ***1.1.4. Available image segmentation tools***

There is a plethora of image segmentation software packages available with a large database of vendors located at the Internet Analysis Tools Registry (IATR) [24]. This database, which is supported by the Human Brain Project (HBP), provides a listing and reviews of 197 distinct image segmentation and registration tools designed for a broad number of applications, including cerebral aneurysm detection, neuroradiology, bio-imaging, surgical planning and anatomical informatics. This international group of contributors range from academic institutions (Massachusetts Institute of Technology, University of Pennsylvania, John Hopkins University) to commercial entities (The MITRE Corporation) and hospitals (Massachusetts General Hospital, Brigham and Women's Hospital) to national laboratories (Los Alamos National Lab). Some of these tools are supported not only by the HBP but also Neuroimaging Informatics Technology Initiative (NIfTI), which is

jointly sponsored by the National Institute of Mental Health and the National Institute of Neurological Disorders and Stroke.

One of the major tools developed in conjunction with the VHP dataset and utilized to create the prior VHP triangular surface meshes [22], [25], was the open source program Insight Toolkit-SNAP (ITK-SNAP) [26], which enables the analysis of three dimensional image stacks and simultaneous segmentation of images in the axial, coronal, and sagittal body planes via manual and automatic methods. The user may manually trace organs, tissues and other structures. The end result is a stereolithography (STL) file describing the surface of the segmented region as a dense triangular mesh.

Among the commercially available products, ScanIP, a product of Simpleware Ltd. is used for automated triangular mesh generation and it costs around \$ 26,000 with the all necessary modules [27]-[28].

### ***1.2. Construction of VHP- Female model prior to my thesis and need of a robust MATLAB approach***

This study presents the construction and development of the VHP- Female model prior to my thesis [22]. Data from Visible Human Project® described in section 1.2.1 was utilized to create high fidelity computational objects. The procedure for the development can be divided into three major

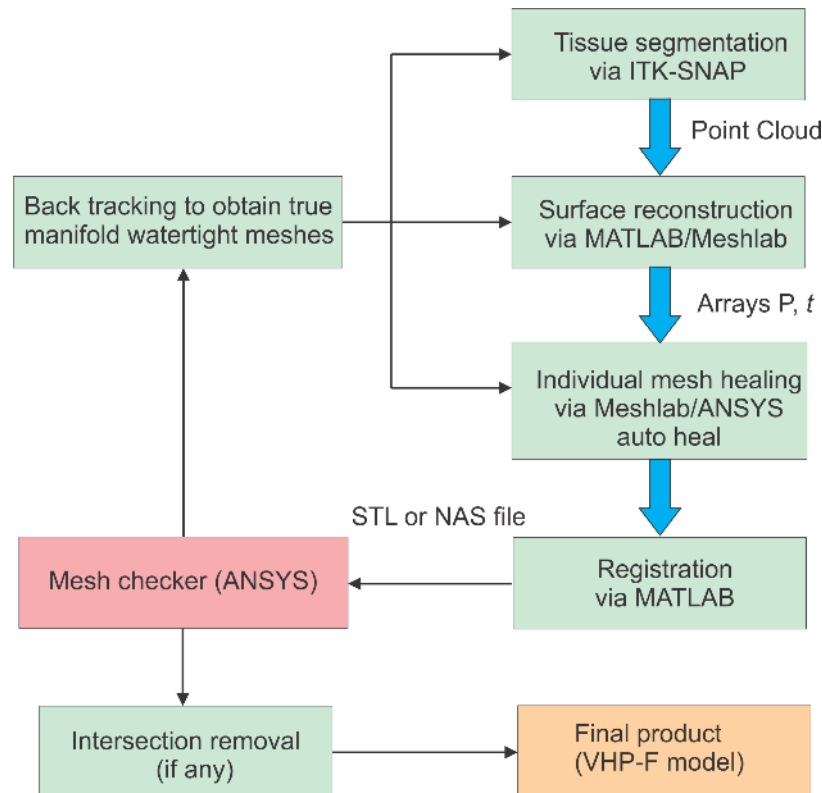


Fig. 1.3. Summary of stages in the development of prior VHP - Female Model

blocks namely segmentation, mesh conditioning and registration. The complete development process is shown in Fig. 1.3. Cryosection images obtained from the data undergo fine segmentation to create stereolithography (STL) files. Mesh conditioning was performed on these files to create high quality true manifold watertight meshes. The meshes obtained were then registered to be anatomically accurate. The process of obtaining a true manifold watertight mesh is an iterative process. The obtained point cloud/STL file after segmentation has to be refined and conditioned to be a true manifold mesh. The obtained organs are then registered to be anatomically accurate. Then the meshes/objects are made to pass the ANSYS Mesh checker, with the option “Check level – Strict” which denotes the tolerance levels. The final objects developed are suitable for both voxel based modeling (via Finite-difference time-domain (FDTD) method) and for finite element method (FEM) modeling.

A total of 33 parts including major organs, bones and blood vessels were present in the VHP-Female Model created. A comprehensive list containing name, number of triangles and material can be found in Table 1.2. [22].

Table 1.2. Inventory of organs that embody the prior VHP-F model

Material	Structure	Triangles	Nodes	Material	Structure	Triangles	Nodes
Blood	Aorta	149,876	74,998	Air	Sinus	1,860,572	929,926
	Superior Vena Cava	270,928	135,729	Cerebellum	Cerebellum	557,708	278,856
Cancellous Bone	Ribs	1,379,396	690,555	Cerebrospinal Fluid	CSF Shell	2,992	3,089
	Skull	9,190,392	4,593,938		Ventricles	832	416
	Spine	781,482	391,001	Eyes	Eye (Left)	52,292	26,148
Cortical Bone	Acromion (Left)	524	320		Eye (Right)	51,556	25,780
	Acromion (Right)	590	346	Infiltrated Fat	Fat Shell	205,462	616,386
	Humerus (Left)	132,127	66,748	Heart Muscle	Heart	206,296	103,150
	Humerus (Right)	137,521	68,097	Intestine	Intestinal Tract	18,462	9,188
	Jaw	436,828	1,310,484	Kidney	Kidney (Left)	27,149	13,577
	Forearm Bones	2,000	1,000		Kidney (Right)	26,611	13,307

Material	Structure	Triangles	Nodes	Material	Structure	Triangles	Nodes
	Scapula (Left)	210,954	105,675	Liver	Liver	130,088	65,046
	Scapula (Right)	206,776	103,581	Inflated Lung	Lung	1,248,744	624,750
	Teeth	58,028	29,056	Muscle	Muscle Shell	20,365	11,381
Grey Matter	Cerebral Cortex	2,173,224	1,086,612	Skin	Dry Skin	64,000	32,004
White Matter	Inner Brain	3,730,972	1,865,332	Tongue	Tongue	354,184	1,062,552
Stomach	Stomach	557,774	278,889				

The following sections briefly describe the segmentation, mesh conditioning and registration process followed in the prior VHP –Female model [25].

### 1.2.1. Segmentation

Insight Segmentation and Registration Toolkit (ITK - Snap) discussed in section 1.1.4 was used for segmentation. The input file is a stack of Grey scale cryosection images in .raw format which was compiled using ImageJ software.

The .raw file was imported into ITK – Snap. The header size, image dimensions, voxel spacing, voxel representation and byte alignment have to be assigned. The values used can be found in [25]. The loaded data has to be re-oriented and this configuration has to be maintained throughout the process of Segmentation. The orientation of the image stack is illustrated in Fig. 1.4. The polygon tool was used for the manual segmentation. ITK – Snap also has in built semi-automatic and

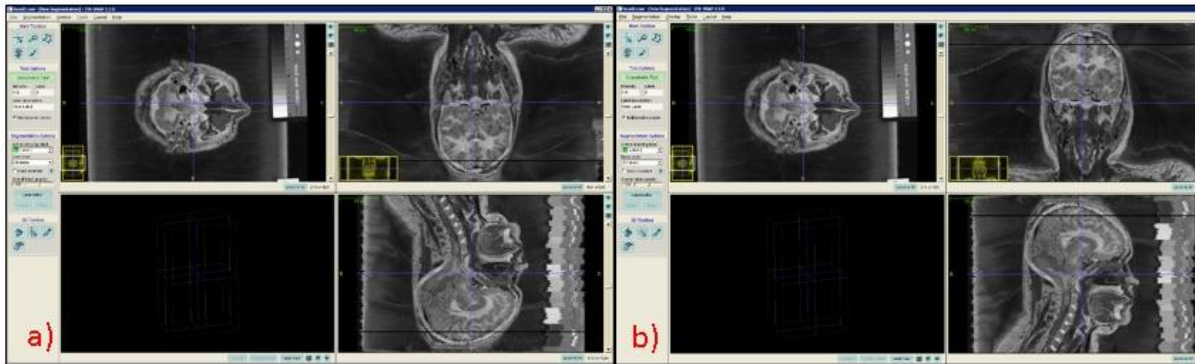


Fig. 1.4. Imported .raw file a) before re-orientation and b) after re-orientation.

automatic segmentation features. This manual segmentation process, while time consuming, results in very fine triangular meshes.

The segmentation can be done in over a period of time and has to be saved as an image in NIfTI format (.nii file), which can be retrieved. After the segmentation process is completed, the “export as surface mesh” was used to save the mesh as a STL file. Fig.1.5. illustrates the segmented area in red for the skull and the respective STL mesh obtained. The exported meshes have a resolution of 1mm.

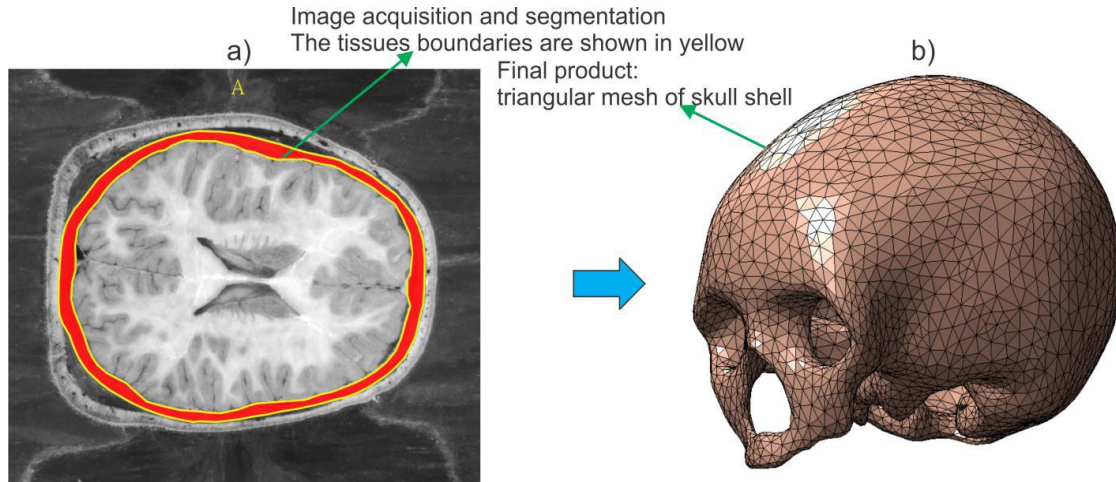


Fig. 1.5 a) Segmentation highlighted for the skull region. b) Mesh constructed for the skull from segmentation.

The STL file created is high definition, complex, and unclear. Therefore, it has to undergo mesh conditioning, which will be discussed in section 1.2.2.

The process of segmentation is extremely time consuming and is usually mentioned in man years or man months. ITK-Snap does not allow the user to skip and segment selected slides. If the user skips slides then the resulting STL file would have holes and would require additional efforts to repair it. The resulting STL file is normally very dense for example, the skull had 781,482 triangles. Commercial solvers such as ANSYS can mesh up to 150, 000 triangles with a reasonable computational resources within a feasible time. Hence the obtained STL file has to be conditioned to create meshes having triangle number within desired limit [22]. The segmentation time could be significantly reduced from man weeks to man days if we can have a custom MATLAB script which would enable us to pick selected images and create low definition meshes to begin with.

### **1.2.2. Mesh conditioning/ Healing**

The high definition STL files obtained from segmentation had a large number of nodes and were non-manifold. Therefore the meshes need to be conditioned to obtain high quality manifold meshes with reasonable number of triangles for computational feasibility. A mesh is a manifold if (1) each edge is incident to only one or two faces and (2) the faces incident to a vertex form a closed or an

open fan [29]. The closed and open meshes are represented in Fig. 1.6. The healing process and concepts will be explained in detail in Chapter 02.

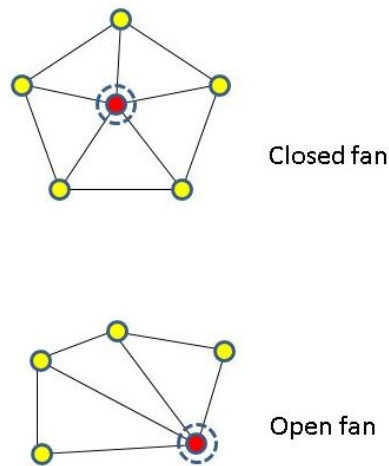


Fig.1.6. Pictorial demonstration of closed and open fan mesh.

Most of the mesh conditioning was performed using custom using MeshLab [30]. MeshLab is an open source and portable system for the processing and editing of unstructured 3D triangular meshes. Custom MATLAB scripts were also used for conditioning.

The custom MATLAB conditioning code performed the algorithm for HC Laplacian smoothing [31]. This resulted in smooth meshes with high triangular quality. The conditioning also included fixing non manifold edges and vertices using MeshLab.

MeshLab was used to perform operations such as mesh cleaning, repairing, smoothing, re-meshing, mesh decimation and reconstruction. The high definition STL files can have holes which were filled using Poisson reconstruction [32]. After the reconstruction was performed, the meshes were smoothed and the number of nodes increased. The nodes or the number of triangles was reduced using Quadrature Edge Collapse Decimation [33]-[36] available in MeshLab. Further, surface preserve Laplacian smoothing and HC Laplacian smoothing have been used for smoothing operation. Example values of the parameters used can be found in [25]. MeshLab has mesh stitching features which were used to form a single layer from different meshes and then reconstruction was applied.

The point could obtained from was reconstructed using the excellent script MyRobustCrust.m written by Dr. Luigi Giaccari based on ball-pivoting algorithm. More on this is described in Chapter 02.

The final object after the conditioning, is imported into ANSYS Mesh check at “strict” level. The Strict entity check setting enforces the tightest tolerance for model faults. If the mesh is not “good”, further conditioning is required and becomes a back tracking case. Hence, once the mesh

passes the “strict” level check in the mesh analyzer we confirm that it is a true manifold mesh and is suitable for both voxel based modeling and for FEM modeling.

The final models were then registered in the human body as described in section 1.2.3 to obtain an anatomically accurate VHP - female model.

The auto healing available in ANSYS played an important role to achieve manifold meshes. The healing option can heal certain non-manifold features and has its limitations. The auto healing is quite handy as it is in-built in ANSYS and the manual healing allows to relax the tolerances. These features are not effective in healing targeted regions and healing certain errors.

Both MeshLab and the auto healer in ANSYS have graphic user interfaces which are user friendly but also give user limited control over different variables and parameters. A worthy mention would be, ANSYS checker which shows the location of the error but does not provide the user to perform targeted healing. Hence this process is very time consuming and a need for more user interactive tools is required. Chapter 03 covers the tools which were developed in MATLAB for mesh conditioning.

### ***1.2.3. Mesh Registration***

Registration is the process of integrating all the organs/bones into their anatomically precise positions. The organs obtained after the mesh conditioning, are then accurately orientated with reference to the image data. The custom MATLAB registration script was designed to perform registration.

Mesh transformations such as shifting, rotation, scaling were used for registration and were done in MeshLab/MATLAB.

Why does mesh registration involve transformations if all the meshes were segmented/generated ITK-Snap? To understand, ITK – Snap has a threshold on the size of the .raw file it imports. Hence the number of images is limited and they have to be cropped to accommodate more images at a time before the stack of images (.raw file) is made. This resulted in each .raw file having a co-ordinate system of its own. Secondly the VHP – Female model was given a unique co-ordinate system. The X and Y origin co-ordinate is the geometrical center of the image used for segmentation and the Z origin co-ordinate was at the image where external auditory meatus appears (image – avf1152a.png). These three factors not only result in translational shift and rotation but can also involve scaling in all X, Y and Z directions. The computation of translational shift, orientation shift and the scaling is based on the ITK – Snap setting for each .raw file and is demonstrated in [25]. The nodes from the Lungs have been plotted on the image to confirm the registration [22] as depicted in Fig. 1.7.

The whole process of registration would be redundant if we would have a single platform for segmentation where there is no limit on the number of images selected and if we could predefine



the co-ordinate system. This has been achieved by using MATLAB scripts in this thesis. The MATLAB script developed for segmentation takes into account the limitations and results in objects requiring no registration process.

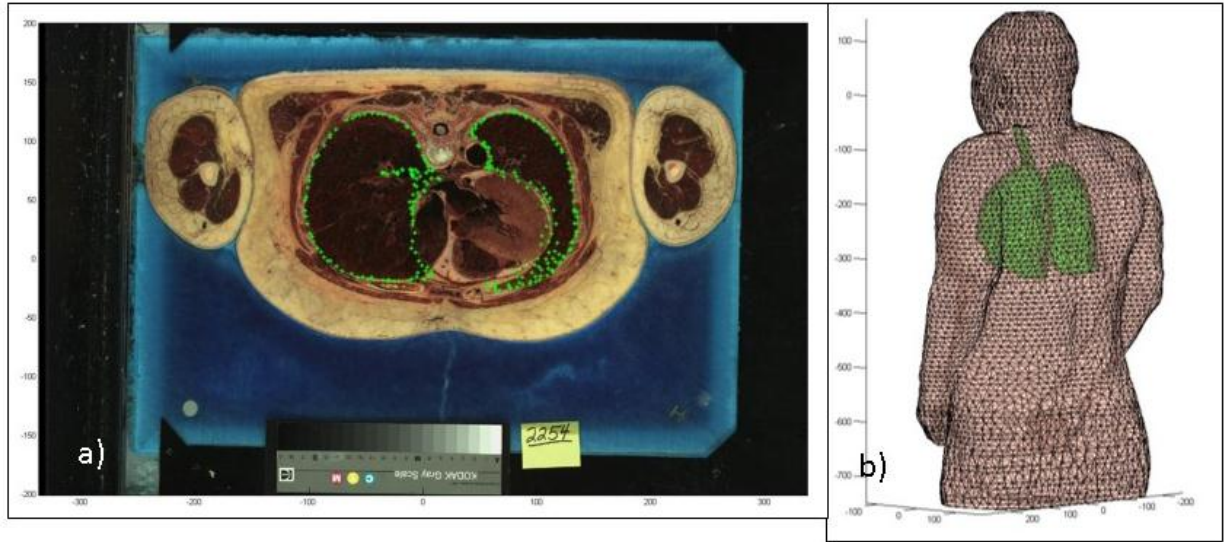


Fig.1.7. a) Representation of Lungs registration b) Registered Lungs in the prior VHP – Female Model [22] .

### ***1.3. Drawbacks of the prior VHP – Female model which lead to the current VHP – Female Full body model***

The VHP – Female model which was developed prior to my thesis is shown in Fig. 1.8. The development of this model spanned from 2011 - 2014 and has its advantages and disadvantages. It is noteworthy that it has the cerebrospinal fluid (CSF) which is difficult to create using the typical process of segmentation and is critical for brain and head studies [22]. We discuss the importance of CSF in transcranial direct current stimulation (Chapter 05).

As for the negative aspects, in this model all the intersections and other Boolean operations were dealt in ANSYS which introduced a huge number of triangles which in turn increases the computational time of a certain simulation. The low resolution model of the previous VHP – Female model was optimized such the number of triangles would not over load the computational resources. If a full body model is created with similar resolution we can expect the triangle number to be doubled and hence the increase the computational time by  $O(n^2)$ . Other important aspect which made it unsuitable for MRI based simulations was that the arms and torso were attached. This was a fundamental flaw of the model as it is anatomically incorrect. Hence the outer shape of the model had to be remodeled completely.



This thesis comprehensively encompasses the above aspects with the use of MATLAB scripts. The MATLAB tools were developed from 2013 – 2014 and were instrumental in building the full human body model [37].

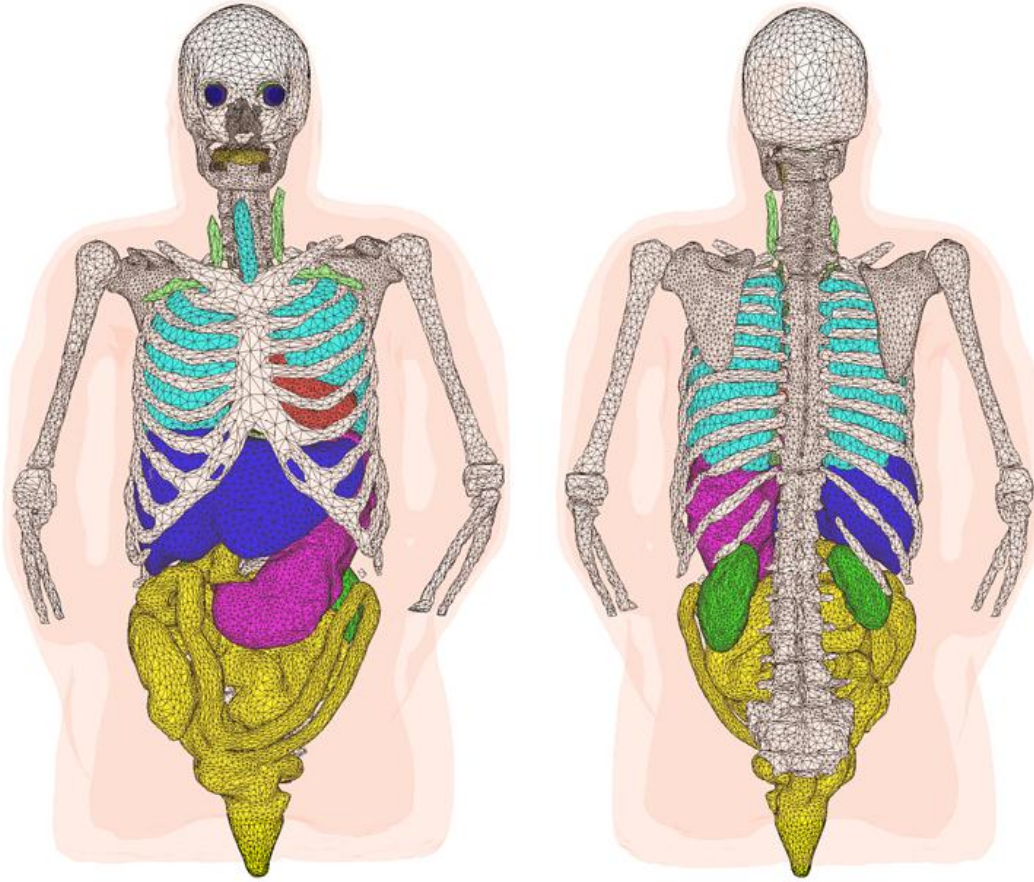


Fig. 1.8. Prior VHP-F computational human body model depicted in MATLAB (April 2014).

#### ***1.4 Thesis organization***

This thesis has been divided into five chapters. Chapter 02 introduces the necessary theory, the basic back ground for surface triangular mesh construction. Chapter 03 discusses in detail the tools developed in MATLAB and Chapter 04 presents the current VHP – Female model and the encompassing tissues. Chapter 05 describes the application of VHP – Female model in the study of Transcranial Direct Current Stimulation, a low frequency application. To conclude, several potential applications and future work are presented in Chapter 06.

## References

- [1]. M.J. Ackerman, "The visible human project," *Proceedings of the IEEE*, vol. 86, 1998, pp. 504-511.
- [2]. U.S. National Library of Medicine. The Visible Human Project® Online: [http://www.nlm.nih.gov/research/visible/visible\\_human.html](http://www.nlm.nih.gov/research/visible/visible_human.html)
- [3]. P. A. Yushkevich, J. Piven, H. C. Hazlett, R. G. Smith, S. Ho, J. C. Gee, and G. Gerig, "User-guided 3D Active Contour Segmentation of Anatomical Structures: Significantly Improved Efficiency and Reliability," *NeuroImage*, vol. 31, pp. 1116-28, 2006.
- [4]. Whole-Body Human Database of Japanese Average Adult Males, Females and Pregnant Woman. Online: <http://www.nict.go.jp/>; see also [http://www.nict.go.jp/en/pdf/NICT\\_NEWS\\_1003\\_E.pdf](http://www.nict.go.jp/en/pdf/NICT_NEWS_1003_E.pdf)
- [5]. IEEE International Committee on Electromagnetic Safety: Technical Committee 34: Wireless Handset SAR Certification Brochure. Online: <http://grouper.ieee.org/groups/scc34/sc2/>
- [6]. IEEE International Committee on Electromagnetic Safety: Technical Committee 34: List of approved human phantoms. Online: <http://grouper.ieee.org/groups/scc34/sc2/wg2/available%20human%20models.doc>
- [7]. N. Petoussi-Henss, M. Zankl, U. Fill, D. Regulla, D., "The GSF family of voxel phantoms," *Physics in Medicine and Biology*, vol. 47, pp. 89–106, 2002.
- [8]. M. Zankl, N. Petoussi-Henss, U. Fill, D. Regulla, "The application of voxel phantoms to the internal dosimetry of radionuclides," *Radiation Protection Dosimetry*, vol. 105, pp. 539–548, 2003.
- [9]. G. Zubal, C. Harrel, E. Smith, Z. Ratner, G. Gindi, P. Hoffer, "Computerized three-dimensional segmented human anatomy," *Medical Physics*, vol. 21, pp. 299–302, 1994.
- [10]. P.J. Dimbylow, "FDTD calculations of the whole-body averaged SAR in an anatomically realistic voxel model of the human body from 1 MHz to 1 GHz," *Physics in Medicine and Biology*, vol. 42, pp. 479–490.
- [11]. D.G. Jones, "A realistic anthropomorphic phantom for calculating organ doses arising from external photon irradiation," *Radiation Protection Dosimetry*, vol. 72, pp. 21–29, 1997.
- [12]. V. Spitzer, M. J. Ackerman, A. L. Scherzinger, and D. Whitlock, "The visible human male: a technical report", *Journal of the American Medical Informatics Association*, vol. 3, no. 2, pp. 118, 1996.
- [13]. R. Kramer, J.W. Vieira, H.J. Khoury, F.R.A. Lima, D. Fuelle, "All about MAX: a male adult voxel phantom for Monte Carlo calculations in radiation protection dosimetry," *Physics in Medicine and Biology*, vol. 48, pp. 1239–1262, 2003.
- [14]. T. Nagaoka, S. Watanabe, K. Sakurai, E. Kuneida, S. Watanabe, M. Taki, Y. Yamanka, "Development of realistic high resolution whole-body voxel models of Japanese adult male and female of average height and weight, and application of models to radio-frequency electromagnetic-field dosimetry," *Physics in Medicine and Biology*, vol. 49, pp. 1–15, 2004.
- [15]. P.J. Dimbylow, "Development of the female voxel phantom, NAOMI, and its application to calculations of induced current densities and electric fields from applied low frequency magnetic and electric fields," *Physics in Medicine and Biology*, vol. 50, pp. 1047–1070, 2005.
- [16]. J. Becker, M. Zankl, U. Fill, and C. Hoeschen, "Katja – the 24th week of virtual pregnancy for dosimetric calculations", *Polish Journal of Medical Physics and Engineering*, vol. 14, no. 1, pp. 13-19, 2008.
- [17]. A. Christ, G. Schmid, R. Djafarzadeh, R. Überbacher, S. Cecil, M. Zefferer, E. Neufeld, M. Lichtsteiner, M. Bouterfas, and N. Kuster "Numerische Bestimmung der Spezifischen

- Absorptionsrate bei Ganzkörperexposition von Kindern: Abschlußbericht”, Technical Report, IT’IS Foundation, Zürich, Switzerland, July, 2009.
- [18]. A. Christ, W. Kainz, E.G. Hahn, K. Honegger, M. Zefferer, E. Neufeld, W. Rascher, R. Janka, W. Bautz, J. Chen, B. Kiefer, P. Schmitt, H.P. Hollenbach, J.X. Shen, M. Oberle, D. Szczerba, A. Kam, J.W. Guag, N. Kuster, “The Virtual Family – Development of Surface Based Anatomical Models of two Adults and two Children for Dosimetric Simulations”, *Physics in Medicine and Biology*, vol. 55, N23, 2010.
  - [19]. E. Cabot, A. Christ, B. Bühlmann, M. Zefferer, N. Chavannes, G. C. van Rhoon, and N. Kuster, “Quantification of the RF exposure of the foetus using anatomical CAD models in three different gestational phases”, submitted.
  - [20]. T. Wu, L. Tan, Q Shao, C. Zhang, C. Zhao, Y. Li, E. Conil, A. Hadjem, J. Wiart, B. Lu, L. Xiao, N. Wang, Yi Xie, and S. Zhang, “Chinese adult anatomical models and the application in evaluation of RF exposures”, *Physics in Medicine and Biology*, vol. 56, pp. 2075-2089, 2011.
  - [21]. J.M. Elloian, G.M. Noetscher, S.N. Makarov, and A. Pascual-Leone, “Continuous wave simulations on the propagation of electromagnetic fields through the human head,” *IEEE Trans. Biomedical Engineering*, vol. 61, no. 6, pp. 1676-1683, June 2014.
  - [22]. G.M. Noetscher, *The VHP-F Computational Phantom and its Applications for Electromagnetic Simulations*, PhD Thesis, Worcester Polytechnic Institute, Apr. 2014, 307 p.
  - [23]. G. M. Noetscher, J. Yanamadala, S. N. Makarov, and A. Pascual-Leone, “Comparison of cephalic and extracephalic montages for Transcranial Direct Current Stimulation - A numerical study,” *IEEE Trans. Biomedical Engineering*, vol. 62, 2014.
  - [24]. C. Haselgrove, "Internet Analysis Tools Registry." *Home*. N.p., n.d. Web. 12 Jan. 2014, <http://www.cma.mgh.harvard.edu/iatr/>
  - [25]. J. Yanamadala, J. Elloian, G.M. Noetscher, A.T. Htet, S.N. Makarov, F. Scire- Scappuzzo, A. Pascual-Leone, “ FEM-Compatible Visible Human Female Segmentation Model and Its Application to In-Body and On-Body Antenna Studies”, *Antenna Applications Symp.*, Monticello, IL, 2013, pp. 340- 359.
  - [26]. P. A. Yushkevich, J. Piven, H. C. Hazlett, R. G. Smith, S. Ho, J. C. Gee, G. Gerig, User-guided 3D Active Contour Segmentation of Anatomical Structures: Significantly Improved Efficiency and Reliability, *NeuroImage*. vol. 31 (2006) 1116-28.
  - [27]. Geng, K., Segars, P., Cockram, S., et. al., “Workflow for creating a simulation ready virtual population for finite element modeling,” *Proc. ASME/FDA 2013 1st Annual Frontiers in Medical Devices: Applications of Computer Modeling and Simulation, FMD2013*, Sep. 11-13, 2013, Washington, DC.
  - [28]. Young, P.G., Beresford-West, T.B.H., Coward, S.R.L, et. al., “An efficient approach to converting 3D image data into highly accurate computational models,” *Philos Trans A Math Phys Eng Sci*. A-13; vol. 366 (1878):pp. 3155-73, 2008.
  - [29]. Mesh basics by Dr. Ching – Kuang Shene. Online: <http://www.cs.mtu.edu/~shene/COURSES/cs3621/SLIDES/Mesh.pdf>
  - [30]. Online: <http://meshlab.sourceforge.net>
  - [31]. J. Vollmer, R. Mencl, and H. Müller, “Improved Laplacian smoothing of noisy surface meshes,” *Computer Graphics Forum*, vol. 18, no. 3, Sep. 1999, pp. 131-138.
  - [32]. M. Kazhdan, M. Bolitho, H. Hoppe, “Poisson Surface Reconstruction”, *Eurographics Symposium on Geometry Processing*, 2006.

- [33]. J. Rossignac and P. Borrel, "Multi-resolution 3D approximations for rendering complex scenes," in *Geometric Modeling in Computational Graphics*, pp. 455-465, Springer Verlag, Eds. B. Falcidieno and T.L. Kunii, Genova, Italy, Jun 28-Jul 2, 1993.
- [34]. H. Hoppe, "Progressive meshes," *SIGGRAPH 1996 Proceedings*, Aug. 1996, pp. 99-108.
- [35]. A. Gueziec, "Surface simplification with variable tolerance," *2<sup>nd</sup> Annual International Symposium on Medical Robotics and Computer Assisted Surgery*, Nov. 1995, pp. 132-139.
- [36]. P.S. Heckbert, M. Garland, "Optimal triangulation and quadric-based surface simplification," *Computational Geometry*, vol. 14, 1999, pp. 49-65.
- [37]. J. Yanamadala, V. K. Rathi, S. Maliye, H. A. Win, A. L. Tran, M. K. Kozlov, G. M. Noetscher, A. Nazarian, and S. N. Makarov, Segmentation of the Visible Human Project® (VHP) Female Cryosection Images within MATLAB® Environment, 23rd International Meshing Roundtable (IMR23), London, England, Oct. 12-15, 2014.

## Chapter 2

# Triangular surface mesh generation and mesh operations

### Introduction

This Chapter reviews basic facts related to triangular surface mesh generation for electromagnetic computational problems. Understanding mesh generation, mesh properties, possible mesh errors, and adaptive mesh refinement process is an important part of any intelligent electromagnetic computations.

Section 2.1 defines a triangular mesh, discusses structured and unstructured meshes, introduces the meaning of a 2-manifold mesh, and gives the metrics for triangle quality, triangle size, and mesh uniformity.

Section 2.2 introduces the basic 2D Delaunay triangulation algorithm. It discusses unconstrained and constrained Delaunay triangulation. It also introduces three-dimensional tetrahedral mesh generation. Perhaps the most important part of this section is three-dimensional surface mesh generation applied in particular to biomedical imaging.

Section 2.3 begins with a discussion of basic mesh operations (translation, rotation, scaling). The need for mesh smoothing is introduced. Laplacian smoothing is then studied.

Section 2.3 introduces a simple mesh transformation techniques. Different types of smoothing are discussed and Laplacian smoothing is introduced. Section 2.3 finishes with the description of two “collision” algorithms: ray-triangle intersection and segment-triangle intersection. These algorithms have a broad application space. For example, they may be used to find surface normal vectors and evaluate intersections of two distinct triangular surface meshes, triangle by triangle. The latter method is the foundation for performing Boolean operations on realistic surface meshes of human tissues.

Section 2.4 introduces perhaps the most important computational aspect of mesh transformation: the process of adaptive mesh refinement. We discuss the physical motivation for adaptive mesh refinement first. Then, we consider a basic example with an artificial error function and model the entire adaptive mesh refinement procedure. Laplacian smoothing may be employed to maintain mesh quality.

## 2.1. Triangular mesh and its quality

### 2.1.1. Arrays of vertices and faces. Structured meshes

#### Arrays of vertices and faces

A triangular surface mesh is the base of any surface representation including various numerical methods in electrical and biomedical engineering, computer graphics, etc. Consider a planar rectangle on the size  $a \times b$  in the  $xy$ -plane shown in Fig. 2.2. The goal is to “cover” its surface with triangles – *simplexes* in 2D. Many ways of doing so exist. One such way is shown in Fig. 2.1.

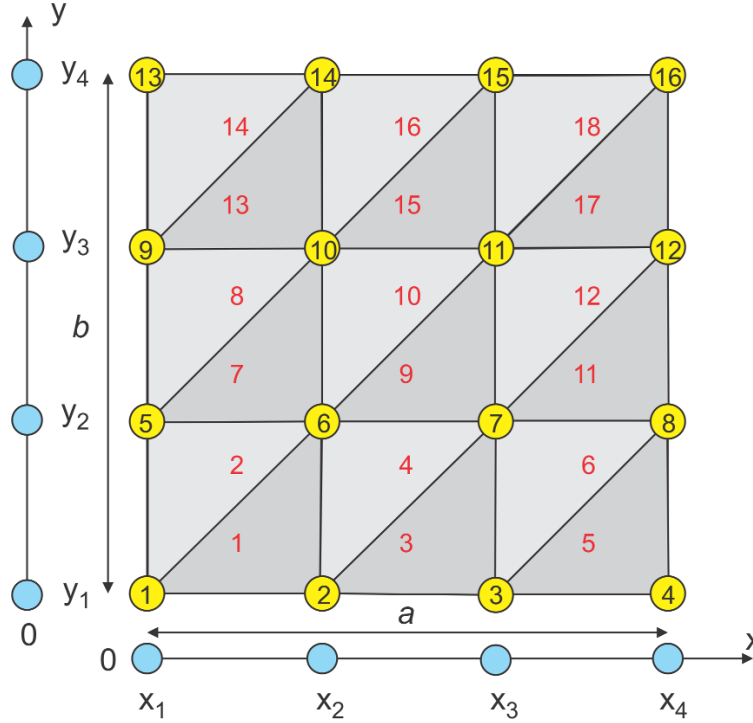


Fig. 2.1 Mesh generation for a planar rectangle.

We first define uniformly spaced  $x$ -nodes and uniformly spaced  $y$ -nodes. Assume that there are  $N_x + 1$  nodal points along the  $x$ -axis and  $N_y + 1$  nodal points along the  $y$ -axis. In Fig.2.1,  $N_x = 3$ ,  $N_y = 3$ . In a general case, one has

$$x_m = \left( \frac{m-1}{N_x} \right) a, \quad m = 1, \dots, N_x + 1$$

$$y_n = \left( \frac{n-1}{N_y} \right) b, \quad n = 1, \dots, N_y + 1$$
(2.1)

There is a common way of describing triangular meshes, which originates from old NASTRAN programs written in the 1970s and 1980s. In order to define a triangular mesh, we need the *array of vertices* (or nodes),  $P$ . This array consists of rows; every row includes three Cartesian

coordinates of the corresponding nodal point. The row number in array  $P$  is simply the vertex number. Further, we need an *array of faces* (or triangles),  $t$  also called *connectivity matrix*. This array also consists of rows; every row includes three integer numbers of triangle vertices; each such number is simultaneously the row number of the array  $P$ . The row number in the array  $t$  is the number of the triangular face. For the mesh shown in Fig. 2.1, there are 16 nodes and 18 triangles, giving:

$$P = \begin{bmatrix} x_1 & y_1 & 0 \\ x_2 & y_1 & 0 \\ x_3 & y_1 & 0 \\ x_4 & y_1 & 0 \\ x_1 & y_2 & 0 \\ x_2 & y_2 & 0 \\ x_3 & y_2 & 0 \\ x_4 & y_2 & 0 \\ x_1 & y_3 & 0 \\ x_2 & y_3 & 0 \\ x_3 & y_3 & 0 \\ x_4 & y_3 & 0 \\ x_1 & y_4 & 0 \\ x_2 & y_4 & 0 \\ x_3 & y_4 & 0 \\ x_4 & y_4 & 0 \end{bmatrix} \quad t = \begin{bmatrix} 1 & 2 & 6 \\ 1 & 5 & 6 \\ 2 & 3 & 7 \\ 2 & 6 & 7 \\ 3 & 4 & 8 \\ 3 & 7 & 8 \\ \dots & & \\ 11 & 15 & 16 \end{bmatrix} \Rightarrow t = \begin{cases} \text{odd row :} \\ [m, m+1, m+N_x+2] + (n-1)(N_x+1) \\ \text{even row :} \\ [m, m+N_x+1, m+N_x+2] + (n-1)(N_x+1) \\ m=1, \dots, N_x, \quad n=1, \dots, N_y \end{cases} \quad (2.2)$$

### ***Structured mesh***

The triangular mesh shown in Fig. 2.1 is called a *structured surface mesh*. In a structured mesh, the indices of the neighbor vertices for any particular vertex could in principle be calculated using a simple addition rule – see Fig. 2.1 and Eq. (2.2). As long as this rule is known, the array of triangular patches,  $t$ , is not really necessary. However, in *unstructured meshes*, studied in the next section, we must use a list of each node's neighbors – the connectivity array,  $t$ .

### ***Non-uniform mesh***

Often, it is desired to increase the triangle density close to the certain areas, for example, close to rectangle edges. In this case, Eqs. (2.1), which are the generating equations for nodal points, may be modified accordingly. For example, the generator

$$\begin{aligned}
x_m &= \left[ 1 - \cos\left(\frac{m-1}{N_x}\right) \right] \frac{a}{2}, \quad m = 1, \dots, N_x + 1 \\
y_n &= \left[ 1 - \cos\left(\frac{n-1}{N_y}\right) \right] \frac{b}{2}, \quad n = 1, \dots, N_y + 1
\end{aligned} \tag{2.3}$$

will create the triangular mesh shown in Fig. 2.2. Note that the array,  $t$ , remains the same for meshes in both Fig. 2.1 and Fig. 2.2.

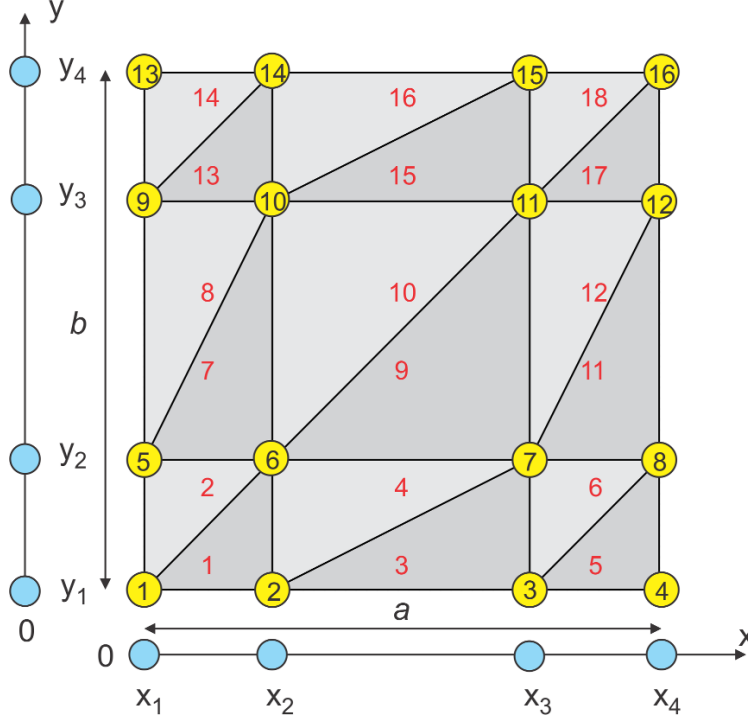


Fig. 2.2 Mesh generation for a planar rectangle with non-uniform nodes.

### ***Mesh storage formats***

Many modern mesh storage formats also include *edge information*. For example, the *winged edge format* used in computer graphics for each edge gives: two vertices of the edge, two faces attached to the edge, and the four edges attached to the edge of interest. Indeed, the edge information can be retrieved from the face information and vice versa. The above format is only valid for manifold meshes as explained in the following text.

#### ***2.1.2. A 3D triangular mesh. 2-Manifold meshes***

When a third spatial coordinate  $z$  is added to the array of nodes in Eq. (2.2), a 3D triangular mesh is obtained. Figure 2.3 shows a triangular mesh for a sphere. This mesh has also been generated “by hand”. The idea here is to use an initial octahedron mesh, then divide the each edge of the mesh, and push all the new vertices in the direction of their outer normal so that they all belong to the sphere surface. This process is repeated as long as necessary. A problem with the triangular



mesh shown in Fig. 2.3 is in slightly different triangle sizes on the sphere surface, which is a deficiency if a *uniform* mesh is needed with the approximately equal triangles.

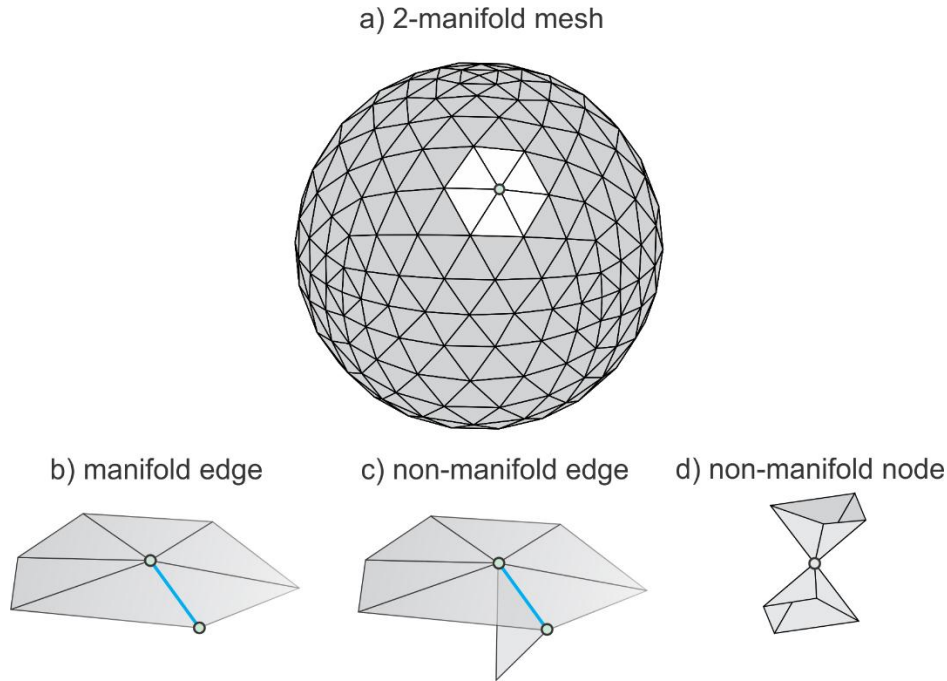


Fig. 2.3. a) – A 3D triangular mesh for a sphere with 512 triangles – a 2-manifold mesh; b) – manifold edge; c) – non-manifold edge; d) – non-manifold node.

The 3D triangular meshes are most important for the numerical analysis, computer graphics, and pattern recognition. The following two properties are of note:

1. A 3D triangular mesh usually represents a physical solid object. Therefore, it must be *watertight*, i.e. do not have missing triangles (surface holes).
2. The surface of a well-behaved triangular mesh in 3D must satisfy one critical condition, which is the so-called *manifold condition*. A mesh is *2-manifold* if every node of the mesh has a disk-shaped neighborhood of triangles – see Fig. 2.3a. This neighborhood can be continuously deformed to an open disk. Every edge of a 2-manifold mesh is a *manifold edge* – see Fig. 2.3b – with only two attached triangles.
3. All other meshes are *non-manifold meshes*. Fig. 2.3c gives an example of a non-manifold mesh with a *non-manifold edge*. A non-manifold mesh with a *non-manifold node* is shown in Fig. 2.3d.

The non-manifold meshes cannot be used for the numerical analysis, in most of the cases. Therefore, they must be *healed* prior to computations.

The definition of 2-manifold meshes is derived from the definition of 2-manifold surfaces. A surface is a *2-manifold* if and only if for each point  $r$  on the surface there exists an open ball with center  $r$  and sufficiently small radius so that the intersection of this ball and the surface can be continuously deformed to an open disk [1].

### 2.1.3. Triangle quality and mesh quality

The triangular mesh should be used to obtain a solution to differential or integral equations. The long narrow triangles seen in particular in Fig. 2.2 are generally not desirable since electric charge and current distributions may significantly vary along their lengths. Such a feature is in contradiction with the general idea of surface discretization, where we typically assume that the electric (or other) parameters are approximately constant for every small triangle.

The best triangle is an equilateral triangle, with all three triangle angles equal to 60 degrees, i.e.  $\alpha = \beta = \gamma = 60^\circ$ . In reality, the mesh cannot consist of only equilateral triangles. The *quality of the triangular element* is therefore introduced, which is essentially a measure of the deviation from an equilateral triangle. One common quality measure is the ratio between the radius of the inscribed circle (times two),  $r_{in}$ , and the radius of the circumscribed circle,  $r_{out}$ , – see Fig. 2.4.

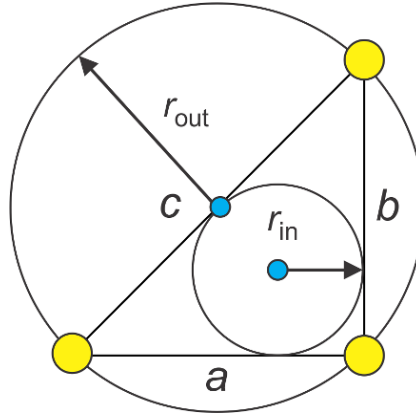


Fig. 2.4. Radii of the inscribed circle (largest circle contained in the triangle) and the circumscribed circle (smallest circle containing the triangle), respectively, for a right-angled isosceles triangle.  $r_{in}$  is called the inradius and  $r_{out}$  is the circumradius.

The quality factor  $q$  is expressed by [2]:

$$q \equiv \frac{2r_{in}}{r_{out}} = \frac{(b+c-a)(c+a-b)(a+b-c)}{abc} \quad (2.4)$$

where  $a, b, c$  are the triangle sides. Another useful expression is [2]:

$$q = \frac{2r_{in}}{r_{out}} = 2(\cos \alpha + \cos \beta + \cos \gamma - 1) \quad (2.5)$$

The overall quality factor of the entire triangular mesh may be the lowest  $q$ -factor of an individual triangle in the mesh. For example, the mesh shown in Fig. 2.3 has an overall mesh quality 0.83. Alternatively, a histogram may be used, which displays the number of triangles of a certain quality. The quality factor introduced above is not the only quality measure. Many other measures of element quality exist [3], [4], [5].

#### 2.1.4. Triangle size and mesh uniformity

A natural measure of triangle size is the radius of the circumscribed circle,  $r_{out}$  in Fig. 2.4 [6]. Such a radius is half of the longest edge for degenerate triangles. For equilateral triangles with side  $a$ ,

$$r_{out} = a / \sqrt{3} \quad (2.6)$$

### 2.2. Delaunay triangulation and three dimensional volume and surface meshes

#### 2.2.1. Structured vs. unstructured meshes

Triangular meshes can be categorized as *structured* or *unstructured*. Figs. 2.1 and 2.2 of the previous section illustrate examples of structured meshes. According to Ref.[7], “structured meshes exhibit a uniform topological structure that unstructured meshes lack. A functional definition is that in a structured mesh, the indices of the neighbors of any node can be calculated using simple addition, whereas an unstructured mesh necessitates the storage of a list of each node’s neighbors.” An example of the structured mesh is given by Eqs. (2.2) of section 2.1. There, all rows of the triangle array  $t$  are computed analytically.

The structured surface meshes might be used for simple geometries (a rectangle or a brick in 3D). Inclusion of non-trivial (polygonal or curved) boundaries usually results in the unstructured meshes. Furthermore, the unstructured meshes can provide finer resolution in certain (sometimes not a priori known) domains of interest. In what follows, we will study the unstructured meshes.

#### 2.2.2. Mesh generation and its properties

Surface mesh generation is a creation of an array of nodes,  $P$ , for a geometrical structure and subdivision of this structure into small planar triangles described by the array  $t$ . There are several desirable properties of mesh generation [7]:

1. The triangles should not intersect the boundaries (in other words, should “respect” the boundaries). Consecutive triangle edges should approximate actual curved boundaries by closest piecewise-linear boundaries.
2. The mesh generation should offer as much control as possible over the sizes of elements in the mesh. This control means the ability to grade from small to large triangles over a relatively short distance.
3. A third (most difficult) goal of mesh generation is that all the triangles should have a relatively high quality as described in section 2.1.

#### 2.2.3. Delaunay triangulation in two dimensions

According to Ref.[8], “despite an abundance of recent work on procedures of generating good triangulation, none of the modern approaches compare in elegance and generality to a procedure developed over fifty years ago by the Russian mathematician Delaunay. Delaunay [9] derived a simple procedure for triangulating an arbitrary set of points on a plane in such a way that *the sum of minimum angle(s) in each triangle would be maximized*. Since finite-element solutions are most accurate with nearly equilateral triangle grids, and since the Delaunay triangulation procedure

comes as close as possible to this, it is an excellent method to use with the finite-element method." More precisely, the Delaunay triangulation in two dimensions maximizes the minimum angle of all the angles of the triangles in the triangulation [7]. In other words, it maximizes minimum triangle quality of the mesh according to Eq. (2.5).

#### 2.2.4. Algorithm

Assume that we have the array of nodes,  $P$  shown by small circles in Fig. 2.5. We need an array of nonintersecting triangles,  $t$ . The following theorem applies: "Three points  $p_1, p_2, p_3$  are vertices of the same triangle of the Delaunay triangulation of  $P$  if and only if the circle through  $p_1, p_2, p_3$  (the circumcircle of triangle  $p_1, p_2, p_3$ ) contains no point,  $P$ , in its interior. Points on the circle boundary are permitted."

This theorem is illustrated in Fig. 2.5. Triangle  $p_1, p_2, p_3$  in Fig. 2.5a is Delaunay since its circumcircle is empty (does not contain any other nodes of  $P$ ). However, triangle  $p_1, p_2, p_3$  in Fig. 2.5b is not Delaunay since its circumcircle contains another node.

One popular algorithm for computing Delaunay triangulation is the *edge flip* demonstrated in Fig. 2.5. It begins with an arbitrary triangulation. Then, we use the following theorem: "An edge of the triangulation is Delaunay if and only if there exists an empty circle that passes through its vertices."

Thus, we check every edge in an arbitrarily-created mesh. If this edge is not Delaunay, such as the edge  $p_1, p_3$  in Fig. 2.5b, we simply flip it as shown in Fig. 2.5a. The flipped edge  $p_2, p_3$  is Delaunay. The algorithm requires  $O(n^2)$  edge flips for a set  $P$  of  $n$  points [7].

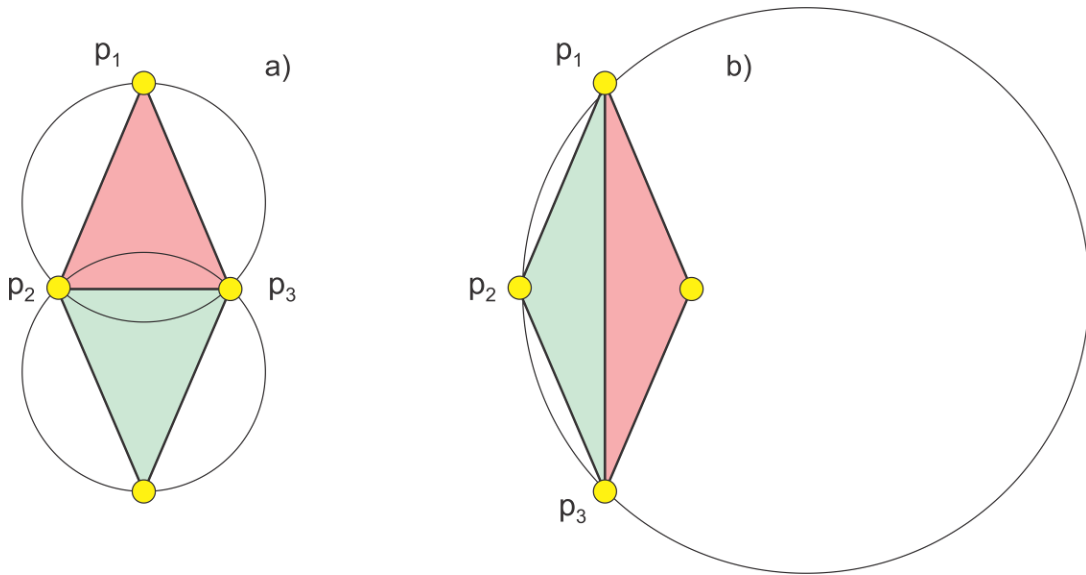


Fig. 2.5.a) – Delaunay triangulation of a set of four nodes; b) – non-Delaunay triangulation of the same node set.

The Delaunay triangulation of a given vertex set is *unique*. The triangle test or the edge test uniquely determines if the triangle or an edge is a part of the triangulation. The known exceptions are a line with more than two points on it, a circle with more than three points on it and no points inside, a sphere with more than four points on its surface and no points inside, and a few other similar cases [7].

Many algorithms compute the Delaunay triangulation by a fast check of whether there is a node inside a triangle in question or not. Today, the Delaunay triangulation of set  $P$  of  $n$  points in the plane can be computed in  $O(n \log(n))$  expected time, using  $O(n)$  expected storage – see, for example Ref. [10]. The online documentation, algorithms, and examples are given in Ref.[11].

### 2.2.5. Constrained Delaunay triangulation explained through an example

The Delaunay triangulation should respect the boundary of the object. Therefore, it may start with the explicit definition of the boundary nodes and the boundary edges. The explicit inclusion of boundary edges is not necessary. However, for non-convex boundaries and multiple boundaries the explicit inclusion of the boundary edges is a must. The Delaunay triangulation constructed in this manner is the *constrained Delaunay triangulation*. Figure 2.6 shows an example [12]. In Fig. 2.6a, we have a polygon with eight boundary nodes and no interior nodes. An application of Delaunay triangulation gives the mesh in Fig. 2.6b, which does not respect the boundaries. When, however, the boundary edges are forced to be a part of the Delaunay triangulation, the mesh of Fig. 2.6c is obtained. The boundary is respected, but there are extra triangles. They are excluded from the mesh by checking the in/out (Boolean) status with respect to a closed boundary of an object – see Fig. 2.6d. Hence, the mesh of a non-convex polygon has been created.

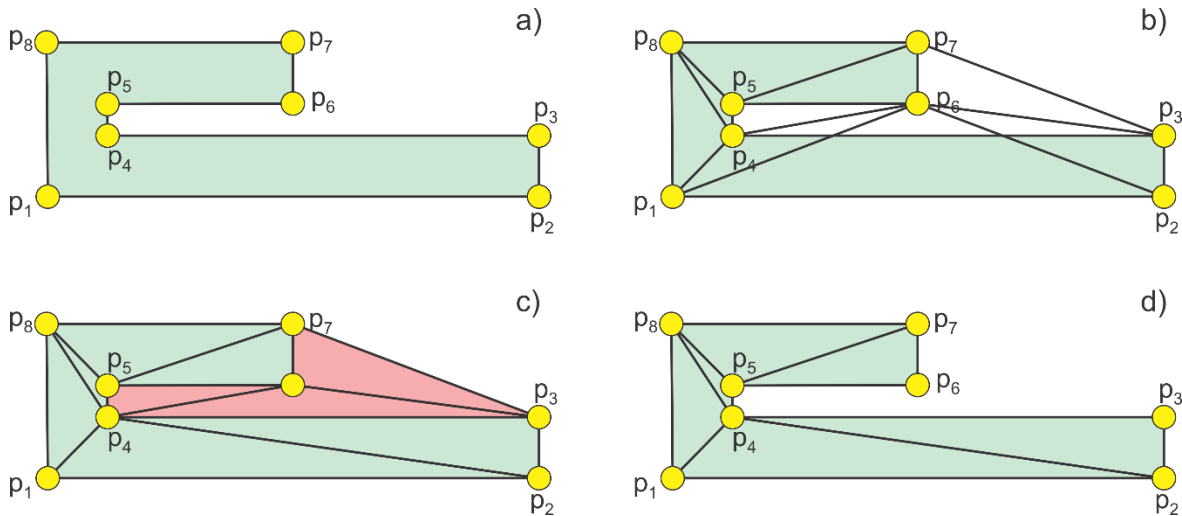


Fig. 2.6. Top – unconstrained Delaunay triangulation of a non-convex polygon; bottom - constrained Delaunay triangulation with boundary edges included into the mesh and removal of unnecessary triangles.

Note that reference [13] discusses edge-flip based algorithms for updating and constructing constrained Delaunay triangulations and constrained regular triangulations. A large collection of mesh generators can be found in online Ref. [14].

### 2.2.6. Delaunay triangulation in three dimensions (tessellation or tetrahedralization)

Given a set of points  $P$  in 3D one can build a tetrahedralization of the *convex hull* (or a convex envelope) that is, a partition of this convex volume into tetrahedra, in such a way that the circumscribing sphere of each tetrahedron does not contain any other point of  $P$  than the vertices of this tetrahedron. Such a tetrahedralization is called a *3D Delaunay triangulation* or *tessellation* or *tetrahedralization* [17]-[20]. Under non degeneracy assumptions (no three points on a line, etc.) it is unique. Many different techniques have been proposed for the computation of Delaunay triangulation in 3D [15]-[17]. One flipping-based algorithm is as follows [17], [18]. At the beginning the triangulation is initialized as a single tetrahedron, with vertices “at infinity”, that contains all points of  $P$ . At each step a new point from  $P$  is inserted and the corresponding tetrahedron, in which this point lies, is split. Then, the Delaunay property is re-established by “flipping” tetrahedra. This method is thus similar to the 2D triangulation method described above in Fig. 2.5.

### 2.2.7. Three-dimensional surface mesh generation

This problem is perhaps one of the most complicated task of mesh generation. An example is biomedical imaging, which is a very large area of research. A workflow for computational biomedical phantoms is a set of 3D mathematical surface meshing algorithms for anatomical structures, which are extracted from medical imaging data. This data includes Computed Tomography (CT), Magnetic Resonance Imaging (MRI), etc. A typical sequence for three-dimensional triangular surface mesh generation in particular includes:

1. Algorithm(s) for image registration and segmentation – creating a dense point cloud in the form of a shell corresponding to the boundary of a 3D shape from a stack of images [19]-[22] – see Fig. 2.7.
2. Algorithm(s) for surface reconstruction/extraction – creating a triangular surface mesh corresponding to this point cloud [20], [23]-[27] – see Figure 2.7b.
3. Algorithms for healing the resulting mesh [20], [23]-[27], mesh smoothing and coarsening [28], [35] – see Fig. 2.7b.

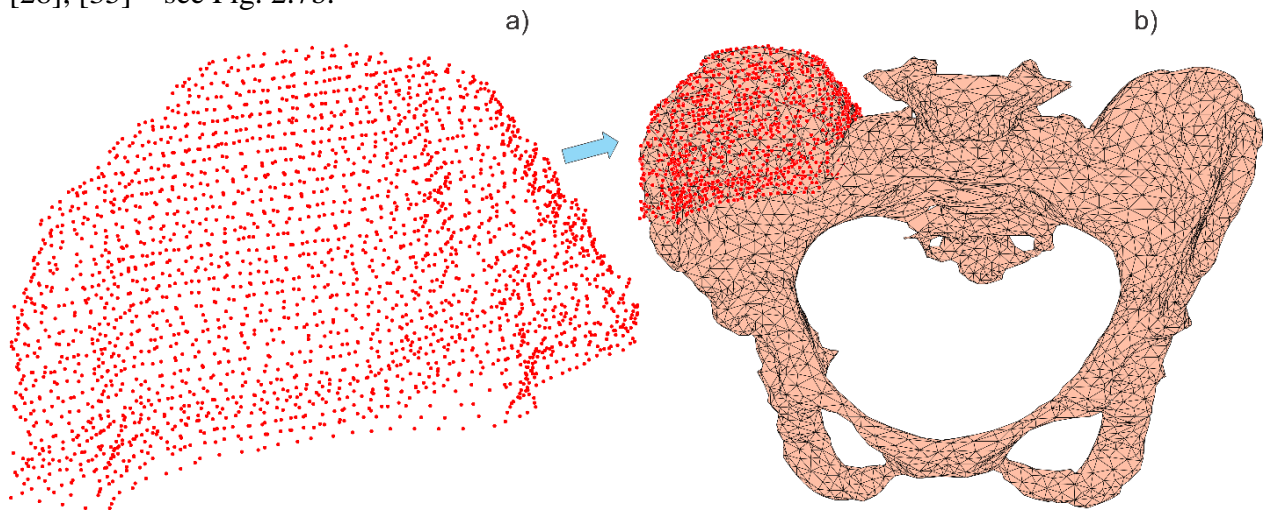


Fig. 2.7. Illustration of three-dimensional surface mesh generation for a pelvic bone from the stack of images for Visible Human (VHP) Project using MATLAB tools. Only a part of the original point cloud, which is the starting point of mesh generation, is shown in Fig. 2.7a.

### 2.2.8. Algorithms for three-dimensional surface mesh generation

A naïve but straightforward and simple way is to apply a 3D Delaunay triangulation to a point cloud, create a tetrahedral mesh, and extract the surface (boundary) faces. Unfortunately, most of the tessellation methods create a final convex tetrahedral mesh, which will mask all non-convex details in Fig. 2.7b. Therefore, this method works only for convex objects without holes. For arbitrary bodies, the problem greatly complicates. A very important concern is noise present in real scanned 3D data. Given that the entire problem is very complex, only brief outline of two methods are discussed: a sculpting-based volumetric method [17] and a region-growing surface method – *the ball-pivoting method* [25].

#### ***Volumetric method***

In sculpting-based methods, a volume tetrahedralization is computed from the data points, typically the 3D Delaunay triangulation. This may be done by surrounding the original dataset by a shield of extra points – see Fig. 2.8a where a projection of a 3D problem is shown. Tetrahedra are then removed from the convex hull to extract the original shape. It is easy to remove the tetrahedra, which contain boundary nodes. It is difficult to remove other tetrahedra under question. The concept is shown in Fig. 2.8a. A certain distance function from the domain surfaces [17] should be available and applicable.

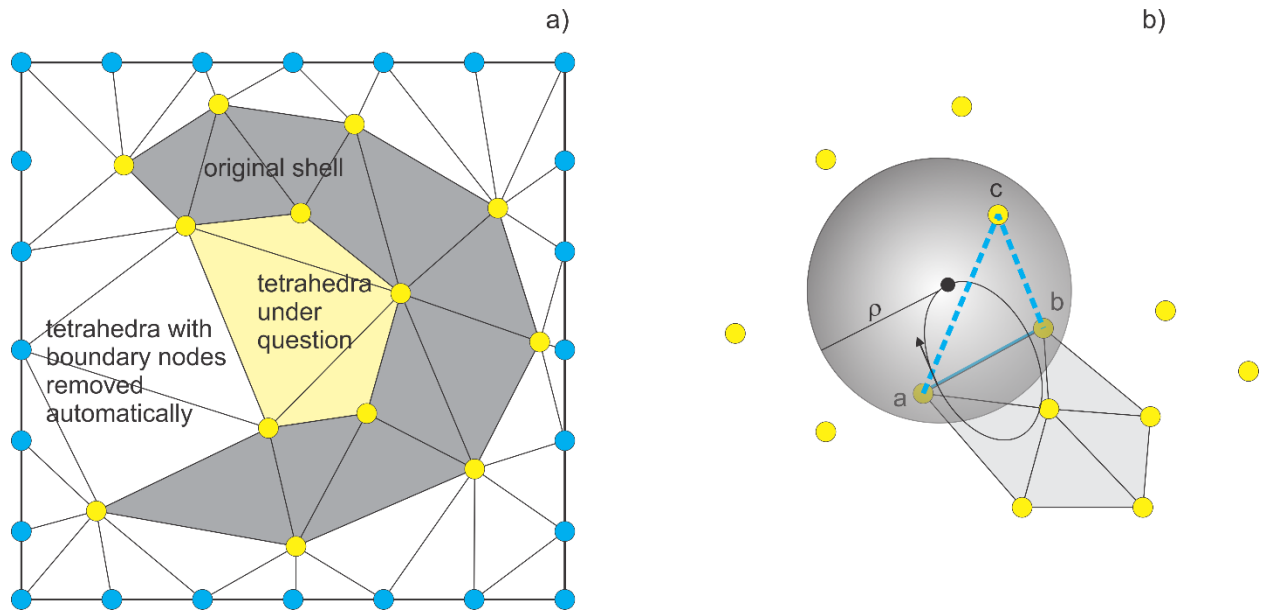


Fig. 2.8. Two methods of three-dimensional mesh generation. In Fig. 2.8a, only a projection of a tetrahedral mesh is shown.

#### ***Region-growing surface method (ball pivoting)***

The principle of the Ball-Pivoting Algorithm (BPA) is shown in Fig. 2.8b. We will essentially cite Ref.[25]. Three points form a triangle if a ball of a user-specified radius  $\rho$  touches them without



containing any other point. Starting with a seed triangle, the ball pivots around an edge  $ab$  (i.e. it revolves around the edge while keeping in contact with the edge's endpoints) until it touches another point  $c$ , forming another triangle. The rotation direction is shown in Fig. 2.8b. The process continues until all reachable edges have been tried, and then starts from another seed triangle, until all points have been considered. Parts of the surface mesh so created are then stitched together.

### ***Oversampling***

For both methods, oversampling (creation of a very large dense nodal set  $P$ ) may be a big plus. However, the oversampling is limited by the image resolution and other factors.

## ***2.3. Mesh operations and transformations***

### ***2.3.1. Topology-preserving mesh transformations***

Once created, a triangular mesh (more specifically, the array of vertices  $P$ ) as a whole could be subject to a shift, rotation, or other operations in 3D. A third coordinate may need to be added to a 2D surface mesh; the starting point is to use  $P(:, 3) = 0$ . Most common mesh operations include mesh translation, rotation, scaling, and deformation. Those operations correspond to the translation, rotation, or deformation of the original object. It is important to emphasize that the array of faces or triangles,  $t$ , *always* remains the same. *Mesh translation* (shift) is the movement as a whole, along some vector  $(x, y, z)$ . It is given by:

$$P(:, 1) \rightarrow P(:, 1) + x, \quad P(:, 2) \rightarrow P(:, 2) + y, \quad P(:, 3) \rightarrow P(:, 3) + z \quad (2.7)$$

Another simple operation is *mesh scaling*. Mesh scaling by the factor  $(S_x, S_y, S_z)$  in three dimensions is done according to:

$$P(:, 1) \rightarrow S_x P(:, 1), \quad P(:, 2) \rightarrow S_y P(:, 2), \quad P(:, 3) \rightarrow S_z P(:, 3) \quad (2.8)$$

*Mesh rotation* about the  $x$ -axis by angle  $\theta$  following the right-hand rule is given by:

$$\begin{aligned} P(:, 1) &\rightarrow P(:, 1) \\ P(:, 2) &\rightarrow +\cos \theta P(:, 2) + \sin \theta P(:, 3) \\ P(:, 3) &\rightarrow -\sin \theta P(:, 2) + \cos \theta P(:, 3) \end{aligned} \quad (2.9)$$

Mesh rotation about the  $z$ -axis by angle  $\varphi$  is given by a similar expression:

$$\begin{aligned} P(:, 3) &\rightarrow P(:, 3) \\ P(:, 1) &\rightarrow +\cos \theta P(:, 1) + \sin \theta P(:, 2) \\ P(:, 2) &\rightarrow -\sin \theta P(:, 1) + \cos \theta P(:, 2) \end{aligned} \quad (2.10)$$



A very efficient method for rotating an entire mesh in space, given an arbitrary axis with the unit vector  $\mathbf{k}$  and an angle of rotation  $\theta$  is the *Rodrigues' rotation formula*. It has the form (noting that rotation about the axis follows the right-hand rule):

$$P_{\text{new}} = P \cos \theta + (K \times P)_{\text{rowwise}} \sin \theta + K \circ K'(1 - \cos \theta) \quad (2.11)$$

Here,  $\times$  denotes the cross-product and array  $K$  has the same dimensions as  $P$ ; it consists of the required number of copies of the vector  $\mathbf{k}$ . Array  $K'$  also has the same dimensions as  $P$ ; it contains three identical columns of dot products  $(K \cdot P)_{\text{rowwise}}$ . The symbol  $\circ$  means *Hadamard product* (element by element multiplication).

### 2.3.2. Necessity of mesh smoothing

Often, the (constrained) 2D Delaunay triangulation algorithm *for planar meshes* is readily available, in particular using the basic MATLAB platform. Then, a mesh for a 2D convex or any non-convex *complicated shape* represented by multiple polygonal boundaries might be created as follows:

1. We select a *larger domain* of a simple shape that contains all boundaries (a rectangle, circle, etc.). We fill this domain with nodes distributed either randomly or, alternatively, as nodes of equilateral triangles of a certain size *excluding* the nodes outside the domain. The resulting node array is  $P$ .
2. We analytically specify the *required* boundary nodes,  $P_b$ , and the corresponding boundary edges,  $C$ . The boundary nodes are put *up front* in the resulting node array,  $P \rightarrow [P_b; P]$ , in order to keep the connectivity in  $C$ . This is a very critical step.
3. We apply the constrained Delaunay triangulation with constraints on  $C$  and select subdomains if necessary. Such subdomains may be, for example, electrodes attached to a conducting object.

### 2.3.3. Topology-preserving Laplacian smoothing

According to Ref.[32], “there are mainly three types of mesh improvement methods: (1) refinement or coarsening, (2) edge swapping, and (3) mesh smoothing. The refinement and the coarsening mainly try to optimize the mesh density, while edge swapping and mesh smoothing mainly aim to optimize the shape regularity. There are mainly two types of smoothing methods, namely Laplacian smoothing and optimization-based smoothing.”

In its basic form, Laplacian smoothing implies moving each vertex to the arithmetic average of the neighboring vertices while keeping the boundary nodes and boundary connectivity (boundary edges) *unchanged* as shown in Fig. 2.9. In other words, a free vertex of the mesh is simply relocated to the centroid of the vertices connected to that vertex. In Fig. 2.9, the node  $p_5$  is moved to the average of the neighboring points  $p_1, p_2, p_3, p_4$ . In this way, the local triangle quality greatly

improves. Indeed, in order to perform the smoothing we should know the neighboring nodes (neighboring triangles) for every mesh node.

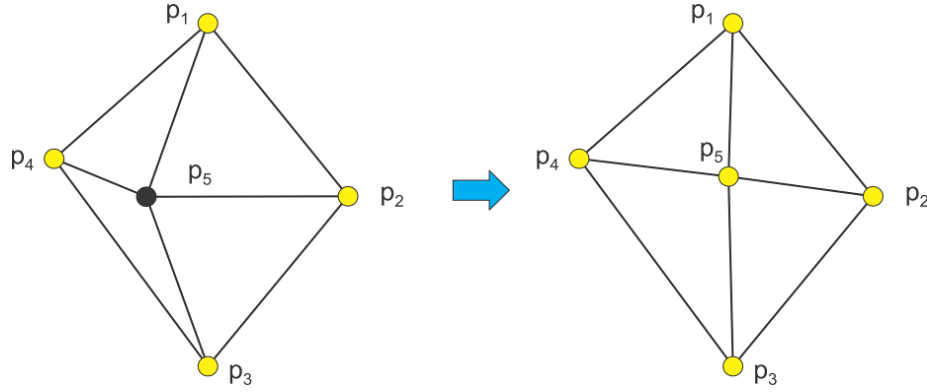


Fig. 2.9. Concept of Laplacian smoothing.

Reference [34] provides a comprehensive overview of different Laplacian smoothing methods. Some of them are briefly listed below.

**Standard Laplacian smoothing** shown in Fig. 2.9:

$$p^* = \frac{1}{k} \sum_{p_j \in \Omega_i, p_j \neq p_i} p_j \quad (2.12)$$

where  $\Omega_i$  is the “star” of the vertex  $p_i$  having  $k$  points and  $p^*$  is the new location of  $p_i$ .

**Lumped Laplacian smoothing**,

$$p^* = \frac{1}{3} p_i + \frac{2}{3} \frac{1}{k} \sum_{p_j \in \Omega_i, p_j \neq p_i} p_j \quad (2.13)$$

**Centroid Voronoi Tessellation (CVT) smoothing** utilizing attached triangle centers  $t_j$  and areas  $A_j$ ,

$$p^* = \sum t_j A_j / \sum A_j \quad (2.14)$$

**Weighted Centroid of Circumcenters (WCC) smoothing** utilizing attached triangle circumcenters  $c_j$  and areas  $A_j$ ,

$$p^* = \sum c_j A_j / \sum A_j \quad (2.15)$$

Equally-weighted versions of Eqs (2.14), (2.15) may be used.

#### **2.3.4. Laplacian smoothing with re-triangulation. Iterative algorithm**

After the creation of the initial mesh, the Laplacian smoothing of any type is applied to all free nodes except the boundary nodes. After that, the constrained Delaunay triangulation with the constraints is defined. Then, the Laplacian smoothing is applied again and the process repeats itself iteratively. One measure of convergence is the control of the resulting mesh quality. The process may be stopped when the triangle quality ceases to increase or it oscillates about a certain value. Note that the Laplacian smoothing does not necessarily converge except for the algorithm **Lumped Laplacian smoothing** [30].

There are two techniques to calculate new positions,  $p^*$ . The first method is to modify *all* positions by one step. This method is called the *simultaneous version*. The second variant is to update the new positions of  $p^*$  immediately. This variant is called the *sequential version*. In this latter case, a position  $p^*$  may not solely depend on the “set” of old positions but can also depend on previously calculated new positions. The Laplacian algorithm **Standard Laplacian smoothing** has the property that the limits of the two techniques are the same if they exist [30].

#### **2.3.5. Weaknesses of Laplacian smoothing**

The Laplacian smoothing algorithm described in previous subsections has the following weaknesses:

1. It is a *local* algorithm with fixed boundary nodes; therefore it is not able to provide high-quality uniform meshes from an arbitrary set of given nodes. If the nodes were initially concentrated in one local area, they will stay there forever.
2. For the same reason, it is not well suited for creating high-quality, non-uniform meshes with different triangle sizes from a given set of data points;
3. The proper handling of boundary nodes is an important subject. The method of fixed nodes used in this subsection is definitely not the best; it only works when the length of a boundary edge is approximately the best anticipated edge length for a given mesh. Also, intersecting boundaries require special care.

#### **Laplacian smoothing in three dimensions**

An undesirable effect is also the obvious “shrinkage” of 3D triangular surface meshes after Laplacian smoothing; the entire 3D mesh actually becomes smaller than it is in reality after several iterations [30]. A simple algorithm to avoid the shrinkage has been developed [30]. The idea is to push the modified points toward the previous points and the original points of the mesh.

### 2.3.6. Boolean operations with meshes

#### *Combining multiple meshes into one mesh*

Consider two *non-intersecting* meshes  $P_1, t_1$  and  $P_2, t_2$ . The meshes are combined into one mesh following the rule:

$$P = [P_1; P_2], \quad t = [t_1; t_2 + n_1] \quad (2.16)$$

This rule is easily extended to three and more meshes. Here,  $n_1$  is the number of nodes in the first mesh.

#### *Constructive solid geometry*

Boolean operations with simple shapes in 2D and 3D are a part of *Constructive Solid Geometry* (CSG) or *Constructive Volume Geometry* (CVG) algorithms [37]-[39], also implemented in MATLAB [38] for simple shapes. This very interesting subject is beyond the scope of the present section.

#### *Boolean operations with realistic 3D surface meshes*

While the CSG works quite well for simple shapes, union, subtraction, and intersection of two realistic 3D surface meshes is a very difficult task [40]-[44]. All intersecting triangles have to be identified, properly split, and re-triangulated in some way or other.

#### *Boolean operations with 2D surface meshes*

The problem simplifies in two dimensions where we only need to split intersecting edges. If a function that checks the in/out status of node in an arbitrary polygon is readily available, the Boolean operations may be implemented with the explicit boundary descriptions (through given boundary nodes and edges). This is the case with the basic MATLAB package where such a function is `inOutStatus` of the class `DelaunayTri`. An outer boundary (outer polygon enclosing all objects) must be given.

### 2.3.7 Collision algorithms for 3D surface meshes

Algorithms that find ray-triangle, segment-triangle, and triangle-triangle intersections [40]-[48] are in particular a basic component of all collision detection data in computer animation. As far computational purposes are concerned, these algorithms allow us:

1. Find outer surface normal vectors for a 3D shell;
2. Perform the inside/outside check for an arbitrary node;
3. Perform Boolean operations (union, subtraction, intersection) on realistic 3D surface meshes [40]-[44] including meshes of various tissues obtained from the medical image data.

#### *Ray-triangle intersection with Möller and Trumbore algorithm [47]*

This algorithm is perhaps most common. We define a ray,  $\mathbf{R}(t)$  as  $\mathbf{R}(t) = \mathbf{O} + t \cdot \mathbf{d}$  where  $\mathbf{O}$  is the origin of the ray and  $\mathbf{d}$  is the normalized direction vector. We define a triangle by three vertices:  $\mathbf{p}_1$ ,  $\mathbf{p}_2$  and  $\mathbf{p}_3$ . We define the point,  $\mathbf{T}(u, v)$  on the triangle as:

$$\mathbf{T}(u, v) = (1 - u - v)\mathbf{p}_1 + u\mathbf{p}_2 + v\mathbf{p}_3 \quad (2.17)$$

where  $(u, v)$  are *barycentric coordinates*, which, by definition, meet the following conditions:

$$u \geq 0, v \geq 0, u + v \leq 1. \quad (2.18)$$

To find the intersection point between the ray and the triangle, Eqs. (2.17), (2.18) are to be solved simultaneously, which yields

$$\mathbf{O} + t \cdot \mathbf{d} = (1 - u - v)\mathbf{p}_1 + u\mathbf{p}_2 + v\mathbf{p}_3 \quad (2.19)$$

Rearranging the terms leads to the matrix equation,

$$\begin{bmatrix} -\mathbf{d} & \mathbf{e}_1 & \mathbf{e}_2 \end{bmatrix} \cdot \begin{bmatrix} t \\ u \\ v \end{bmatrix} = \mathbf{O} - \mathbf{p}_1 \quad (2.20)$$

where  $\mathbf{e}_1 = \mathbf{p}_2 - \mathbf{p}_1$  and  $\mathbf{e}_2 = \mathbf{p}_3 - \mathbf{p}_1$ . By solving Eq. (2.20), we can find the barycentric coordinates  $(u, v)$  and the distance,  $t$ , from the ray origin to the intersection point. The solution to Eqs. (2.20) is obtained using the Cramer's rule:

$$\begin{bmatrix} t \\ u \\ v \end{bmatrix} = \frac{1}{(\mathbf{d} \times \mathbf{e}_2) \cdot \mathbf{e}_1} \begin{bmatrix} (\mathbf{tvec} \times \mathbf{e}_1) \cdot \mathbf{e}_2 \\ (\mathbf{d} \times \mathbf{e}_2) \cdot \mathbf{tvec} \\ (\mathbf{tvec} \times \mathbf{e}_2) \cdot \mathbf{d} \end{bmatrix} = \frac{1}{\det} \begin{bmatrix} \mathbf{qvec} \cdot \mathbf{e}_2 \\ \mathbf{pvec} \cdot \mathbf{tvec} \\ \mathbf{qvec} \cdot \mathbf{d} \end{bmatrix} \quad (2.21)$$

where  $\mathbf{tvec} = \mathbf{O} - \mathbf{p}_1$ ,  $\mathbf{pvec} = (\mathbf{d} \times \mathbf{e}_2)$ ,  $\mathbf{qvec} = (\mathbf{tvec} \times \mathbf{e}_1)$  and  $\det = \mathbf{pvec} \cdot \mathbf{e}_1$ . Fig. 2.10a illustrates the implementation of this algorithm in MATLAB (MATLAB function `RayTriangleIntersection.m` to this section) for a ray passing through a human eye surface mesh. The intersection points are marked.

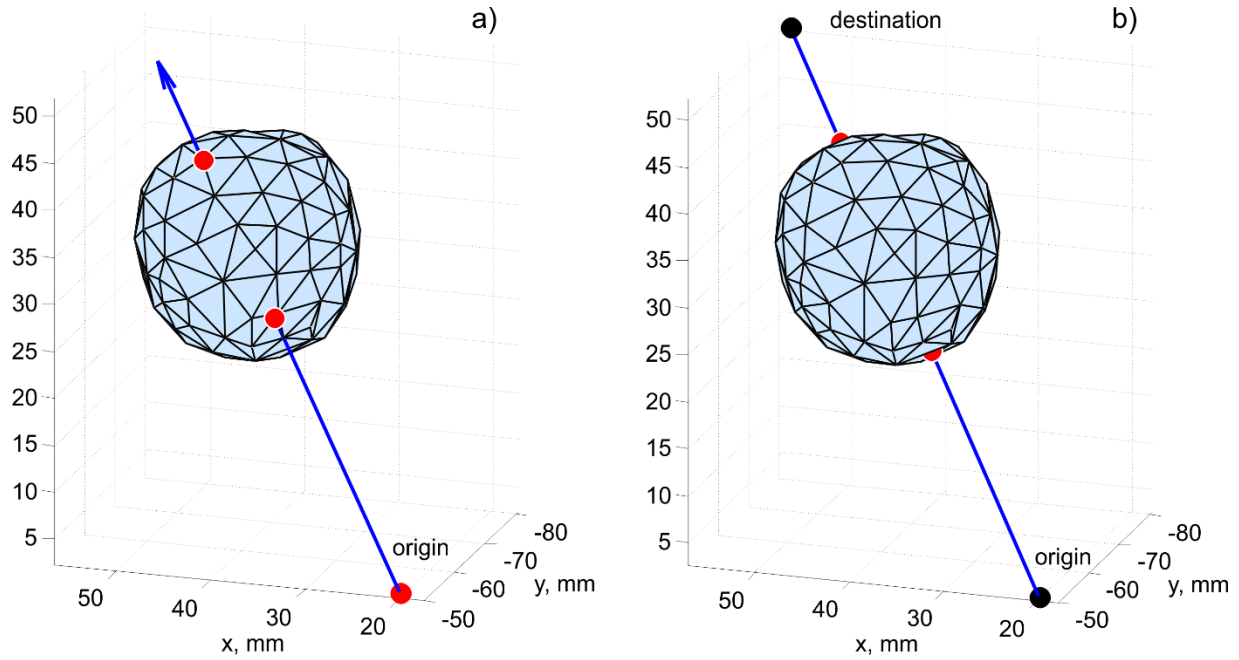


Fig. 2.10. a) – Ray-triangle intersection for a human eye; b) – segment-triangle intersection.

### ***Segment – triangle intersection***

The same algorithm applies (an alternative is algorithm of Ref. [46], which projects the point and triangle onto a 2D coordinate plane where inclusion is tested.). Similar to the ray-triangle intersection, we find the point(s) of intersection but the distance of this point from the origin should be less than or equal to the length of the segment. Fig. 2.24b illustrates the implementation of this algorithm in MATLAB (MATLAB function `SegmentTriangleIntersection.m` to this section) for a ray passing through a human eye surface mesh. The intersection points are marked.

### ***Triangle – triangle intersection and mesh – mesh intersection***

A triangle is a set of three segments. Therefore, a triangle-triangle intersection problem can be reduced to the segment-triangle intersection problem considered previously. However, separate fast algorithms may be developed too [44], [47]. Next, the mesh-mesh intersection problem can be reduced to the triangle-triangle intersection problem since every mesh is a combination of triangles. Consider a master mesh X and a slave mesh Y. Both meshes are 2-manifold. For any triangle from the master mesh there exist three different intersection cases as shown in Fig. 2.11. Cases #1 and #3 in Fig. 2.11 would become equivalent if we could treat the master and slave meshes as one set of triangles.

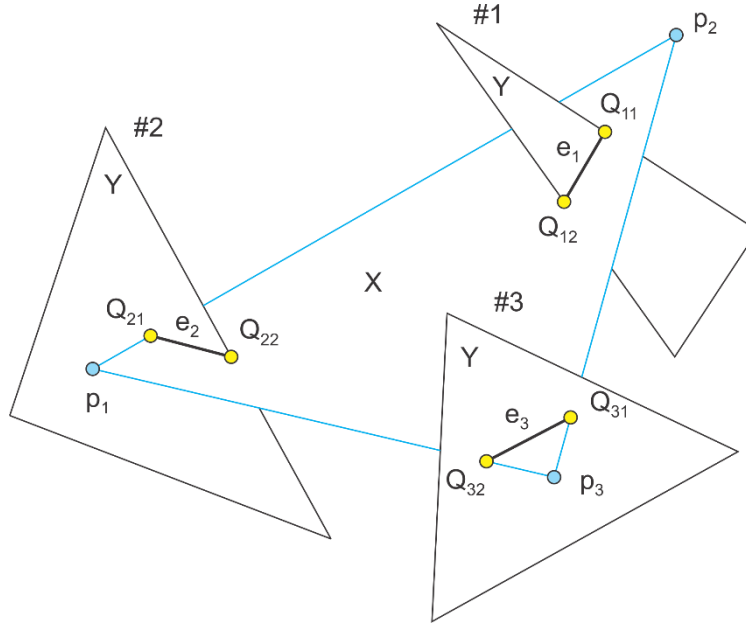


Fig. 2.11. Three types of intersection of a triangle from a master mesh X with various triangles of a slave mesh Y. Cases #1 and #3 are equivalent if we treat the master and slave meshes as one set of triangles.

With reference to Fig. 2.11 we could formulate one possible mesh-mesh intersection algorithm as follows:

1. For each triangle of the master mesh under question, we find intersecting edges  $e_i, i = 1, 2, 3, \dots$  in Fig. 2.25.
2. Next, we apply a constrained 2D Delaunay triangulation to triangle's plane and subdivide the master triangle into sub-triangles, which respect intersections.
3. The same procedure is applied to each triangle under question of the slave mesh.
4. We construct refined master and slave meshes, which respect all intersections.
5. Boolean operations on meshes are performed by checking in/out status of separate triangles.

Apparently, the above algorithm is quite slow. However it is simple and makes use of the existing constrained 2D Delaunay triangulation in MATLAB.

#### ***Other algorithms implemented in MATLAB***

MATLAB central provides a number of related vectorized scripts – see [48], [49]– for ray-triangle and segment-triangle intersection.

### ***2.3.8. Checking in/out status and finding outer normal vectors for 2-manifold 3D surface meshes***

#### ***In/out status***

Assume that an observation point in Fig. 2.12a lies outside a 2-manifold shell in three dimensions. A ray emanating from this point may or may not intersect this mesh. However, the number of intersections will always be even: 0, 2, 4, etc. Similarly, if the observation point lies inside the shell, the number of intersections will always be odd: 1, 2, 3, etc.

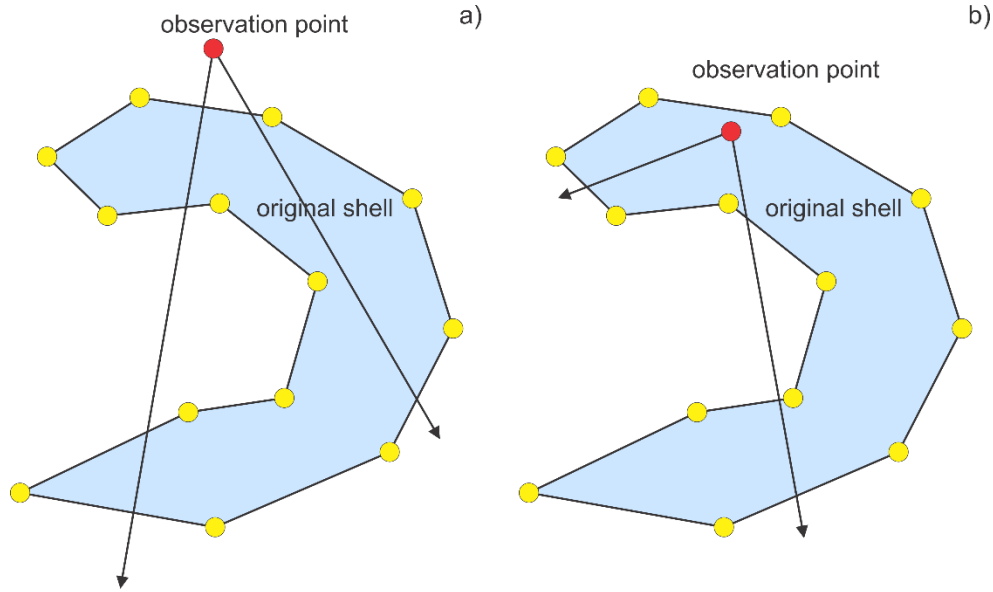


Fig. 2.12. Checking in/out status for a 2-manifold mesh. Only mesh cross-section is shown.

The critical point is that we do not have to check all rays; this can be done only once (excluding some degenerate cases). Therefore, a single ray can be constructed that points toward the center of a selected triangle in the mesh. Then, the ray-triangle intersection algorithm shown in Fig. 2.12 is applied and the number of intersections is counted.

#### ***Finding outer normal vectors***

The normal vector is defined as the normalized cross-product of two triangle edges; its sign is important. To select only the outer normal vector, we may set an observation point slightly above each triangle center, in the direction of the normal vector. If this point is outside the mesh, the normal direction is correct. If not, the direction is reversed. This algorithm is implemented in the MATLAB function `MeshNormals.m` to this section.

### ***2.4. Adaptive mesh refinement and mesh decimation***

Theory of adaptive mesh refinement in applications to the Boundary Element Method (BEM) or the Method of Moments (MoM) is developed in many references – see, for example, [50]-[58]. Its detailed analysis is not the subject of this section. This theory depends on the particular method used for computations. Here, we present one simple concept. This concept implies the MoM/BEM Galerkin method with the accurate calculation of potential integrals, makes it possible to evaluate the electric potential and the field at any point of the conducting (metal) boundary or dielectric/magnetic boundary. This also utilizes the simple mesh generation methods described in this Chapter.

#### ***2.4.1. Concept of adaptive mesh refinement***

As an example, we consider a surface of a metal object in the electrostatic case. Such a surface always possesses a given potential/voltage value. However, the charge distribution is to be evaluated numerically, for every surface triangle. After the numerical solution for the charge



distribution is complete, the electric potential may be computed back. Some possible steps for adaptive mesh refinement are then as follows:

(1a) ***Finding local solution error – collocation method.*** First, an error of the numerical solution must be found for every triangle in the mesh. In the *collocation method* [50], [52], [53] the electric potential on the object surface is matched to a given potential value, e.g. 1 V only for the collocation nodes (positions) – typically triangle centers or vertices. A relative potential (or charge/electric field) mismatch for *other positions* could be used as a *local error indicator* [50], [52], [53]. An excellent early paper on the local error behavior is Ref.[50].

(1b) ***Finding local solution error – Galerkin method.*** In the Galerkin method, there are no collocation nodes. However, once the numerical solution is available, the potential and the field may still be recalculated at any point of the boundary. Consider the boundary of a metal object with the constant impressed potential of 1 V. Using the existing BEM solution, the electric potential values are recalculated at every triangle center separately. Those values are never 1 V but rather slightly vary about this value. The corresponding absolute difference is an error.

(2) ***Using tangential electric field***

A similar treatment applies to the tangential electric field, which must be zero at the metal surfaces (for example, at triangle centers), but is never really zero. The corresponding absolute deviation is again an error. For dielectric-dielectric interfaces, the error in the boundary condition for the normal *E*-field component may be computed; for magnetic boundaries – the error in the normal *H*-field. A specific error measure may be more complicated and physically justified; this is the subject of a separate discussion.

(3) ***Triangle refinement.*** Triangles with the largest error (say for example the worst 15% of the total number of triangles) are refined by introducing new mesh nodes exactly at the centers of their edges as shown in Fig. 2.13. Two scenarios are possible: a) three new nodes at three edges of any triangle in question and b) new nodes only on the boundary edges and on edges adjacent to the two triangles in question. All boundary nodes including the old and new ones may be put up front in the new node array *P*.

(4) ***Mesh refinement.*** Constrained Laplacian smoothing described in the previous section may be applied to the new node array *P*. The Laplacian smoothing may involve Delaunay triangulation(s). The boundary nodes are not the subject to movement. If an inner node crosses the boundary, it is deleted. In the present section, this method will be developed only for a circle and rectangle, but it is applicable to any polygonal domain.

(5) ***Iterative adaptive mesh refinement.*** The numerical solution is calculated again and the process repeats itself until a stop criteria defined by the algorithm designer is met.

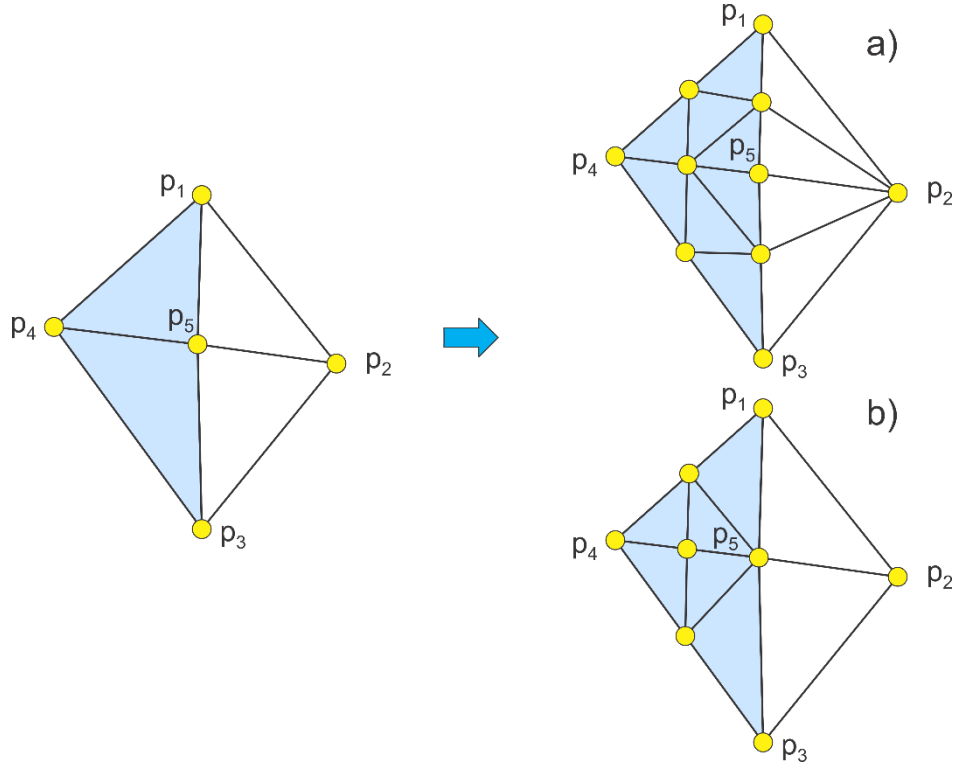


Fig. 2.13. Two scenarios of edge subdivisions for triangles with the largest error.

Note that the adaptive mesh refinement implies final meshes with very different triangle sizes; the max/min triangle size ratio is at least 10:1 and routinely reaches 100:2. Another feature of the iterative procedure is reusing the previous meshes.

#### 2.4.2. Example of adaptive mesh refinement with a given error function

Simple geometry shapes (also called *primitives*) are described *implicitly*, using the *distance function*. For example, a circle of radius  $R$  is described by distance function

$$d = \sqrt{P^2(:, 1) + P^2(:, 2)} - R \quad (2.22)$$

The local error indicator (or the local error function,  $e_n$ ) calculated at the center of triangle  $n$  will be modeled here by:

$$e_n = \frac{1}{\sqrt{|d|}} A_n^\alpha, \quad 0 \leq \alpha \leq 1 \quad (2.23)$$

where  $d$  is a distance function for an object and  $A_n$  is the triangle area. Note that the error function so selected increases toward the boundary and that the error function becomes singular at the boundary. One motivation for this choice is the well-known expression for the surface charge density,  $\sigma$ , in C/m<sup>2</sup> of a circle in vacuum with radius  $R$  and with the total charge  $Q$ , which is given by [60]-[61].

$$\sigma = \frac{Q}{2\pi R} \frac{1}{\sqrt{R^2 - r^2}}, \quad 0 \leq r \leq R \quad (2.24)$$

and tends to infinity at the edge of the disk.

Figure 2.14 demonstrates the mesh refinement process with 15% triangles to be refined at every step, with method a) in Fig.2.13 (all edges are subdivided), and with Laplacian smoothing of type **WCC** - see Eq. (2.15) of the previous section. Furthermore,  $\alpha = 1/4$  in Eq. (2.23). The mesh size increases by approximately 70% at every iteration step. Laplacian smoothing is performed iteratively, until the mesh quality increases.

It is seen in Fig. 2.14 that the adaptive mesh refinement reduces triangle quality, but usually not very significantly. The final mesh becomes highly-non-uniform. The max/min triangle size ratio for the last mesh in Fig. 2.14 is approximately 30:1.

#### ***2.4.3. Dependence on the error function and the refinement rate***

The mesh refinement procedure strongly depends on the error function given by Eq. (2.23) as well as on the mesh refinement rate. In the previous example, the mesh size increased by about 70% at every step. Note that the mesh size increase is not equal to the number of refined triangles. Usually, smaller rates of 20-30% are employed such as those in the finite-element solver ANSYS Maxwell3D or HFSS. The effect of the parameter  $\alpha$  in Eq. (2.23) may be critical.

Figure 2.15 shows a similar numerical experiment, but for the square plate. Five percent of all triangles are to be refined at every step, with option a) in Fig. 2.13, and with Laplacian smoothing of type **WCC** - see Eq. (2.15). The mesh size increases by approximately 20% at every step. Furthermore,  $\alpha = 1/2$  in Eq. (2.23). The Laplacian smoothing is performed iteratively, until the mesh quality increases. One can see that the mesh is finally refined not only at the edges, but also in the main area of the plate. The error plot at 11<sup>th</sup> iteration is shown on bottom left of Fig. 2.15; the corresponding refined mesh is shown on bottom right.

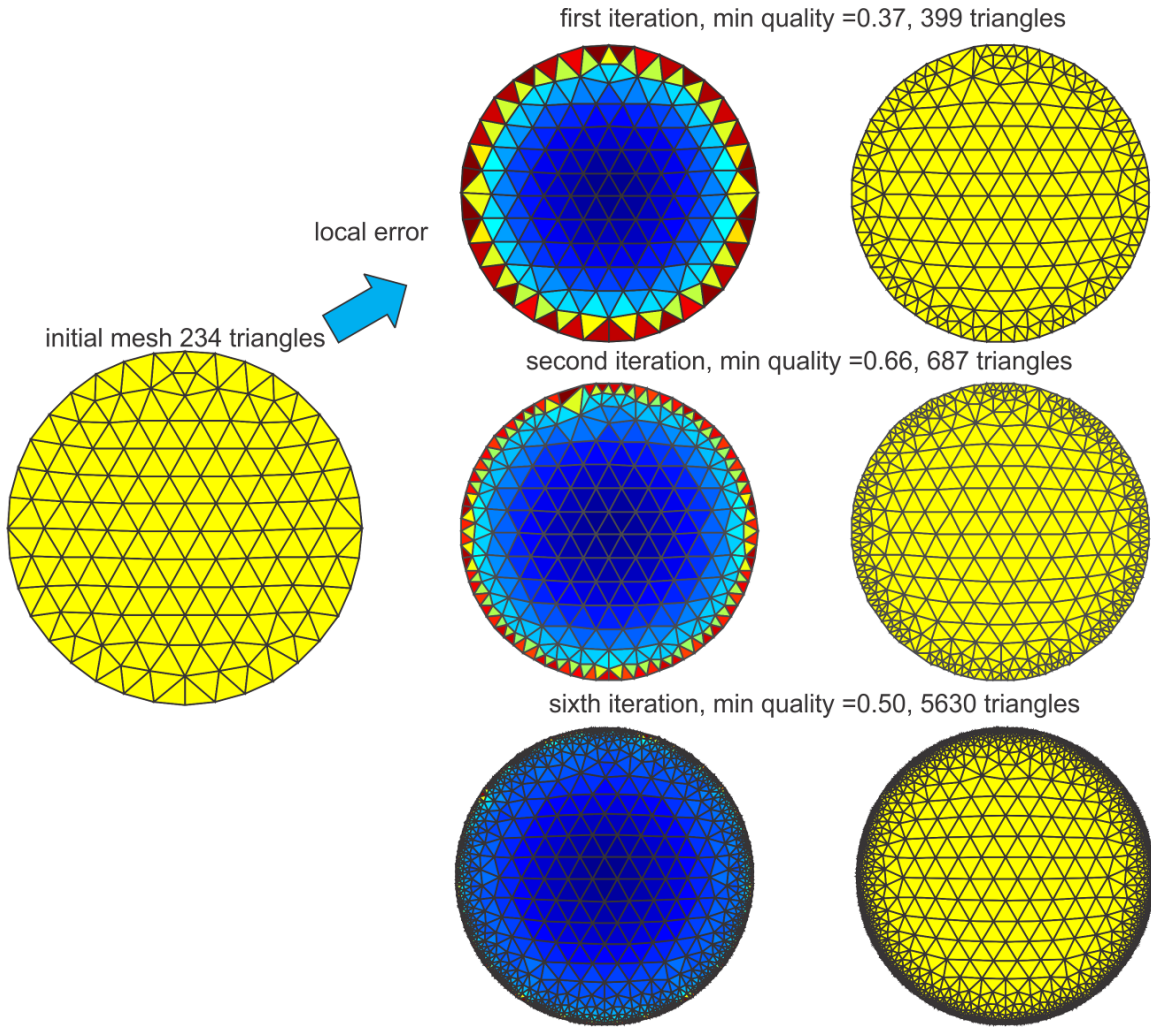


Fig. 2.14. Iterative meshes in the adaptive mesh refinement process. Left column shows the error plot at the previous iteration step; right column – the mesh refined according to this error.

#### 2.4.4. Mesh decimation

Quite often, a dense mesh in certain areas is not required. Depending on factors including the problem geometry, field gradient, and value of the error function, large triangles may provide an adequate solution, enabling reduction of the problem size and an increase in the speed of the calculation. The process of reducing mesh density in certain areas is known as *mesh decimation*. One popular algorithm for mesh decimation is the (incremental) *edge collapse* schematically shown in Fig. 2.16a (see, for example, Ref. [7]). Two nodes  $p_1, p_2$  of an edge (usually the shortest edge in the area of interest) are replaced by one node  $p_{12}$  at the edge center and the mesh topology is updated. Yet another algorithm is the *vertex removal* schematically shown in Fig. 2.16b. Node  $p_1$  and all triangles attached to this node is removed and the resulting hole is re-triangulated.

#### MATLAB implementation

One mesh decimation algorithm is implemented in MATLAB function `reducepatch.m`.

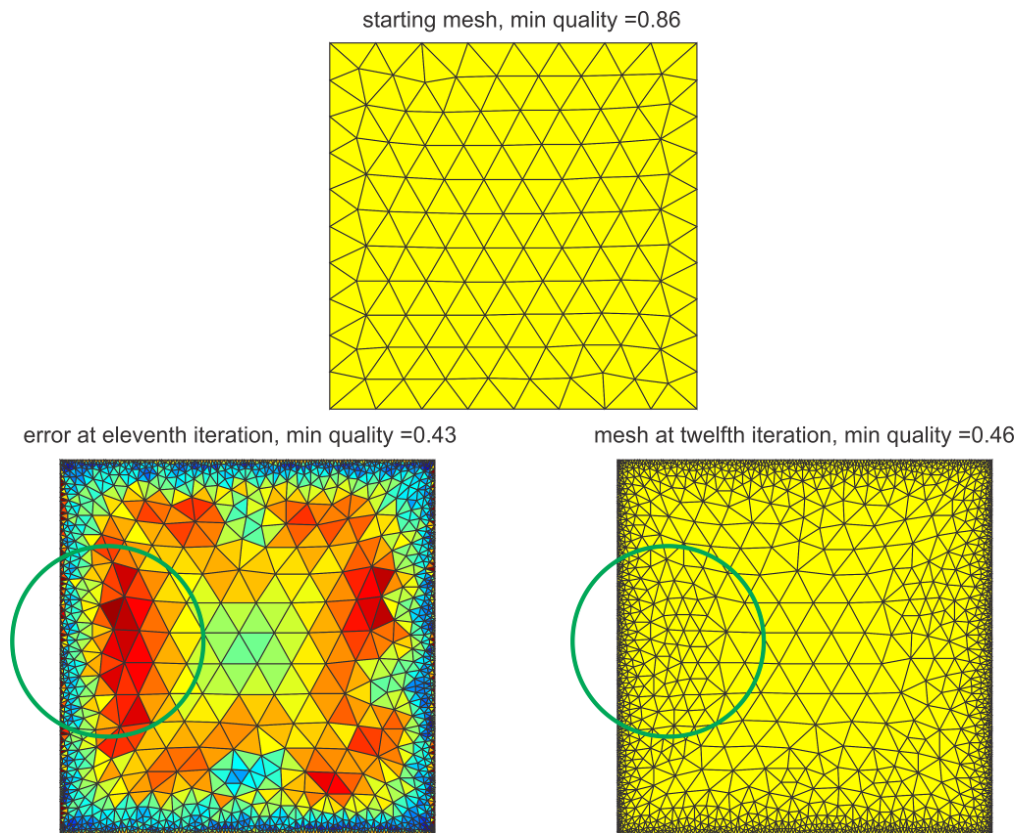


Fig. 2.15. Iterative meshes in the adaptive mesh refinement process for the square plate.

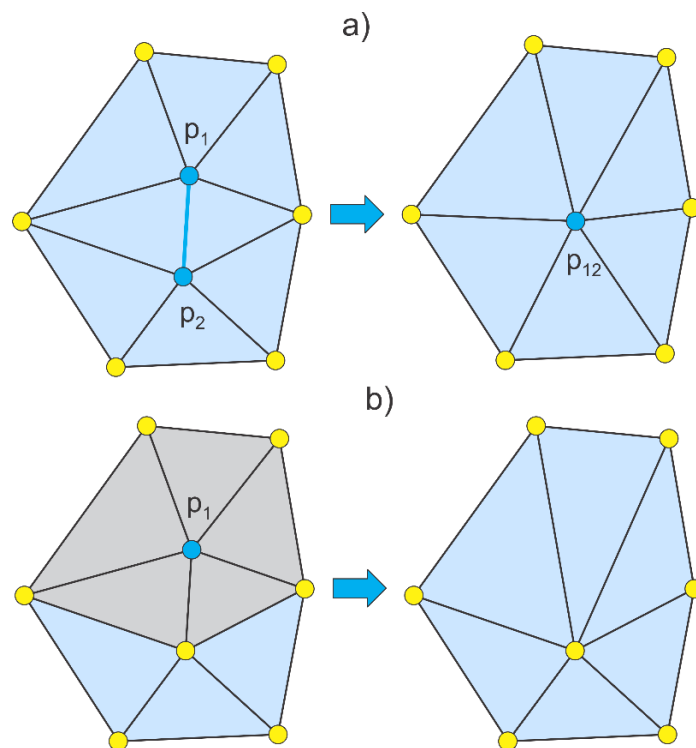


Fig. 2.16. a) - Edge collapse method; b) - vertex removal.

## References

- [1] Manifolds online: Dr. Ching-Kuang Shene, <http://www.cs.mtu.edu/~shene/COURSES/cs3621/NOTES/model/manifold.html>
- [2] R. A. Johnson, *Modern Geometry: An Elementary Treatise on the Geometry of the Triangle and the Circle*, Boston, MA, Houghton Mifflin, 1929, p. 189-192. Online: <http://mathworld.wolfram.com/Inradius.html>
- [3] D. A. Field, "Qualitative measures for initial meshes," *Intern. J. Numer. Methods Engineering*, vol. 47, pp. 887–906, 2000.
- [4] P. M. Knupp, "Remarks on Mesh Quality," 45th AIAA Aerospace Sciences Meeting and Exhibit, 7-10 January, 2007, Reno, NV, 10 p.
- [5] Online: [http://cubit.sandia.gov/help-version8.1/Chapter\\_5/Mesh\\_Quality\\_Assessment/Metrics\\_for\\_Triangular\\_Elements.html](http://cubit.sandia.gov/help-version8.1/Chapter_5/Mesh_Quality_Assessment/Metrics_for_Triangular_Elements.html)
- [6] P.-O. Persson, Mesh Generation for Implicit Geometries, PhD Thesis, MIT, Feb. 2005, 126 p. Online: <http://persson.berkeley.edu/thesis/persson-thesis-color.pdf>
- [7] J. R. Shewchuk, *Delaunay Refinement Mesh Generation*, PhD thesis, Computer Science Department, Carnegie Mellon University, May 18, 1997, Pittsburgh, PA.
- [8] Z. Cendes and D. Shenton, "Adaptive mesh refinement in the finite element computation of magnetic fields," *IEEE Trans. on Magnetics*, vol. 21, no. 5, Sep. 1985, pp. 1812-1816.
- [9] B. Delaunay, "Sur La Sphe're Vide," *Bull. Acad. Science USSR VII: Serie Sci. Math. Nat.*, 1934, pp. 783-800.
- [10] R. A. Dwyer, "A faster divide-and-conquer algorithm for constructing Delaunay triangulations," *Algorithmica*, vol. 2, no.2.4, 1987, pp. 137-152.
- [11] The Geometry Center Home Page: <http://www.qhull.org/>
- [12] MATLAB Online Help: *Computational geometry/Delaunay triangulation*.
- [13] J. R. Shewchuk, "Updating and constructing constrained Delaunay and constrained regular triangulations by flips," *Proc. of the 19<sup>th</sup> Annual Symposium on Computational Geometry (San Diego, California)*, pp. 182-190, Association for Computing Machinery, June 2003. Online: <http://www.cs.cmu.edu/~jrs/jrspapers.html>
- [14] R. Schneiders: <http://www-users.informatik.rwth-aachen.de/~roberts/software.html>
- [15] F. P. Preparata and M. I. Shamos, *Computational Geometry: an Introduction*, Springer-Verlag, New York, NY, 1985.
- [16] H. Edelsbrunner, "Algorithms in Combinatorial Geometry," vol. 10: EATCS Monographs on Theoretical Computer Science. Springer-Verlag, Heidelberg, Germany, 1987.
- [17] C. Bajaj, F. Bernardini, and G. Xu, "Automatic reconstruction of surfaces and scalar fields from 3D scans," in *Computer Graphics Proceedings*, 1995, Annual Conference Series. Proceedings of SIGGRAPH 95, pp. 109–118.
- [18] H. Edelsbrunner and N. R. Shah, Incremental topological flipping works for regular triangulations. In *Proc. 8th Annual ACM Sympos. Comput. Geom.* (1992), pp. 43–52.
- [19] P.A. Yushkevich, P. Joseph, C. Heather, et. al., "User-guided 3D active contour segmentation of anatomical structures: Significantly improved efficiency and reliability," *Neuroimage*, vol. 31(3), pp.1116-28, 2006.



- [20] P.G. Young, T.B.H. Beresford-West, S.R.L. Coward, et. al., "An efficient approach to converting 3D image data into highly accurate computational models," *Philos Trans A Math Phys Eng Sci.* A-13; vol. **366** (1878):pp. 3155-73, 2008.
- [21] M. Sezgin and B. Sankur, "Survey over image thresholding techniques and quantitative performance evaluation," *Journal of Electronic Imaging*, vol. **13**(1), pp. 46–165, Jan. 2004.
- [22] Q. Fang and D. Boas, "Tetrahedral mesh generation from volumetric binary and gray-scale images," *IEEE International Symposium on Biomedical Imaging* 2009, pp. 1142-1145, <http://iso2mesh.sourceforge.net/cgi-bin/index.cgi>
- [23] Lorensen, W.E. and Cline, H.E. "Marching cubes: A high resolution 3D surface construction algorithm," *Computer Graphics*, vol. **21**(4): 163-169, 1987.
- [24] Hilton, A., Stoddart, A.J., Illingworth, J., and Windeatt, T., "Marching Triangles: Range Image Fusion for Complex Object Modeling," *Image Processing*, vol. **1**, pp. 381–384. Sep 1996.
- [25] Bernardini, F., Mittleman, J., Rushmeier, H., Silva, C., and Taubin, G., "The ball pivoting algorithm for surface reconstruction," *IEEE Trans. Visualization and Computer Graphics*, vol. **5**, no 4, Oct-Dec. 1999.
- [26] Kazhdan, M., Bolitho, M., and Hoppe, H., "Poisson Surface Reconstruction," *Eurographics Symposium on Geometry Processing*, 2006.
- [27] Wang, M. and Feng, J.Q., "2D-manifold boundary surfaces extraction from heterogeneous object on GPU," *J. of Computer Science and Technology*, vol. **27**(4): 862–871, 2012.
- [28] Field, D., "Laplacian smoothing and Delaunay triangulations," *Communications in Applied Numerical Methods*, vol. **4**, pp. 709–712, 1988.
- [29] Freitag, L.A., "On Combining Laplacian And Optimization-Based Mesh Smoothing Techniques," In: *Trends in Unstructured Mesh Generation*, pp. 37-43, 1997.
- [30] Vollmer, J., Mencl, R., and Müller, H., "Improved Laplacian smoothing of noisy surface meshes," *Computer Graphics Forum*, vol. **18**, no. 3, pp. 131-138, 1999.
- [31] Mukherje, N., "A Hybrid, variational 3D smoother for orphaned shell meshes," In *Proc. 11th International Meshing Roundtable*, Ithaca, New York, Sep.15-18 2002.
- [32] Chen, L., "Mesh smoothing schemes based on optimal Delaunay triangulations," In *Proc. 13th International Meshing Roundtable*, Williamsburg, VA, Sandia National Laboratories, SAND #2004-3765C, pp.109-120, Sep. 19-22, 2004.
- [33] Garimella, R.V., Shashkov, M.J., and Knupp, P.M., "Triangular and Quadrilateral Surface Mesh Quality Optimization Using Local Parametrization," *LA-UR-02-7190*, Nov. 2002.
- [34] Erten, H., Ungor, A., and Zhao, C., "Mesh Smoothing Algorithms for Complex Geometries," in: B. W. Clark (ed.), *Proc. 18<sup>th</sup> Int. Meshing Roundtable*, Springer-Verlag, Berlin-Heidelberg, 2009, pp. 175-193.
- [35] Garland, M. and Heckbert, P.S., "Surface simplification using quadric error metrics," *SIGGRAPH '97 Proceedings of the 24th Annual Conference on Computer Graphics and Interactive Techniques*, pp. 209-216, NY, 1997.
- [36] P.-O. Persson and G. Strang, "A Simple mesh generator in MATLAB," *SIAM Review*, vol. 46, no. 2, pp. 329-345, June 2004.
- [37] J. D. Foley, A. van Dam, S. K. Feiner, and J. F. Hughes, *Computer Graphics: Principles and Practice in C*, Addison-Wesley Professional, 1996, 2<sup>nd</sup> ed.

- [38] MATLAB codes by Mr. Bruce R. Land of Cornell University, Online: <http://www.nbb.cornell.edu/neurobio/land/projects/hierarchy/>
- [39] M. Chen and J. V. Tucker, "Constructive volume geometry," *Computer Graphics Forum*, vol. 19, no. 4, pp. 282-293, 2000. Online: [http://www-compsci.swan.ac.uk/~csjvt/JVTPublications/CVG-Forum\(published\).pdf](http://www-compsci.swan.ac.uk/~csjvt/JVTPublications/CVG-Forum(published).pdf)
- [40] S. H. Lo and W. X. Wang, "A fast robust algorithm for the intersection of triangulated surfaces," *Engineering with Computers*, vol. 20, pp. 11–21, 2004.
- [41] A. H. Elsheikh and M. Elsheikh, "A reliable triangular mesh intersection algorithm and its application in geological modelling," *Engineering with Computers* vol. 30, pp. 143–157, 2014.
- [42] L. C. Coelho, M. Gattass, and L. H. De Figueiredo, "Intersecting and Trimming Parametric Meshes on Finite-Element Shells," *Int. J. for Numerical Methods in Engineering*, vol. 0(0), 1–100, 1999.
- [43] W. M. Lira, L. C. G. Coelho, and L. F. Martha, "Multiple Intersections of Finite-Element Surface Meshes," *11th International Meshing Roundtable*, Ithaca, New York, USA, Sep. 15-18, 2002.
- [44] O. Devillers and P. Guigue, "Faster Triangle-Triangle Intersection Tests," Institut National de Recherche en Informatique et en Automatique, Preprint # 4488, June 2002.
- [45] T. Möller and B. Trumbore, "Fast, Minimum Storage Ray/Triangle Intersection", *Journal of Graphics Tools*, 2(1):21—28, 1997.
- [46] D. Badouel, "An Efficient Ray-Polygon Intersection", *Graphics Gems*, pp. 390-393.
- [47] T. Möller, "A Fast Triangle-Triangle Intersection Test," Online: <http://web.stanford.edu/class/cs277/resources/papers/Moller1997b.pdf>
- [48] J. Tuszynski, "Triangle/Ray Intersection," Online: <http://www.mathworks.com/matlabcentral/fileexchange/33073-triangle-ray-intersection>
- [49] J. P. Mena-Chalco, "Ray/Triangle Intersection," Online: <http://www.mathworks.com/matlabcentral/fileexchange/25058-ray-triangle-intersection>
- [50] T. Watanabe, Y. Kuno, and Y. Uchikawa, "Robustness of the boundary integral equation method for potential problems," *IEEE Trans. Magnetics*, vol. 26, no. 2, pp. 610-613, March 1990.
- [51] C. A. Brebbia, J. C. F. Telles, and L. C. Wrobel, *Boundary Element Techniques, Theory, and Applications in Engineering*, Springer-Verlag, Berlin-Heidelberg, 1994.
- [52] M. Bachtold, M. Emmenegger, J. G. Korvink and H. Baltes, "An error indicator and automatic adaptive meshing for electrostatic boundary element simulations," *IEEE Tran. Computer-Aided Design of Integrated Circuits and Systems*, vol. 16, no. 12, pp. 1439-1446, Dec. 1997.
- [53] D.-K. Park, C.-H. Ahn, S.-Y. Lee, and J.W. Ra, "Adaptive mesh refinement for boundary element method and its application to stripline analysis," *IEEE Trans. on Magnetics* , vol. 26, no. 2, pp. 783-786, March 1990.
- [54] M. Liang, J. Chen, and S. Yang, "Error estimation for boundary element method," *Engineering Analysis with Boundary Elements*, vol. 23, pp. 257-265, 1999.
- [55] V. Jandhyala, S. Savage, and Z. Cendes, "Efficient capacitance computation for structures with non-uniform adaptive surface meshes," *Presented at 36th Annual ACM/IEEE Design Automation Conference*, 1999.



- [56] N. Kamiya, Y. Aikawa, and K. Kawaguchi, "Adaptive boundary element for the problem with mixed boundary condition," In: C. A. Brebbia, S. Kim, T. A. Osswald, and H. Power, Eds., *Boundary Elements XVII*, WIT, 1995.
- [57] M. Aurada, M. Ebner, S. Ferraz-Leite, M. Mayr, P. Goldenits, M. Karkulik, and D. Praetorius, "HILBERT — A Matlab implementation of adaptive BEM, ASC Report 44/2009, Wien, Austria. Online: <http://www.asc.tuwien.ac.at/abem/hilbert/>
- [58] M. Aurada, S. Ferraz-Leite, P. Goldenits, M. Karkulik, M. Mayr, and D. Praetorius, "Convergence of adaptive BEM for some mixed boundary value problem," *ASC Report No. 12/2010*, Wien, Austria. Online: <http://www.asc.tuwien.ac.at/preprint/2010/asc12x2010.pdf>
- [59] S. M. Rao, T. K. Sarkar, and R. G. Harrington, "The electrostatic field of conducting bodies in multiple dielectric media," *IEEE Trans. Microwave Theory Tech.*, vol. 32, no. 11, Nov. 1984, pp. 1442-1448.
- [60] W. R. Smythe, *Static and Dynamic Electricity*, McGraw Hill, New York, 1950, p. 114.
- [61] J. D. Jackson, *Classical Electrodynamics*, Wiley, New York, 1975, p. 128, problem 3.3.

## Chapter 3

# Mesh generation and operation tools developed in MATLAB

### Outline of segmentation/surface reconstruction workflow in MATLAB

This chapter details the process used for the development and construction of the VHP – Female model using MATLAB and describes the MATLAB operation tools which form the building blocks of the mesh generation. The work flow for the generation of meshes is robust and rapid compared to the prior VHP – Female model discussed in section 1.2.

The process of segmentation and mesh conditioning are made user friendly which ensures quick generation of manifold watertight meshes for each tissue. Use of custom made MATLAB scripts gives user the flexibility and control in every aspect of mesh generation. Fig 3.1 shows the summary of stages in the development of the VHP – Model using MATLAB.

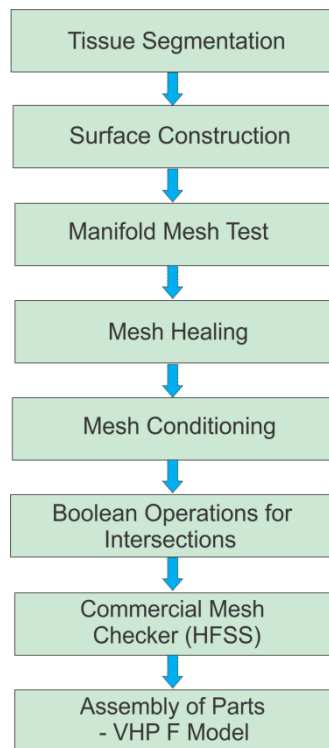


Fig.3.1 Summary of stages in the development of prior VHP – Female Model

The latest basic MATLAB platform (without toolboxes) has a number of built-in and open-source features that makes it an accessible alternative for medical image segmentation and surface reconstruction. These features relate to both computational geometry and image processing. In particular, they include (compatibility with R2015a):

- Pixel-based image processing tools: resampling, registration, mouse I/O (functions *imread*, *imagesc*, *ginput*);
- 3D Delaunay triangulation or tetrahedralization, constrained and unconstrained 2D Delaunay triangulations (*delaunay*, *triangulation*);
- 3D surface mesh generation via a sculpting based volumetric method [17] or a region-growing surface method – the ball-pivoting method [25] (an excellent function *MyRobustCrust* by Dr. L. Giaccari);
- 3D surface-preserving mesh decimation (via the function *reducepatch*)
- Interactive mesh processing tools such as selection of vertices or triangles of a 3D surface mesh and visualization of multiple meshes in many different formats (function *select3d* by Dr. J. Conti).

The goal of the present study has been to establish a segmentation and surface reconstruction workflow to enhance and augment the VHP-Female model entirely in MATLAB. The corresponding workflow, separated into short MATLAB scripts, is outlined in Fig. 3.2 and includes:

- Data acquisition (scan data) of the body in the xy-plane using one of a set of images;
- Manual mouse selection of nodes indicating a boundary of interest (segmentation) using 2D mouse input *ginput*. Left click adds a nodal point; right click deletes the previous node, hitting return acquires the next image;
- 3D surface mesh generation via the ball-pivoting method as implemented in the function *MyRobustCrust*;
- Automatic selection and visualization of edges with only one adjacent triangle (hole boundaries) and with more than two adjacent triangles (non-manifold edges);

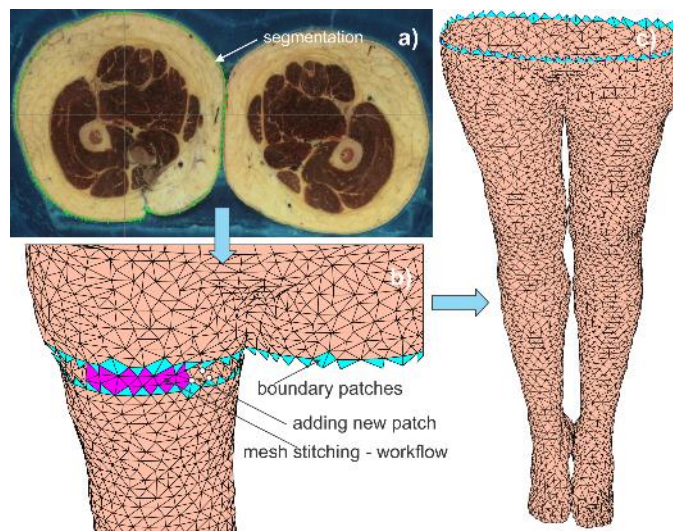


Fig.3.2 Illustration of the segmentation/mesh generation workflow: a) – segmentation; b) – stitching of two individual surface meshes; c) – semi-complete surface mesh.

- Sequential selection of individual triangles/nodes/edges using function `select3d`. Manual removal/addition of selected triangles, mesh stitching, mesh healing;
- Mesh smoothing and mesh coarsening using `reducepatch`.

The following sections explain in detail the process involved in the development of the current VHP – Female Model.

### ***3.1. Segmentation and Surface reconstruction***

The medical images from the VHP database discussed in section 1.1.1 are selected based on the objects to be segmented. The script sets the co-ordinate system for the VHP – Female model and generates vertices based on the same. The resolution of the mesh generated can be controlled by choosing the step size in the image set. The image set comprises of slides from start to the end of the tissue. This allows the user the flexibility to generate meshes as high as  $0.33 \times 0.33 \times 0.33 \text{ mm}^3$  resolution voxels or any other desired low definition objects.

Image processing based functions such as `imread`, `imagesc` are used to read the data and set the co-ordinate axes limits. Function `ginput` is used to read the pixel data from the sampling of nodes which are later converted to vertices based on the co-ordinate system. The segmentation process is illustrated in Fig. 3.2a.

Additionally, zoom option can also be enabled based on the user requirement when accuracy is desired. The segmentation script results in a surface point cloud. The ball-pivoting method [25] based *MyRobustCrust* was used for 3D mesh generation. This resulted in surface based objects representing the respective tissue. As discussed before this object is defined by matrices P, t. This object can be viewed using the `patch` function. The script which does the segmentation with zoom option enabled is `main_direct_zoom.m`.

### ***3.2. Mesh test for manifoldness***

A MATLAB based custom function `mesh_edges.m` returns the set of non manifold edges and other boundary edges which result in mesh being non manifold and not watertight. This is based on the number of triangles present at each edge. If only one triangle is present at the edge, it is a boundary edge and if more than two triangles are present at the edge then it is defined as a non manifold edge.

These edges are highlighted on the object when displayed, enable the user to identify the area of concern and also returns an error message. Illustration of non manifold edges and boundary edges present during healing of intestine is displayed through virtual plotting in Fig 3.3.

If the mesh generated from step 3.1 is manifold, then no errors are displayed and we can proceed to deal mesh intersections and to perform mesh conditioning to achieve the desired mesh size and quality. If non manifold, we need to fix the errors to make the edges manifold and close and holes and make the object water tight.

### 3.3. Healing the object

The object which fails the manifold test has to undergo healing to make it manifold and water tight. The function *select3d* enables the user to built interactive mesh processing tools such as selection of vertices or triangles of a 3D surface mesh and visualization of multiple meshes in different formats. This function is used to select the highlighted non manifold vertices and non manifold faces obtained from the process as explained earlier in section 3.2.

The selections are then deleted, which create holes in the structure. These holes can be patched by adding new triangles as shown in Fig.3.2b. The addition or removal of triangle would require selecting the vertices of the triangle under consideration. For edges which are present in crevices, we can adopt a method of virtual plotting the selected area which would enable the user to perform actions in selected and inaccessible regions. Virtual plotting is used to open up the interior areas of the Intestine as depicted in Fig. 3.3.

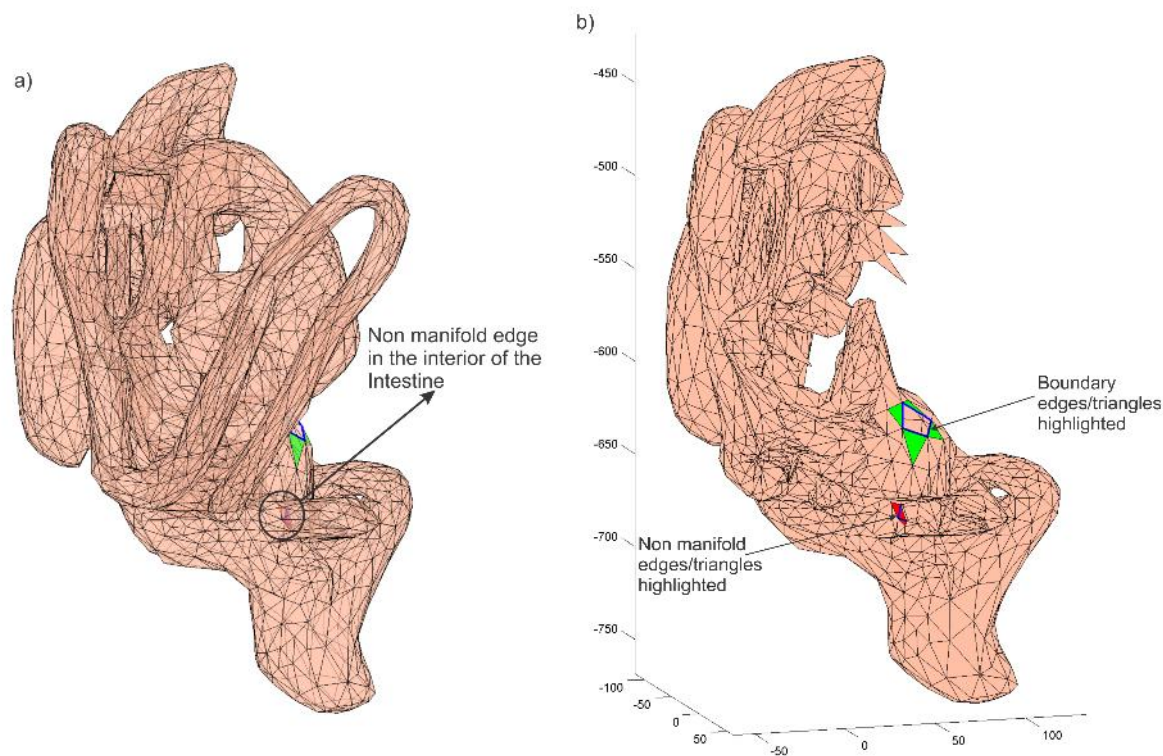


Fig 3.3 Illustration of non manifold edges and boundary edges present during healing of intestine displayed through virtual plotting. a) non manifold edge in the interior region of the intestine is not accessible as shown b) - the non manifold edge is now accessible through virtual plotting of the cut open intestine.



The idea of adding triangles can be extended to stitch meshes together as shown in Fig. 3.2b. This would enable one to manually stitch two sheets together. Boolean addition can automatically be applied if they are manifold structures. Other Boolean operations such as intersection, subtraction can also be performed on the meshes to be discussed in section 3.5.

After all the non manifold features are removed we ensure the mesh passes the manifold test and is watertight.

### 3.4. Mesh Conditioning

The manifold mesh obtained can be reduced to a lower resolution which contains smaller number of triangles to optimize the computational time. This mesh coarsening can be achieved using MATLAB inbuilt function *reducepatch*, which reduces the number of faces while trying to preserve the overall shape. The reduction can be specified as a factor ranging from 0 – 1 or by the targeted number of triangles. This feature is illustrated in the Fig. 3.4, where the original surface mesh after segmentation is shown in Fig 3.4a and the surface mesh after healing and patch reduction is shown in Fig 3.4b.

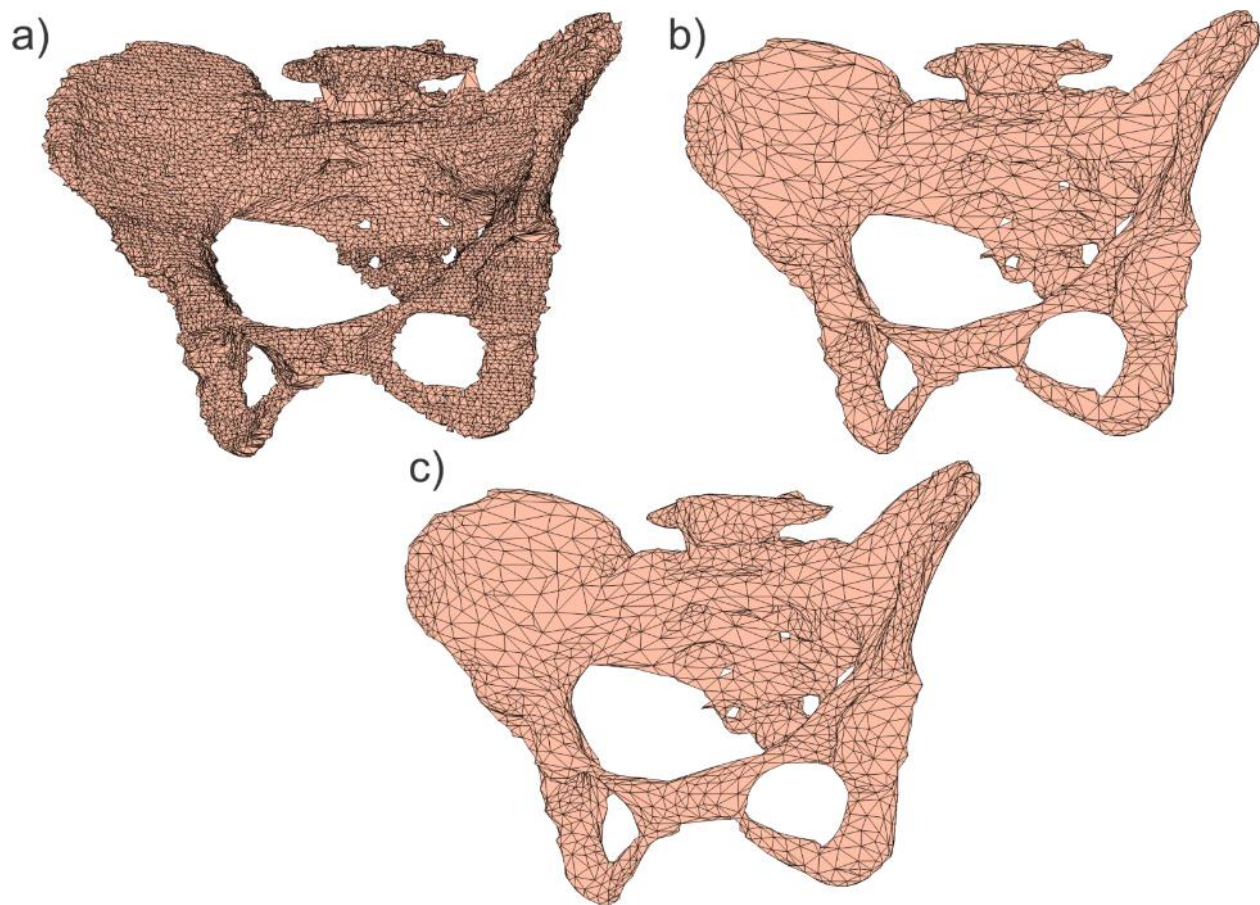


Fig 3.4 Illustration of the mesh conditioning workflow for pelvic girdle: a) – original surface having approx. 44,000 triangles; b) – Surface mesh after healing and decimation having approx. 6,500 triangles; c) –surface mesh after two iterations of HC smoothing.

The mesh having the desired resolution is obtained and the mesh quality is tested. The mesh quality and mesh smoothing algorithms are discussed in Chapter 2. In particular, surface-preserving (HC) Laplacian smoothing [3] is preferred as it preserves the surface topology with minimal shrinkage and deformation. The number of iterations and weights  $\alpha$ ,  $\beta$  can be specified for each operation. A default optimized values of  $\alpha = 0.1$  and  $\beta = 0.6$  were used for HC smoothing. An illustration of this is shown in Fig 3.4c, which is the product after applying two HC smoothing iterations to the surface mesh in Fig 3.4b.

The mesh of desired resolution and acceptable triangle quality is obtained. This mesh before being finalized and added to the VHP – Female model, has to be made sure that it is not intersecting with any of the neighboring tissues. Most of the commercially available solvers can fix intersecting meshes. The caveat is, for example HFSS, introduces a large number of small triangles at the intersecting junction, and this results in an increase in the computational time. Hence we resort to doing the Boolean operations in MATLAB to be discussed in section 3.5.

### ***3.5. Mesh intersection algorithm for 2 manifold triangular meshes via constrained 2D Delaunay triangulation***

An important problem in human body segmentation is related to intersections of meshes describing different tissues after surface reconstruction. Public-domain MATLAB codes that implement one of the existing intersection algorithms were not found [4]-[9]. An original algorithm has therefore been developed and tested. In contrast to the classic paper [4] and other relevant sources [5], [6], [9], we do not explicitly construct the chains and loops of intersection line segments. Instead, all individual intersection line segments are collected randomly and then a constrained 2D Delaunay triangulation is applied to each triangle with the intersection line segments separately. Note that the constrained 2D Delaunay triangulation was also used in [9], but augmented with the construction of intersection chains. The algorithm steps are as follows (the goal is to subtract a manifold Y from a manifold X):

- For every edge of mesh X, find the triangle(s) of mesh Y intersected by this edge and the corresponding intersection points via Möller & Trumbore algorithm [10] vectorized in MATLAB. Store the results in two distinct cell arrays.
- Swap meshes X and Y and perform the same operation.
- For every triangle of mesh X falling into the intersection list, collect all extra line segments (node pairs) to be added. Three scenarios are possible. The first is when *two* edges of a triangle in Y intersect the triangle in X. A line segment  $Q_{11}Q_{12}$  in Fig. 3.5 has to be added. The second scenario is when only *one* edge of a triangle in Y intersects the triangle in X. Then, an edge of the triangle in X must also intersect this triangle in Y. A line segment  $Q_{21}Q_{22}$  in Fig. 3.5 has to be added. The last scenario is when two edges of the triangle in X intersect a certain triangle in Y. A line segment  $Q_{31}Q_{32}$  in Fig. 3.5 has to be added. Finally, store all results in a cell array.

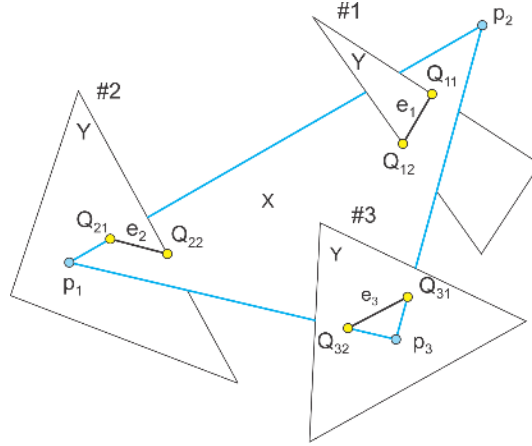


Fig.3.5 Three types of triangle intersections between a master mesh X and various triangles of a slave mesh Y. Cases #1 and #3 are equivalent if we treat the master and slave meshes as one set of triangles.

- Swap meshes X and Y and perform the same operation.
- For every triangle of mesh X falling into the intersection list, remove duplicated nodes/remunerate the constrained line segments using function `unique` with three arguments and perform constrained 2D Delaunay triangulation in MATLAB in the triangle plane. The local orthogonal coordinate system includes one (the longest) triangle edge as an x-axis. Remove sub-triangles of vanishingly small areas, which are routinely produced when multiple (intersection) points are located on the same edge of the triangle in X.
- Collect all sub-triangles in X and create a new refined mesh XR, which respects all the intersection segments and does not have duplicated points.
- Swap meshes X and Y and perform the same two previous operations.
- Using the original manifold X, determine all triangles YX of the refined mesh YR in X. Use the Möller & Trumbore algorithm [10] for triangle centers.
- Using the original manifold Y, determine all triangles XY of the refined mesh XR not in Y. Use the Möller & Trumbore algorithm [10] for triangle centers.
- Combine meshes XY and YX, eliminate duplicated points, and obtain the conformal mesh X–Y.
- Check if the mesh X–Y is a 2 manifold mesh without holes.

The above algorithm in its present form is straightforwardly programmed in MATLAB and shows a high reliability. It produces an exact representation of any curved intersecting surfaces. At the same time, it is yet to be optimized for speed and for handling of some degenerate cases. The default MATLAB precision is used. Two expected and undesirable results of this algorithm include potential reduction in the triangle quality due to the possible generation of low-quality (highly skewed) triangles and in an increase in the overall mesh size, which may be substantial for small-size meshes.



Vertices of intersecting meshes X and Y located in close proximity are the major source of both problems. Therefore, one way to address both issues identified above is to make those vertices coincident at the onset of the algorithm, immediately after identifying the intersections.

Yet another way is to apply mesh decimation on flat surfaces followed by local Laplacian smoothing, which slightly shrinks the selected surfaces in the direction of the inner surface normal vector. This operation leaves a gap between the intersected meshes. Since the distinct organ meshes are in fact separated by thin tissues, such a gap may be anatomically correct.

Fig. 3.6 shows a mesh intersection example. Fig. 3.6a indicates two intersecting meshes: white matter and CSF ventricles. Fig. 3.6b shows coincident faces created for both meshes after the intersection algorithm completes and simultaneously the white matter mesh after subtraction. Fig. 3.6c indicates degradation in triangle areas of the white matter mesh after the subtraction; Fig. 3.6d gives similar results for the triangle quality (defined as twice the ratio of incircle to circumcircle) of the white matter mesh.

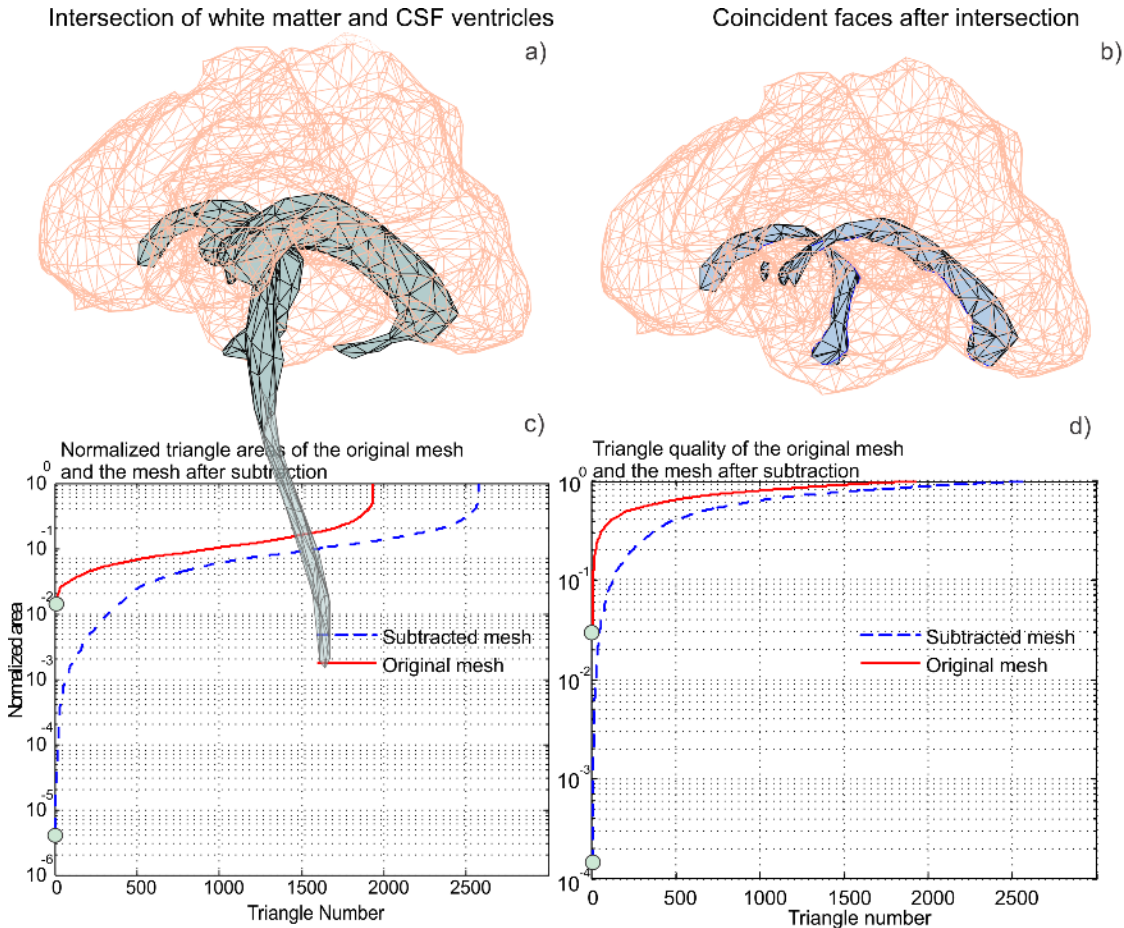


Fig.3.6 Image intersection results for white matter and CSF ventricles meshes.

It is recommended to perform manifold test on the mesh after Boolean operation are performed. The present algorithm in particular does not introduce any non-manifold features or holes, but these anomalies might occur due to that particular mesh structures under Boolean operation.

### ***3.6. Generation of mesh normals***

The Möller & Trumbore algorithm was implemented for ray to triangle intersection and segment to triangle intersection. This can be extended to find the outer normals of a mesh under study. The algorithm is applied to triangle centers where the ray originates. Then the intersection points of that ray with the mesh itself are used to determine if it is the inner or the outer normal. Zero or even numbers of intersection points imply that the assumed direction of the ray is the outer normal. In case of odd number of intersection points, it is the inner normal and its direction has to be reversed. The direction of outer normal is critical for various computations, for example, to check if a point is present inside or outside a mesh structure (in – out status check). An example illustration of outer normals for femur is shown in Fig. 3.7.

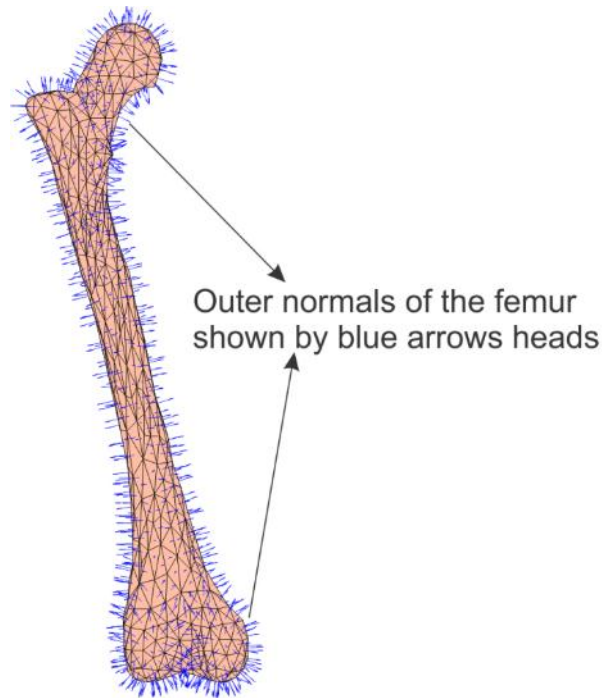


Fig.3.7 Illustration of outer normal(s) for the femur bone. Arrow heads depict the direction.

### ***3.7. Assembly and file format of tissues***

The meshes obtained are now manifold, watertight and are intersection free from the neighboring tissues. These meshes are now defined by point cloud ' $P$ ', connectivity matrix ' $t$ ', and respective

normals for each face defined by ‘*normals*’. Now, these meshes can be converted into any other format which is compatible with commercial software packages.

We have converted our meshes into NASTRAN format which is widely used across different software packages. It is noteworthy to mention that when converting from one format to another, the precision of the mesh might change and can result in error such as face errors, where two faces of the same mesh intersect. Hence it is advisable to maintain the precision to ensure the mesh remains manifold even after the file format transformation. A precision of up to three decimal places were used when converting the MAT file into the NASTRAN file and the same applies for file conversion into STL format.

The meshes are converted to desired format and then are assembled. Chapter 05 discusses the details of the 81 tissues such as the triangle number, material and mesh quality for both high definition and low definition meshes present in the complete VHP – Female model.

## ***References***

- [1] C. Bajaj, F. Bernardini, G. Xu, Automatic reconstruction of surfaces and scalar fields from 3D scans, Computer Graphics Proceedings, 1995, Annual Conference Series. Proceedings of SIGGRAPH 95, pp. 109–118.
- [2] F. Bernardini, J. Mittleman, H. Rushmeier, C. Silva, G. Taubin, The ball pivoting algorithm for surface reconstruction, IEEE Trans. Visualization and Computer Graphics, vol. 5, no 4 (Oct-Dec. 1999).
- [3] J. Vollmer, R. Mencl, H. Mueller, Improved Laplacian smoothing of noisy surface meshes, Eurographics. vol. 18 (1999) 1-8.
- [4] S. H. Lo, Automatic mesh generation over intersecting surfaces, Int. J. Numerical Methods Eng., vol. 38 (1995) 943–954.
- [5] S. H. Lo and W. X. Wang, A fast robust algorithm for the intersection of triangulated surfaces, Engineering with Computers, vol. 20 (2004) 11–21.
- [6] A. H. Elsheikh, M. Elsheikh, A reliable triangular mesh intersection algorithm and its application in geological modelling, Engineering with Computers, vol. 30 (2014) 143–157.
- [7] L. C. Coelho, M. Gattass, L. H. De Figueiredo, Intersecting and Trimming Parametric Meshes on Finite-Element Shells, Int. J. for Numerical Methods in Engineering, vol. 0(0) (1999) 1–100.
- [8] W. M. Lira, L. C. G. Coelho, L. F. Martha, Multiple Intersections of Finite-Element Surface Meshes, 11th International Meshing Roundtable, Ithaca, New York, USA, Sep. 15-18, 2002.
- [9] C.H. Lindenbeck, H.D. Ebert, H. Ulmer, L. Pallozzi Lavorante, R. Pflug, TRICUT: a program to clip triangle meshes using the rapid and triangle libraries and the visualization toolkit, Computers & Geosciences, vol. 28 (2002) 841–850.
- [10] T. Möller and B. Trumbore, Fast, Minimum Storage Ray/Triangle Intersection, J. of Graphics Tools, vol. 2 (1997) 21–28.

## Chapter 4

### The VHP – Female computational model to date

#### Assembly of parts

The meshes obtained as a result of processes explained in Chapter 3 are assembled to create the VHP – Female Model. The meshes have been categorized as high definition and low definition versions based on the triangle number of the respective object. The number of tissues available to date in the inventory is 81 and is expanding. Table 4.1 summarizes the details of the high and low definition model meshes such as mesh quality, material and average area.

#### 4.1. High definition model

The meshes after initial segmentation and surface construction have the highest number of triangles. The resolution depends on the data sampling of the images and the segmentation efforts. High definition meshes are often computational burden and lead to the development of low definition meshes. High definition meshes can be used selectively depending on the application under study. Table 4.1 summarizes the details of the high definition model meshes such as mesh quality, material and average area. Selected high definition meshes have been illustrated in Table. 4.2.

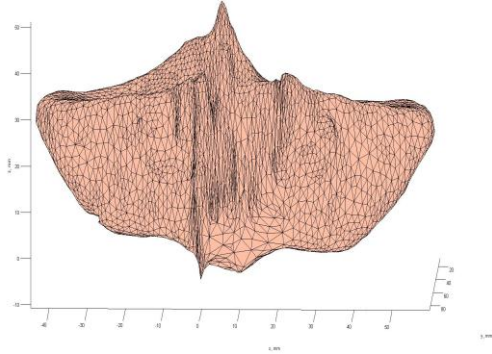
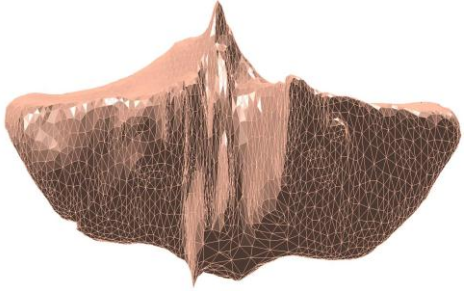
Table 4.1 Individual tissues of the VHP-Female model. HD stands for higher-definition meshes; LD stands for lower-definition (decimated and smoothed) meshes. Average triangle area is given. The meshes are given before intersections (if any).

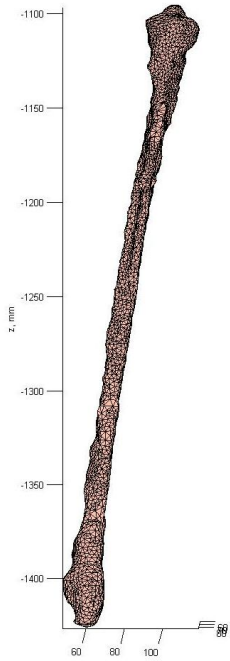

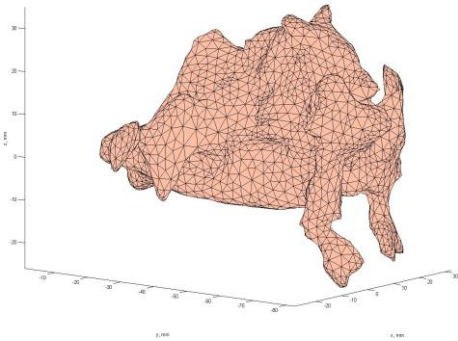
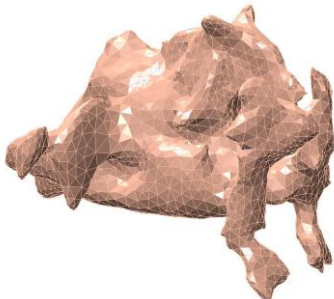
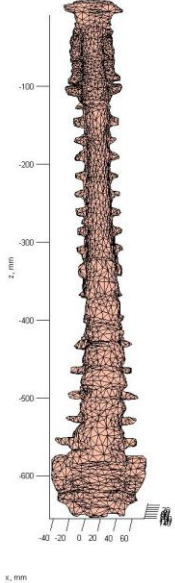

Organ	Type of tissue	Mesh size (HD)	Mesh Quality (HD)	Average area (mm <sup>2</sup> )	Mesh size (LD)	Mesh Quality (LD)	Average area (mm <sup>2</sup> )
Aorta	Organ	3874	0.2315	552	2018	0.0176	687
Brain(Grey matter)	Organ	2992	0.0707	414	2992	0.0707	414
Brain(White matter)	Organ	4838	0.3861	241	1934	0.0312	406
Calcaneus left	Bone	622	0.0543	6932	622	0.0543	6932
Calcaneus right	Bone	618	0.3734	5231	618	0.3734	5231
Calf left	Muscle	1888	0.1717	5816	944	0.1980	7496
Calf right	Muscle	2022	0.0855	6324	1010	0.1831	8178
Cerebellum	Organ	7998	0.0106	79	516	0.0615	220
CSF Shell	Organ	2992	0.1804	477	2992	0.1804	477
CSF Ventricles	Organ	832	0.0075	207	832	0.0075	207
Eye left	Organ	540	0.3823	184	216	0.2286	333
Eye right	Organ	510	0.3611	160	204	0.5260	287
Femur left	Bone	1000	0.0316	5730	1000	0.0316	5730

<b>Organ</b>	<b>Type of tissue</b>	<b>Mesh size (HD)</b>	<b>Mesh Quality (HD)</b>	<b>Average area (mm<sup>2</sup>)</b>	<b>Mesh size (LD)</b>	<b>Mesh Quality (LD)</b>	<b>Average area (mm<sup>2</sup>)</b>
Femur right	Bone	1000	0.0274	5417	1000	0.0274	5417
Fibula left	Bone	7504	0.2019	1870	2100	0.0011	3320
Fibula right	Bone	5880	0.2583	1891	2048	0.0028	3075
Gluteus left	Muscle	4522	0.0607	3927	2024	0.1404	5192
Gluteus right	Muscle	2480	0.0285	3379	2480	0.0285	3379
Hamstring left	Muscle	4898	0.4265	3678	2448	0.0383	4634
Hamstring right	Muscle	4672	0.2748	4130	2522	0.0128	5045
Heart	Organ	3988	0.1251	1083	2990	0.0240	1246
Humerus left	Bone	1766	0.0370	1130	882	0.0344	1732
Humerus right	Bone	1248	0.2208	999	798	0.1902	1156
Intestine	Organ	19096	0.0418	2368	10006	0.0001	3222
Jaw	Bone	1500	0.0900	156	240	0.0587	373
Kidney left	Organ	2838	0.0562	1468	2014	0.0497	1668
Kidney Right	Organ	2162	0.0420	1374	2010	0.0866	1371
Liver	Organ	4616	0.4349	1915	3000	0.0986	2347
Lungs	Organ	4870	0.3068	1589	3018	0.0506	1885
Muscle	Muscle	12580	0.2509	3294	12580	0.2509	3294
Navicular left	Bone	198	0.3619	5524	198	0.3619	5524
Navicular right	Bone	214	0.2936	5572	214	0.2936	5572
Outer Shape	Organ	6506	0.0084	9749	6506	0.0084	9749
Patella left	Bone	318	0.5606	3659	318	0.5606	3659
Patella right	Bone	280	0.6478	4413	280	0.6478	4413
Phalanges L1	Bone	402	0.1657	5498	402	0.1657	5498
Phalanges L2	Bone	676	0.3203	3356	676	0.3203	3356
Phalanges L3	Bone	706	0.2935	2621	706	0.2935	2621
Phalanges L4	Bone	452	0.0198	4471	452	0.0198	4471
Phalanges L5	Bone	1544	0.2013	2139	416	0.1890	3653
Phalanges R1	Bone	1396	0.2168	3107	418	0.1926	5063
Phalanges R2	Bone	1984	0.0615	2024	386	0.1721	3700
Phalanges R3	Bone	436	0.1112	3281	436	0.1112	3281
Phalanges R4	Bone	1450	0.1893	2020	394	0.0414	3190
Phalanges R5	Bone	1366	0.0551	2198	410	0.2315	3342
Pelvic girdle	Bone	10296	0.0002	2708	10296	0.0002	2708
Quadriceps/l	Muscle	2936	0.2986	5484	2936	0.2986	5484
Quadriceps/r	Muscle	2992	0.0792	5041	2992	0.0792	5041
Radius & Ulna	Bone	2000	0.0763	2596	2000	0.0763	2596
Ribs	Bone	9998	0.0003	1895	9998	0.0003	1895
Scapula left	Bone	2602	0.0548	929	2002	0.0781	1031
Scapula Right	Bone	2500	0.0632	676	2000	0.0807	753
Shin left	Muscle	1346	0.0649	6106	1000	0.1545	6539
Shin right	Muscle	1626	0.2877	5260	1000	0.0989	6278

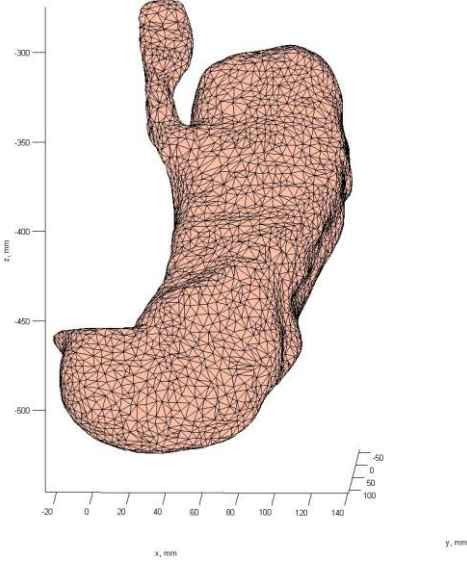

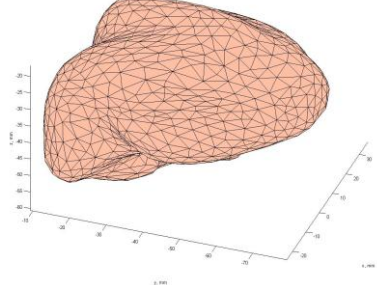
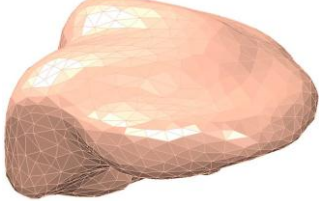
Organ	Type of tissue	Mesh size (HD)	Mesh Quality (HD)	Average area (mm <sup>2</sup> )	Mesh size (LD)	Mesh Quality (LD)	Average area (mm <sup>2</sup> )
Sinus	Cavity	5892	0.1871	78	382	0.0112	301
Skull	Bone	3996	0.0108	596	3996	0.0108	596
Spine	Bone	10252	0.0160	1715	5000	0.001	2615
Stomach	Organ	8714	0.1537	2596	3502	0.0004	1989
Superior Vena Cava	Blood vessel	7048	0.0292	0.00043	1000	0.0831	1.2
Talus left	Bone	720	0.3037	4659	720	0.3037	4659
Talus right	Bone	754	0.3192	4064	754	0.3192	4064
Teeth	Bone	2154	0.0446	68	2154	0.0446	68
Tibia left	Bone	1300	0.1186	5562	1300	0.1186	5562
Tibia right	Bone	1042	0.0581	5850	1042	0.0581	5850
Tongue	Muscle	2000	0.1755	132	320	0.0678	341
Trabecular left	Bone	568	0.1811	2913	568	0.1811	2913

Table 4.2 Selected high definition meshes

Name of tissues:	View 1	View 2
Cerebellum		

<p>Tibia left</p>	 <p>A 3D wireframe model of the left tibia. The vertical axis is labeled 'z, mm' and ranges from -1100 to -1400 in increments of 50. The horizontal axis is labeled 'x, mm' and ranges from 60 to 100. The model shows the bone's structure with a mesh overlay.</p>	 <p>A solid 3D model of the left tibia, rendered in a light brown color. It shows the bone's surface and internal structure without the mesh overlay.</p>
<p>Sinus cavity</p>	 <p>A 3D wireframe model of the sinus cavity. The vertical axis is labeled 'z, mm' and ranges from 0 to 20 in increments of 2. The horizontal axis is labeled 'x, mm' and ranges from -30 to 30. The model shows the cavity's structure with a mesh overlay.</p>	 <p>A solid 3D model of the sinus cavity, rendered in a light brown color. It shows the cavity's surface and internal structure without the mesh overlay.</p>
<p>Spinal cord</p>	 <p>A 3D wireframe model of the spinal cord. The vertical axis is labeled 'z, mm' and ranges from -100 to -600 in increments of 100. The horizontal axis is labeled 'x, mm' and ranges from -40 to 60. The model shows the spinal cord's structure with a mesh overlay.</p>	 <p>A solid 3D model of the spinal cord, rendered in a light brown color. It shows the spinal cord's surface and internal structure without the mesh overlay.</p>



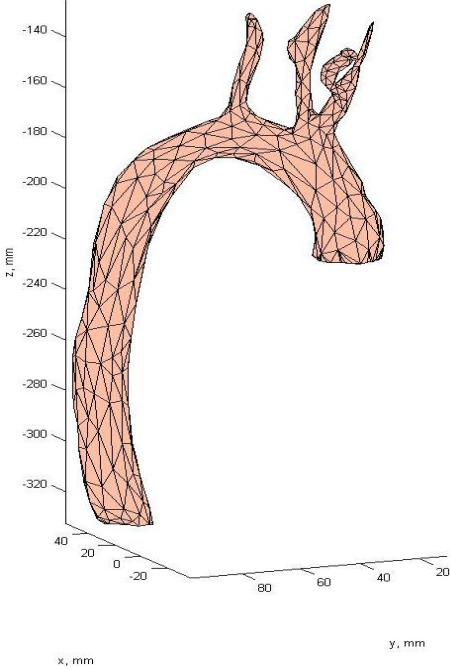
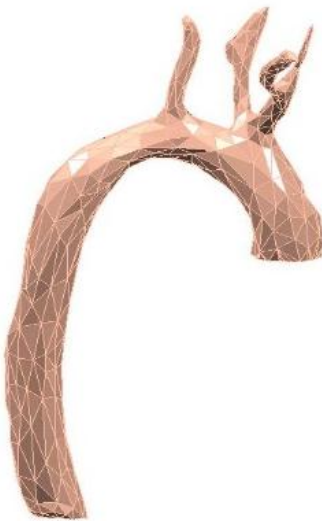
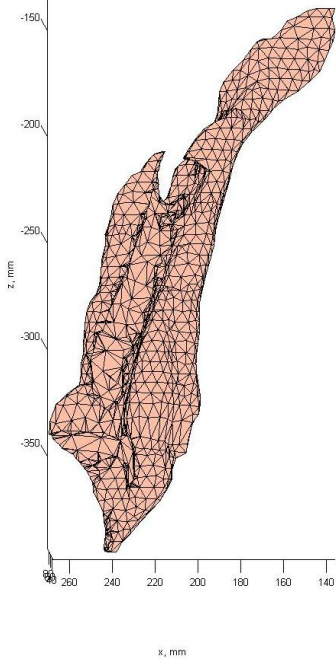
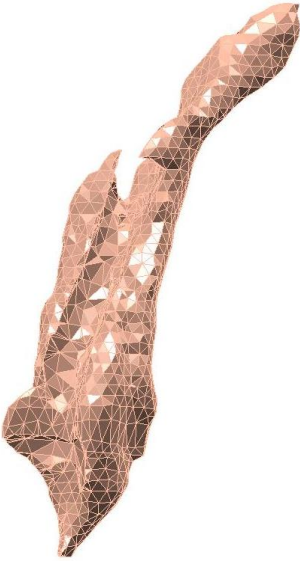
Stomach		
Tongue		

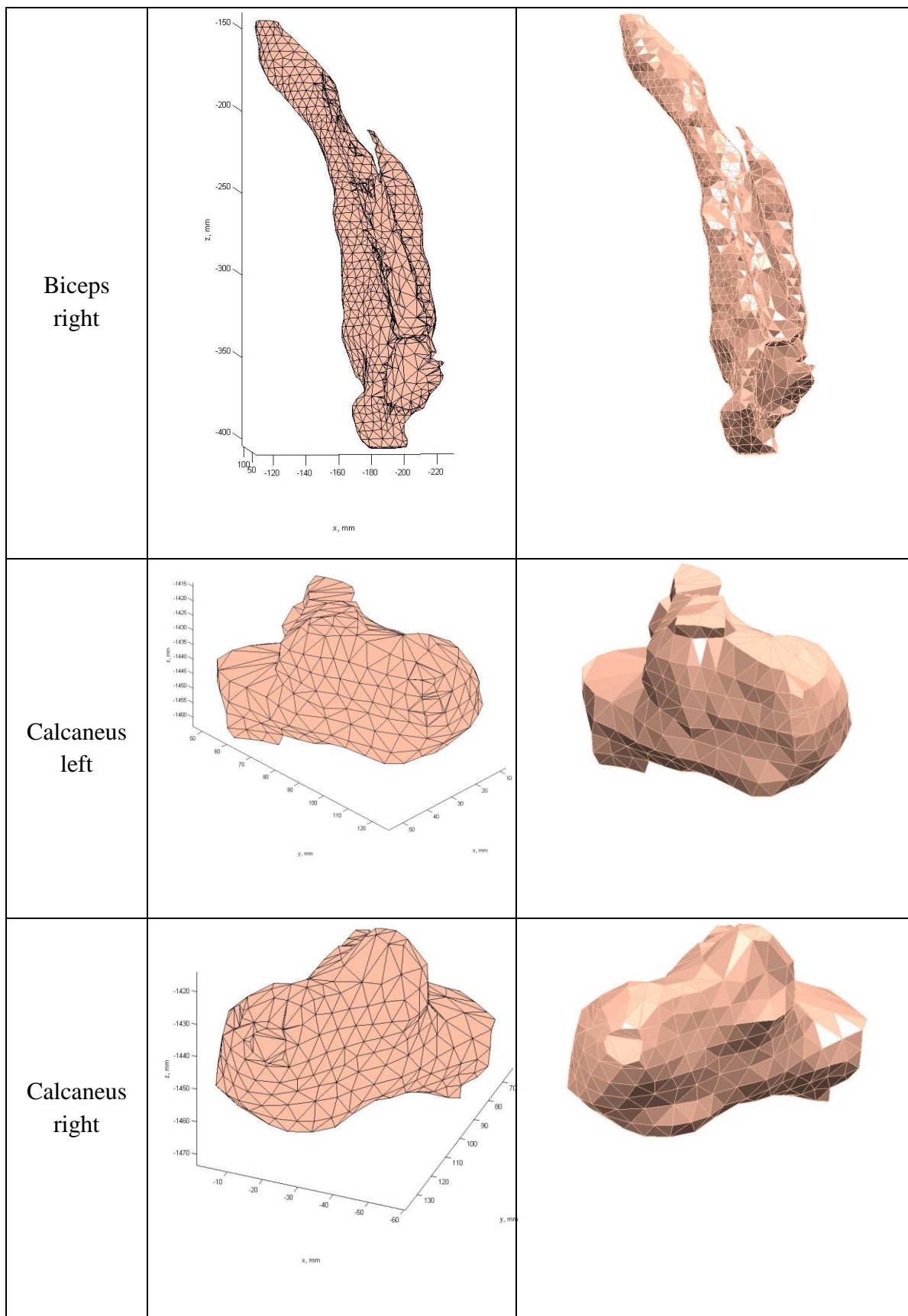
#### 4.2. Low definition model

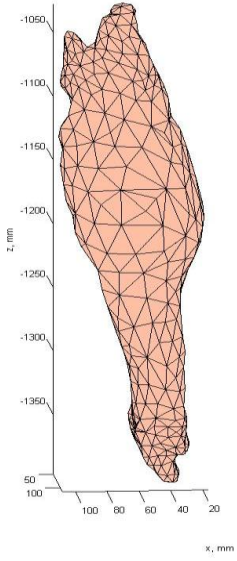

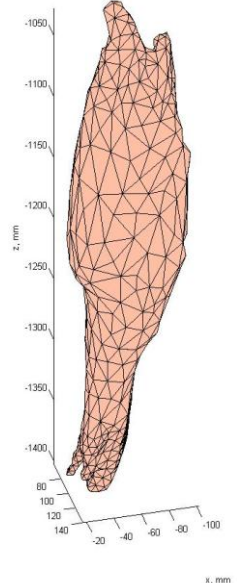
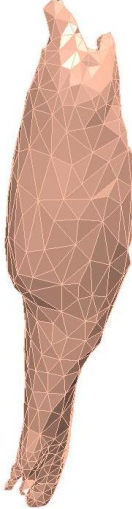
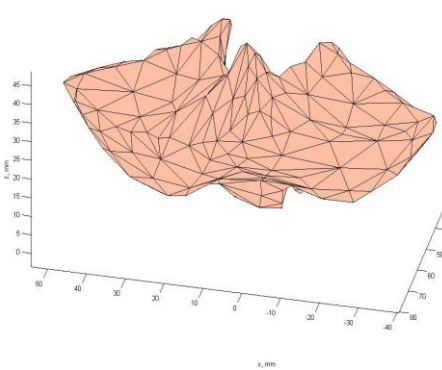

Low definition meshes are the key to achieve reasonable computational time when it comes to triangular based surface meshes. These meshes are made from their respective parent high definition meshes by decimation and smoothing. The reduced computational time comes at a cost – as the number of triangles are reduced, the surface features and topology might have to compromise to an extent. The VHP – Female model with low definition meshes is therefore apt for optimization problems where the number of variables is high and where is a need to quickly run multiple simulations. Table 4.1 summarizes the features of the low definition meshes similar to that of high definition meshes. The entire set of low definition meshes which currently comprise the VHP – Female model are displayed in Table 4.3.

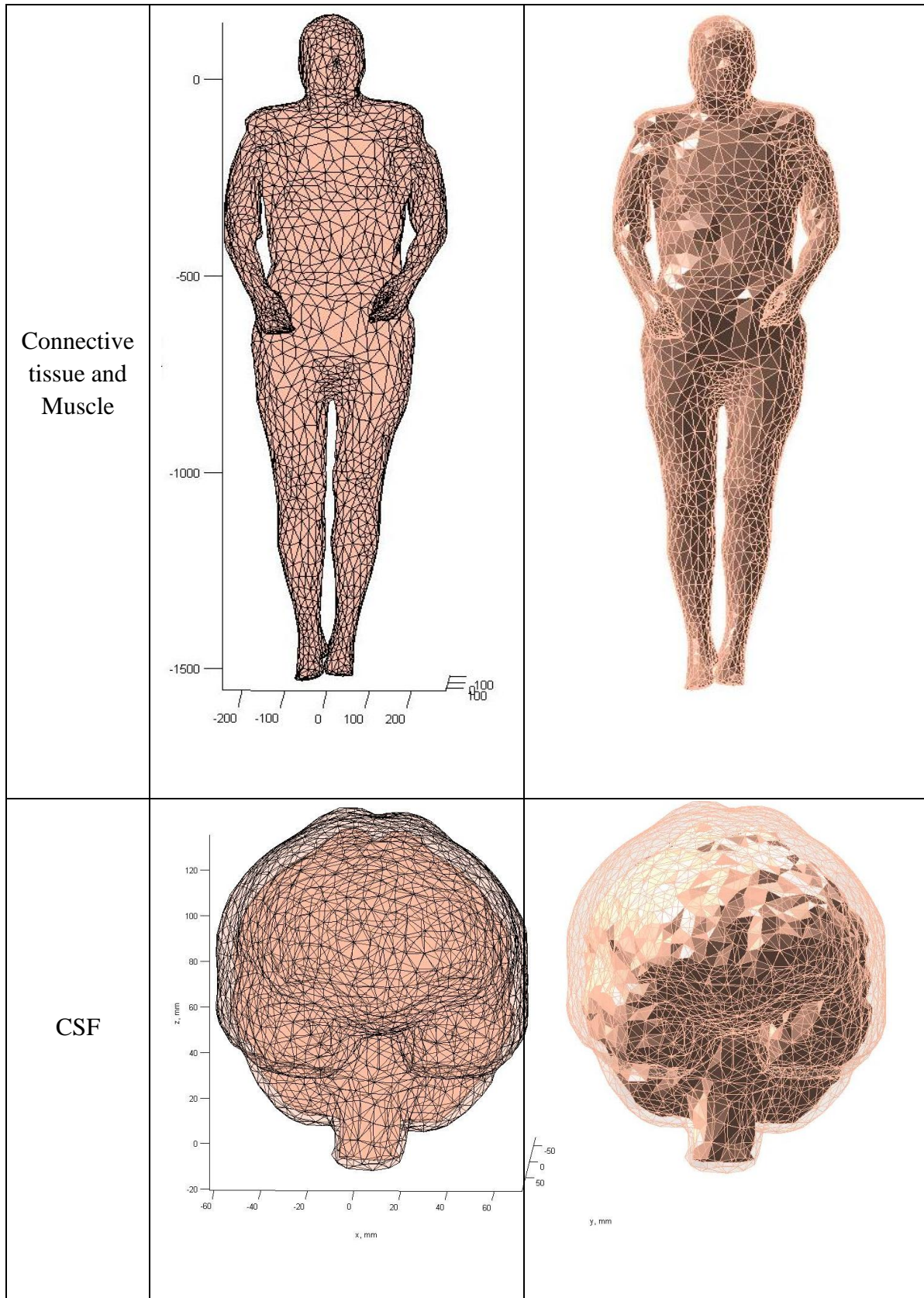


Table 4.3. Table of inventory of low definition tissues

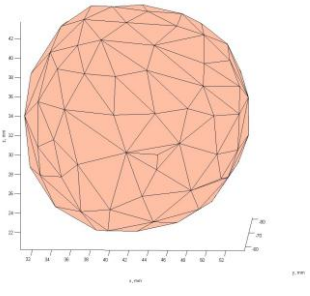
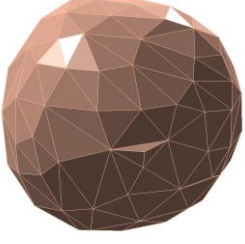
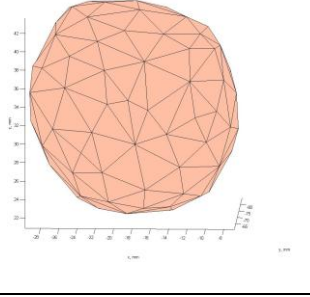
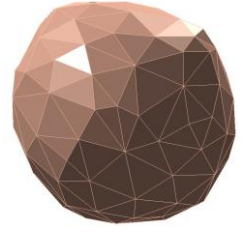
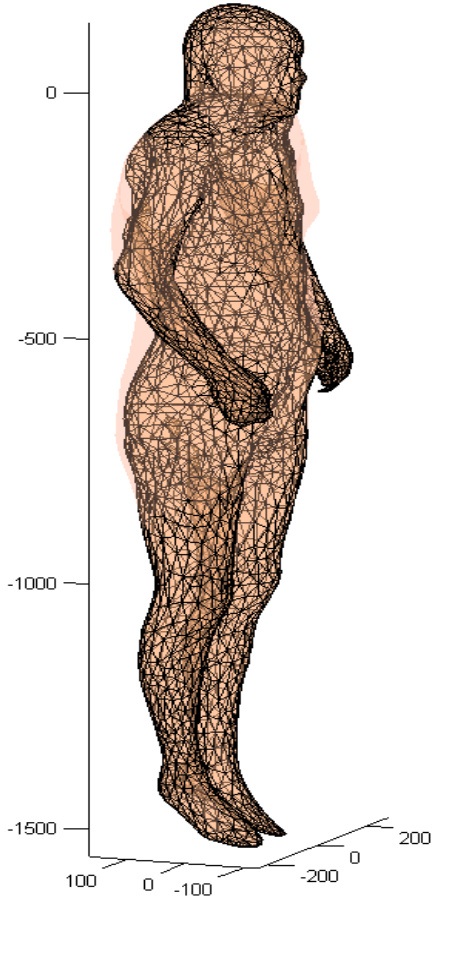

Name of tissues:	View 1	View 2
Aorta		
Biceps left		

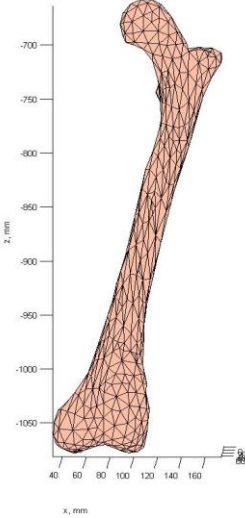

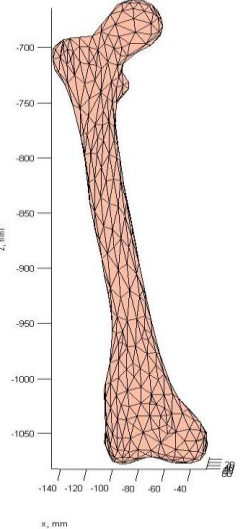

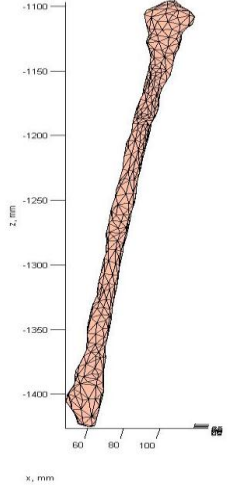



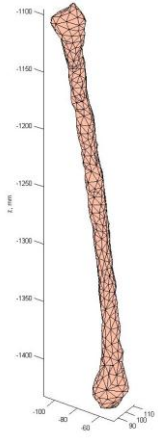

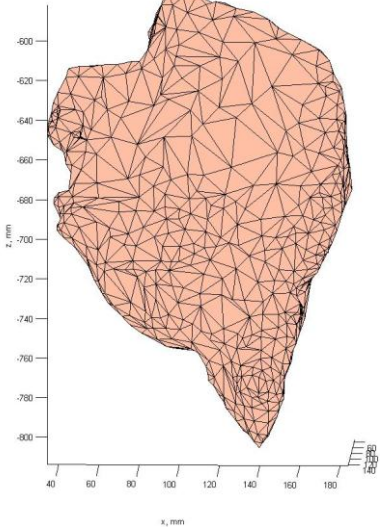
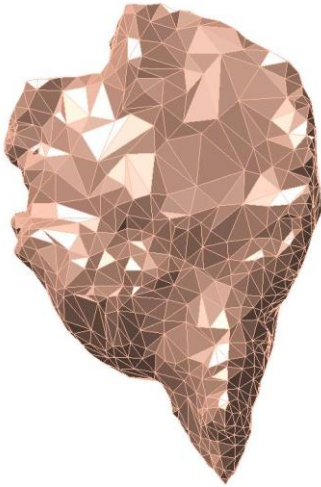
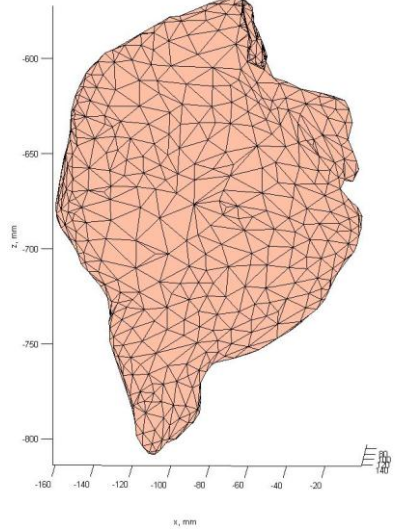
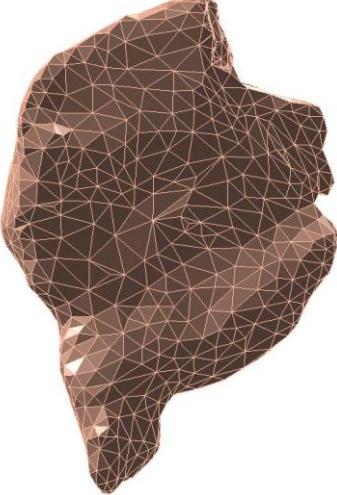
Calf left	 <p>A 3D wireframe plot of the left calf. The vertical z-axis ranges from -1050 to -1350 mm. The horizontal x-axis ranges from 100 to 20 mm. The depth y-axis ranges from 50 to 100 mm. The model is a triangular mesh colored in a light orange hue.</p>	 <p>A solid 3D model of the left calf, rendered as a smooth, light orange surface. It shows the overall shape and contours of the calf's body.</p>
Calf right	 <p>A 3D wireframe plot of the right calf. The vertical z-axis ranges from -1050 to -1400 mm. The horizontal x-axis ranges from 140 to -100 mm. The depth y-axis ranges from 60 to 120 mm. The model is a triangular mesh colored in a light orange hue.</p>	 <p>A solid 3D model of the right calf, rendered as a smooth, light orange surface. It shows the overall shape and contours of the calf's body.</p>
Cerebellum	 <p>A 3D wireframe plot of the cerebellum. The vertical z-axis ranges from 0 to 45 mm. The horizontal x-axis ranges from 60 to -40 mm. The depth y-axis ranges from 0 to 80 mm. The model is a triangular mesh colored in a light orange hue.</p>	 <p>A solid 3D model of the cerebellum, rendered as a smooth, light orange surface. It shows the complex, folded structure of the cerebellum.</p>

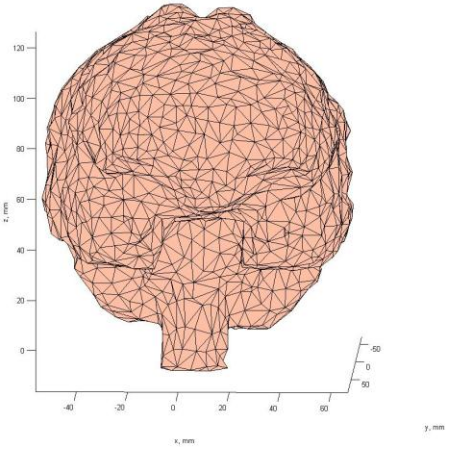
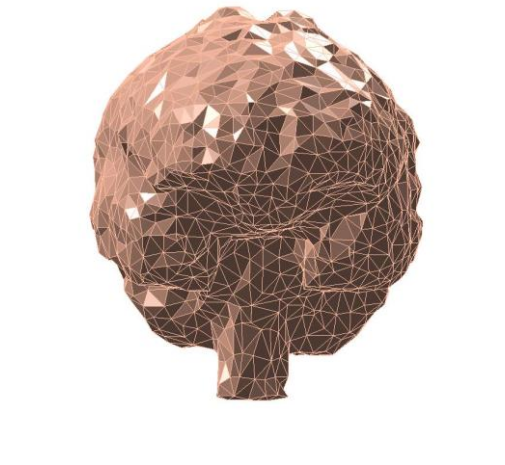
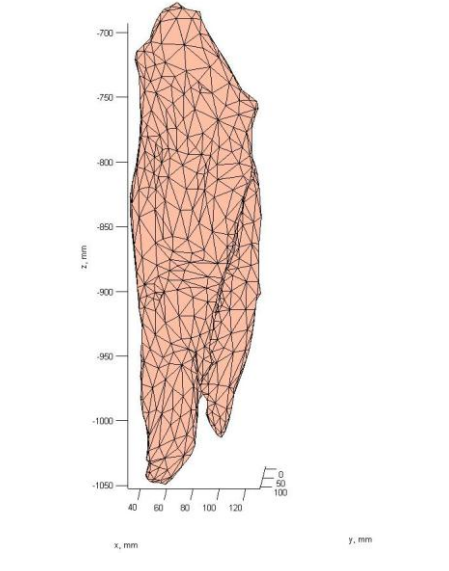
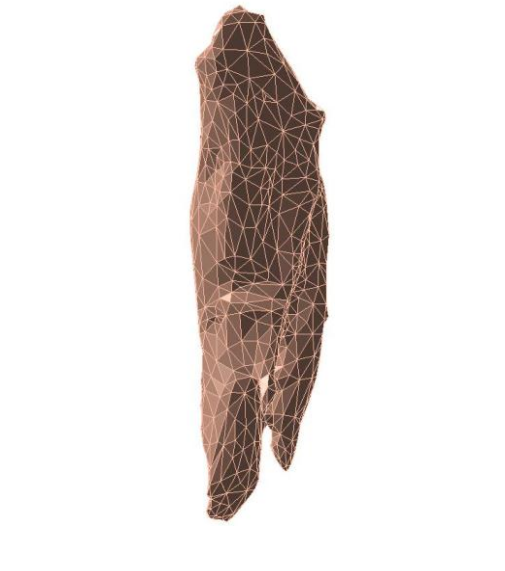
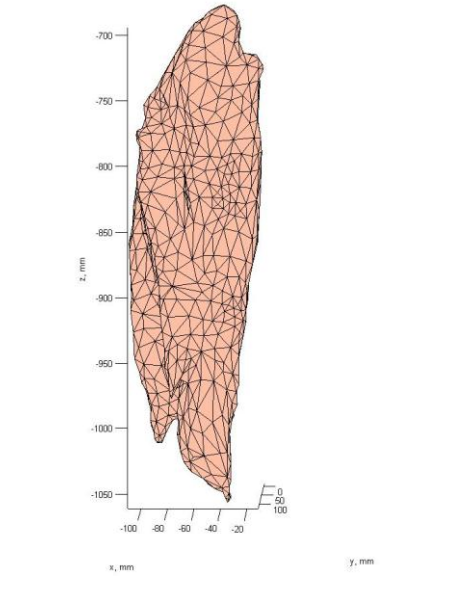
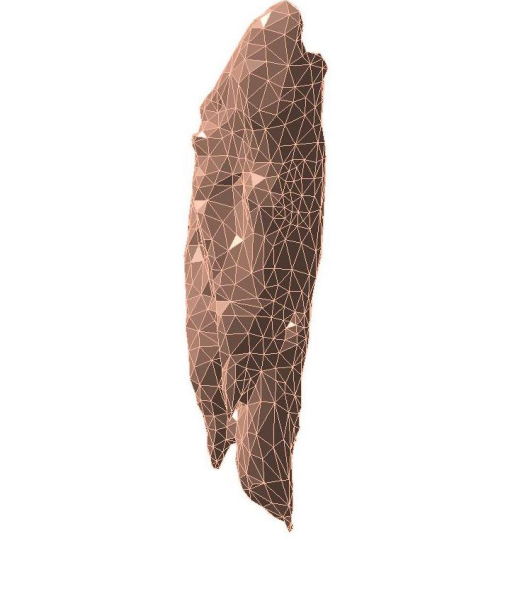




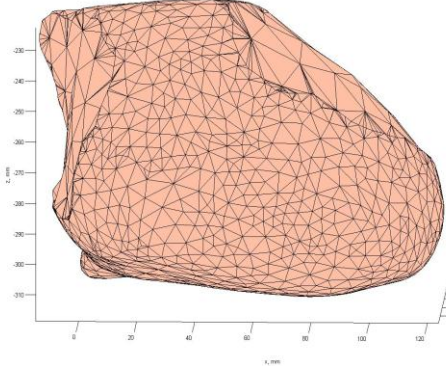
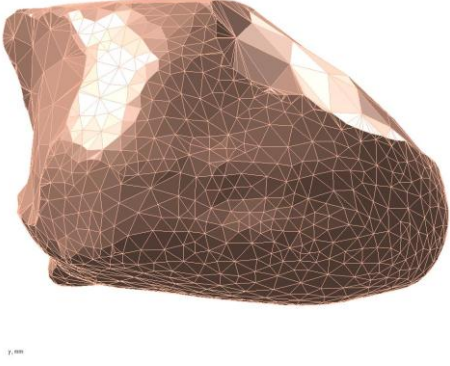
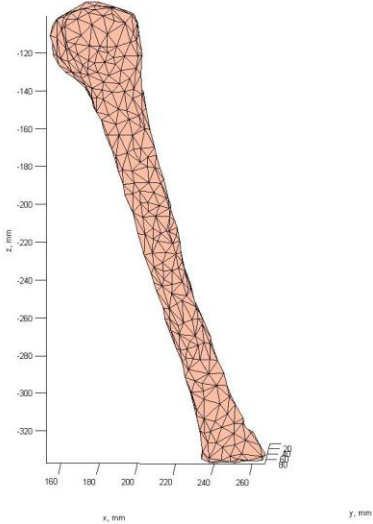

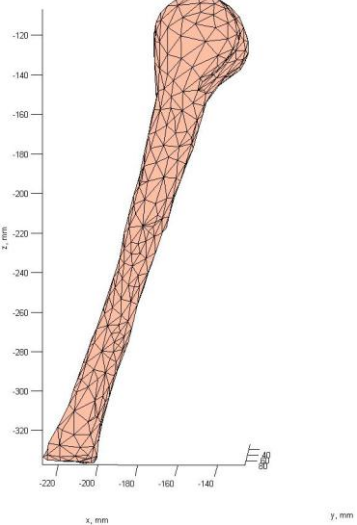

Eye left	 <p>A wireframe sphere rendered in a light orange color. It is positioned within a 3D coordinate system with visible axes. The vertical axis is labeled from 0 to 100 in increments of 20. The horizontal axis is labeled from -100 to 100 in increments of 20. The depth axis is labeled from 0 to 200 in increments of 20. The sphere's surface is composed of a triangular mesh.</p>	 <p>A shaded sphere rendered in a dark brown color with a triangular mesh. It is shown from a perspective view, highlighting its three-dimensional form.</p>
Eye right	 <p>A wireframe sphere rendered in a light orange color, identical to the one in the 'Eye left' row. It is positioned within a 3D coordinate system with visible axes. The vertical axis is labeled from 0 to 100 in increments of 20. The horizontal axis is labeled from -100 to 100 in increments of 20. The depth axis is labeled from 0 to 200 in increments of 20. The sphere's surface is composed of a triangular mesh.</p>	 <p>A shaded sphere rendered in a dark brown color with a triangular mesh, identical to the one in the 'Eye left' row. It is shown from a perspective view, highlighting its three-dimensional form.</p>
Fat	 <p>A wireframe model of a human figure, rendered in a dark brown color. The figure is shown in a side profile view, standing upright. It is positioned within a 3D coordinate system with visible axes. The vertical axis is labeled from 0 to -1500 in increments of 500. The horizontal axis is labeled from 100 to -200 in increments of 100. The depth axis is labeled from 0 to 200 in increments of 100. The figure's surface is composed of a triangular mesh.</p>	 <p>A shaded model of a human figure, rendered in a dark brown color with a triangular mesh. The figure is shown in a side profile view, standing upright. It is positioned within a 3D coordinate system with visible axes. The vertical axis is labeled from 0 to -1500 in increments of 500. The horizontal axis is labeled from 100 to -200 in increments of 100. The depth axis is labeled from 0 to 200 in increments of 100. The figure's surface is composed of a triangular mesh.</p>

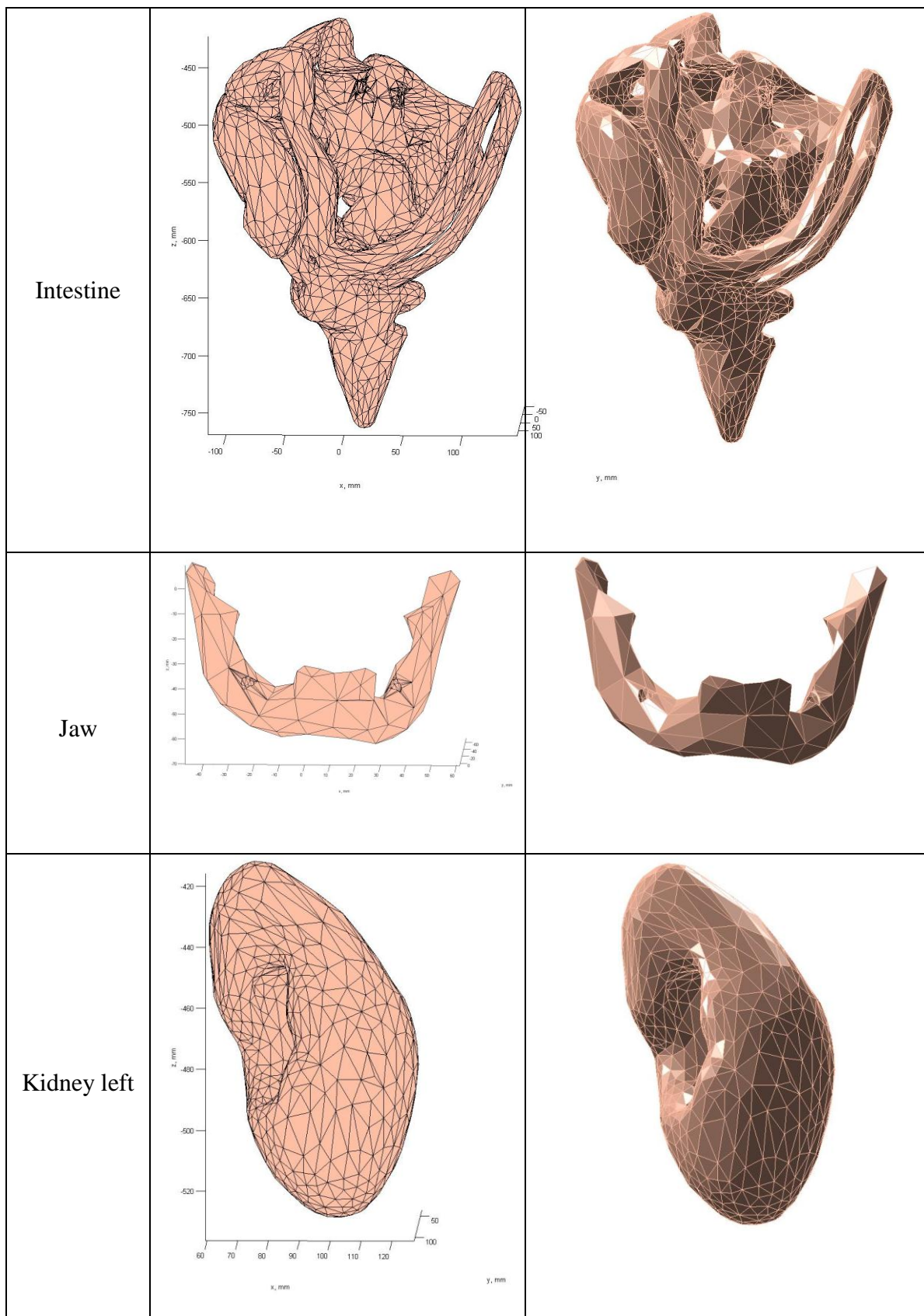
Femur left		
Femur right		
Fibula left		

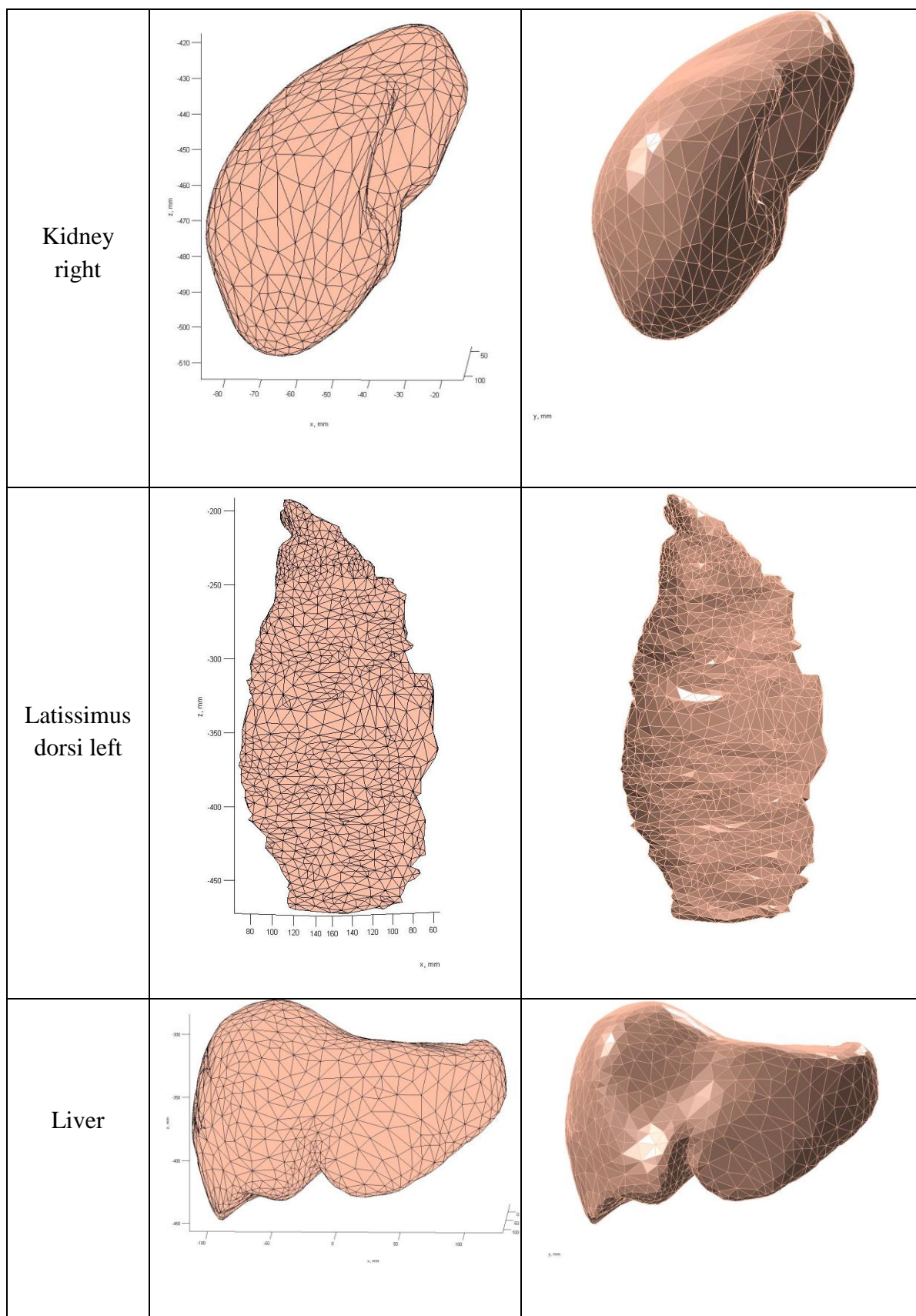
Fibula right		
Gluteus left		
Gluteus right		

<p>Grey Matter</p>	 <p>A 3D wireframe plot of a brain-like structure. The x-axis ranges from -40 to 60 mm, the y-axis from -50 to 90 mm, and the z-axis from 0 to 120 mm. The structure is composed of a dense network of orange lines forming a mesh.</p>	 <p>A 3D shaded surface plot of the same structure as the wireframe. It is rendered with a brownish-orange color and a semi-transparent mesh overlay, showing the top and side profiles of the brain-like shape.</p>
<p>Hamstring left</p>	 <p>A 3D wireframe plot of a hamstring-like structure. The x-axis ranges from 40 to 120 mm, the y-axis from 0 to 100 mm, and the z-axis from -700 to -1050 mm. The structure is composed of a dense network of orange lines forming a mesh.</p>	 <p>A 3D shaded surface plot of the same structure as the wireframe. It is rendered with a brownish-orange color and a semi-transparent mesh overlay, showing the side profile of the hamstring-like shape.</p>
<p>Hamstring right</p>	 <p>A 3D wireframe plot of a hamstring-like structure. The x-axis ranges from -100 to -20 mm, the y-axis from 0 to 100 mm, and the z-axis from -700 to -1050 mm. The structure is composed of a dense network of orange lines forming a mesh.</p>	 <p>A 3D shaded surface plot of the same structure as the wireframe. It is rendered with a brownish-orange color and a semi-transparent mesh overlay, showing the side profile of the hamstring-like shape.</p>

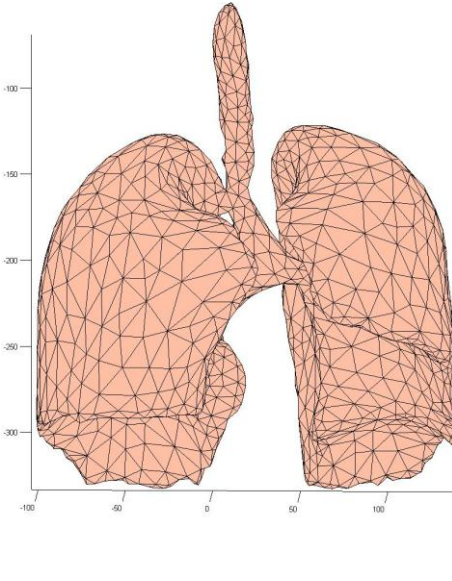
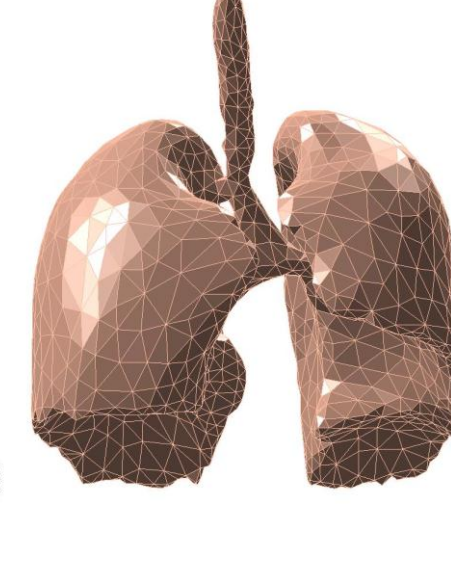
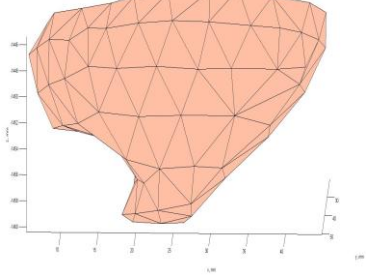
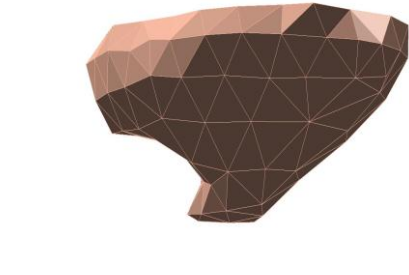
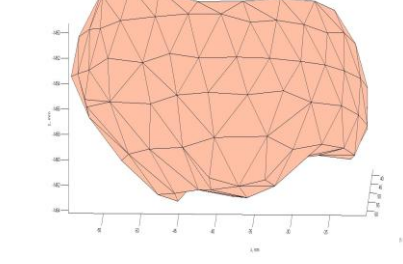
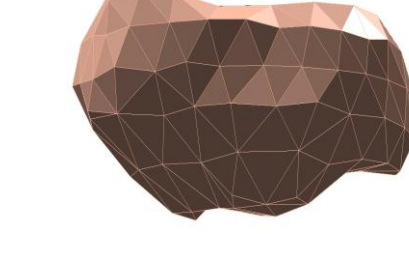
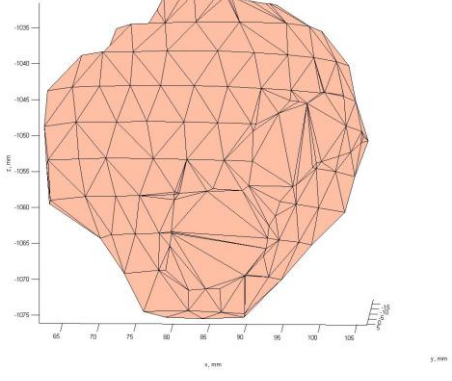
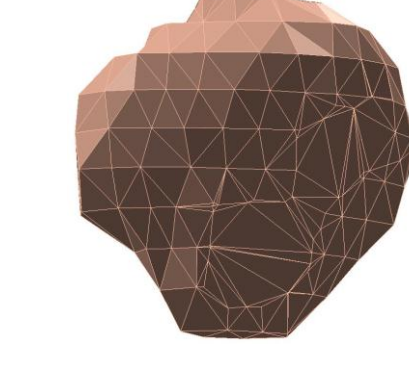


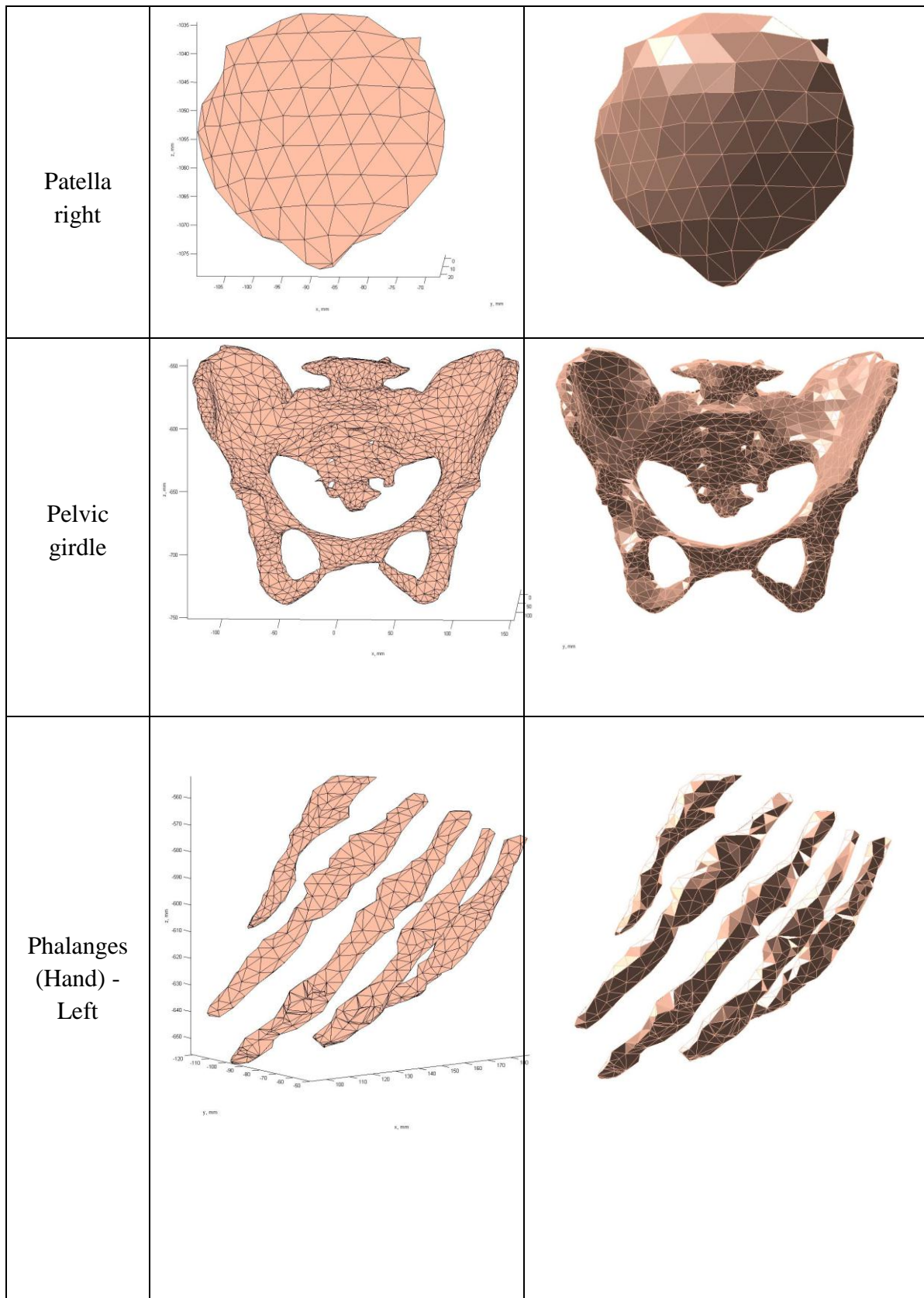
Heart		
Humerus left		
Humerus right		

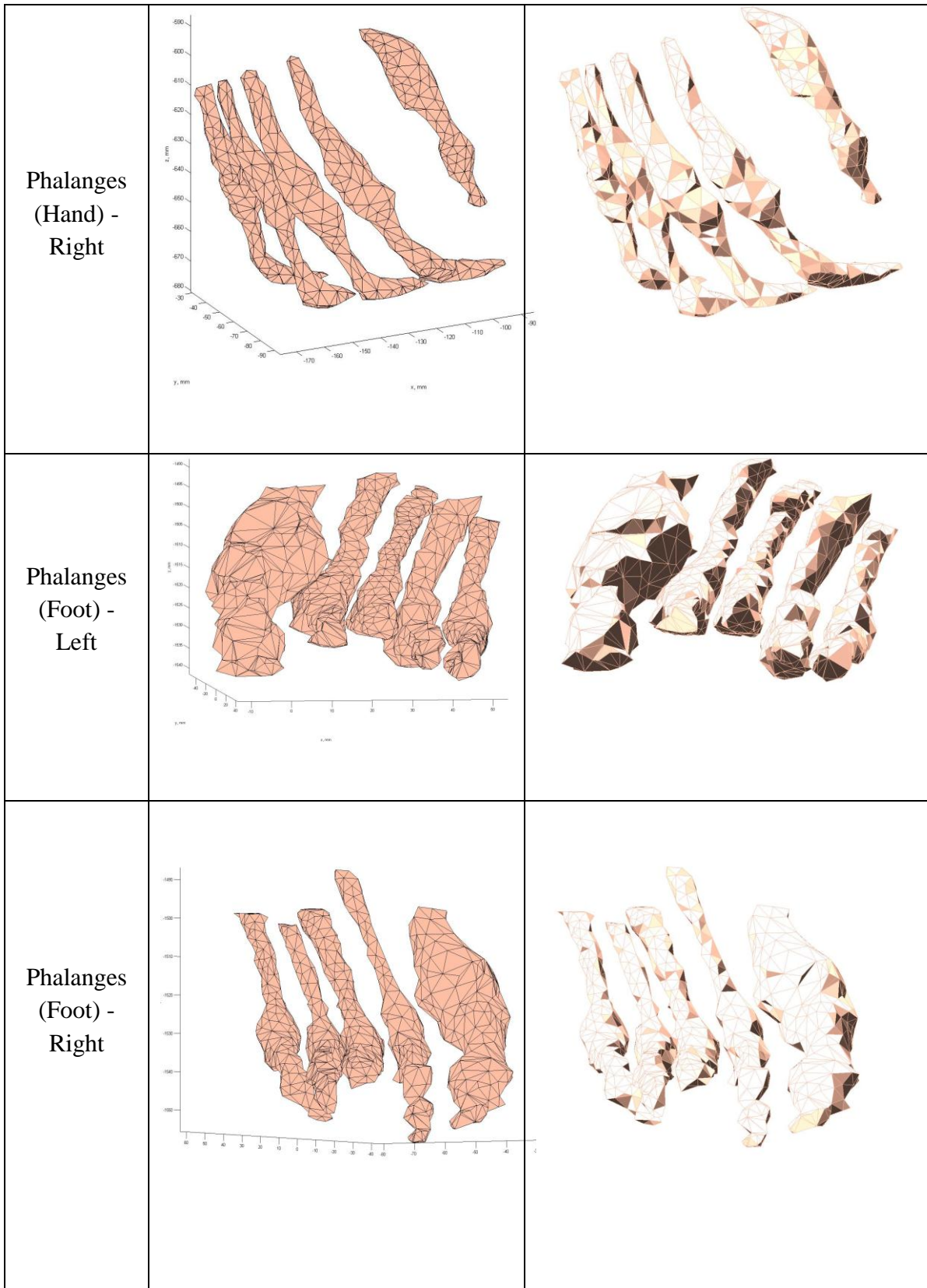




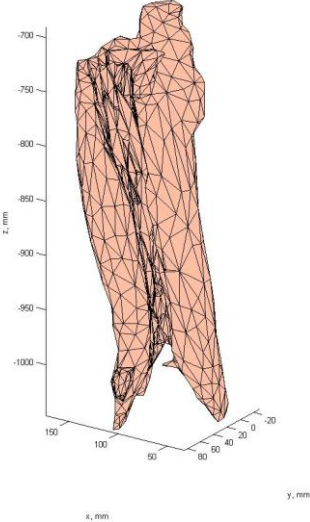
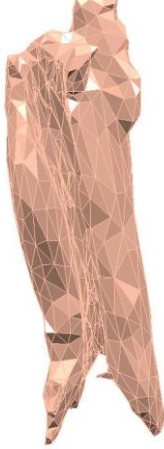
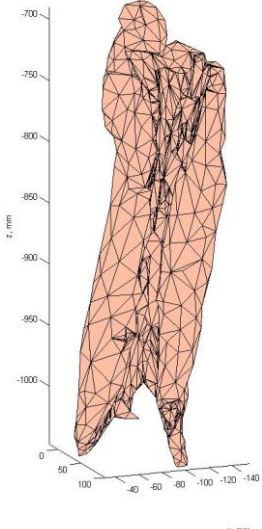

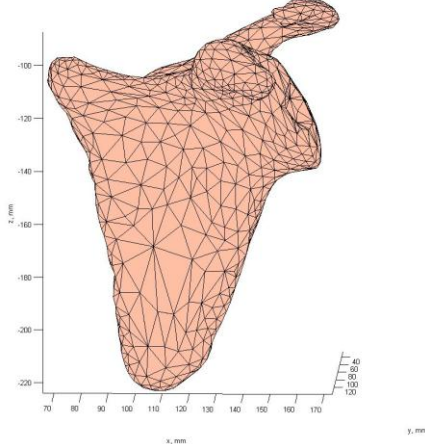
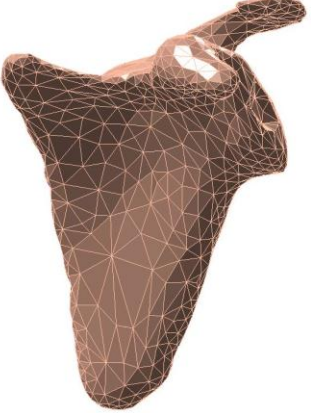


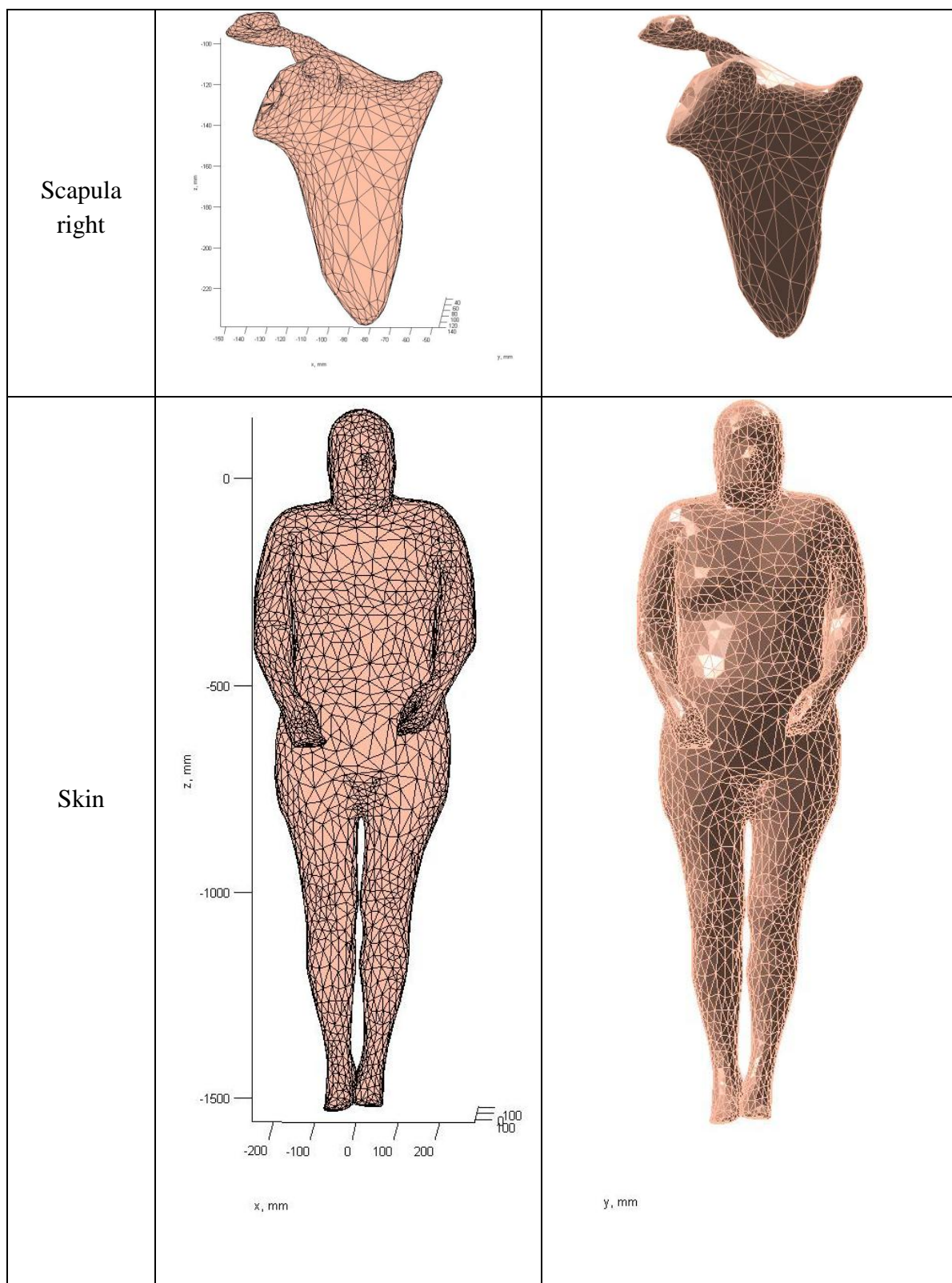
Lungs		
Navicular left		
Navicular right		
Patella left		



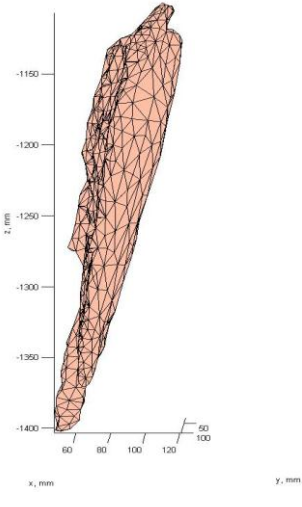

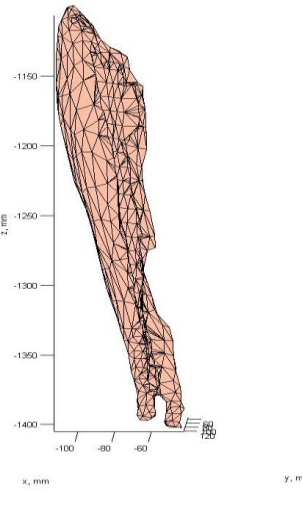

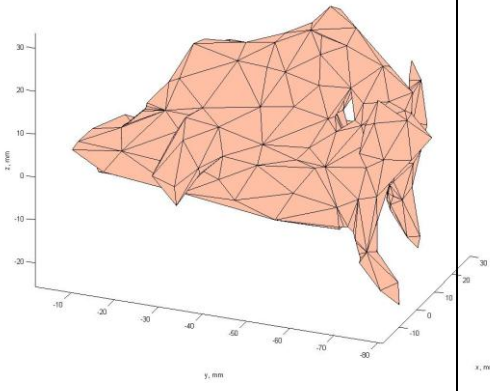
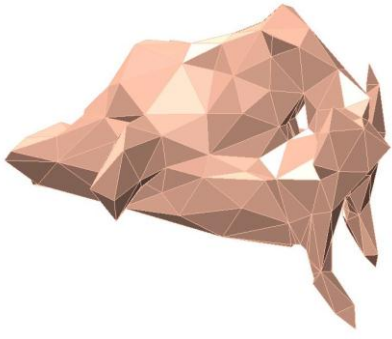


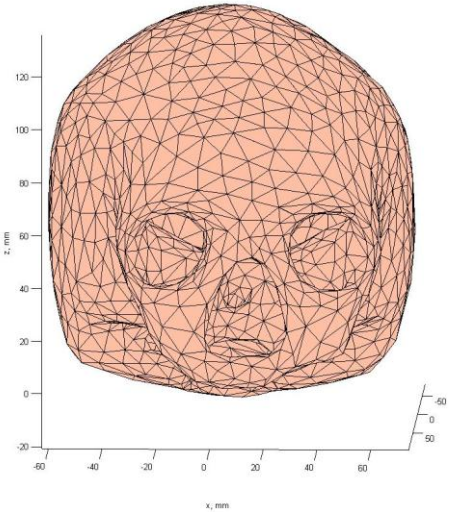
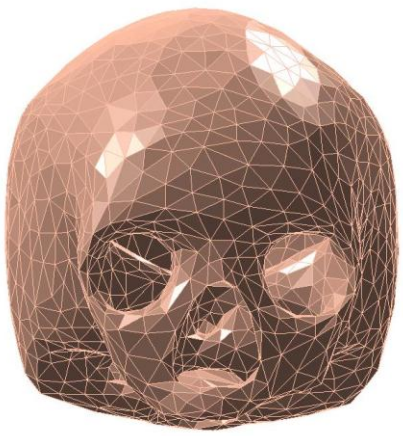
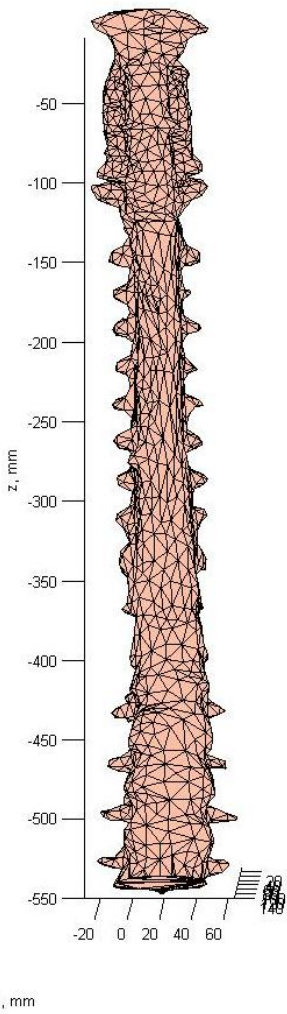
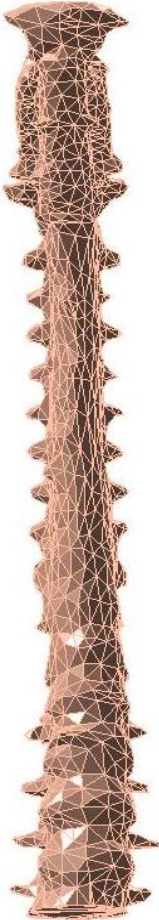


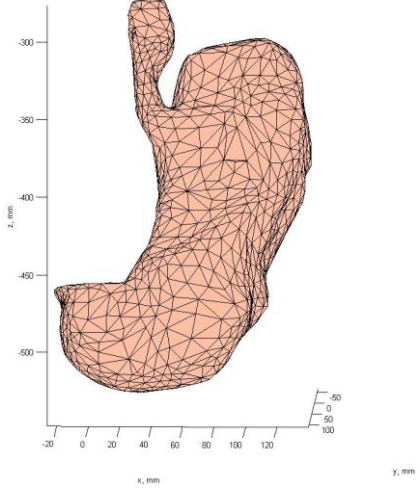
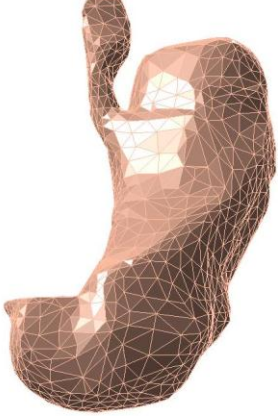
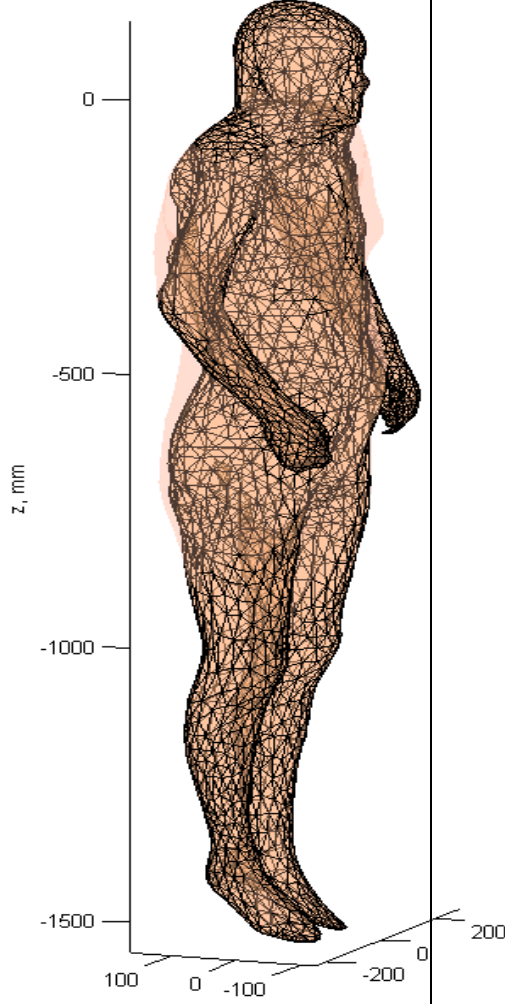

<p>Quadriceps left</p>		
<p>Quadriceps right</p>		
<p>Scapula left</p>		

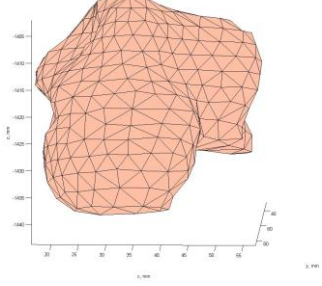
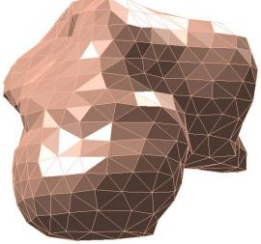
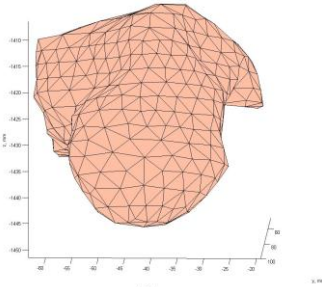
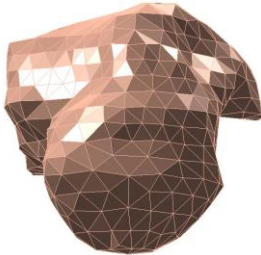
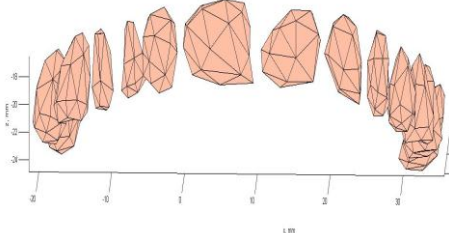
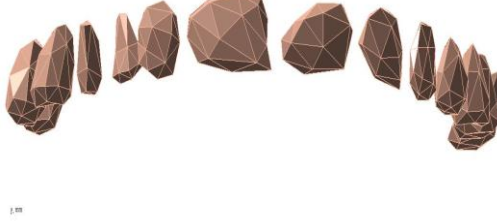
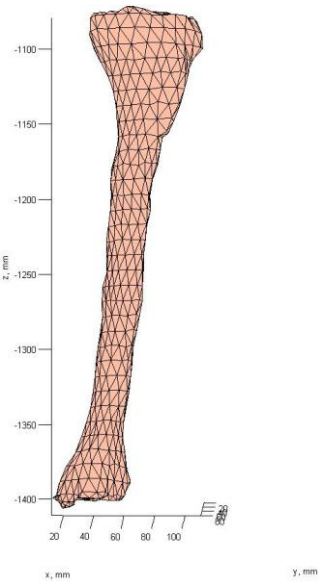





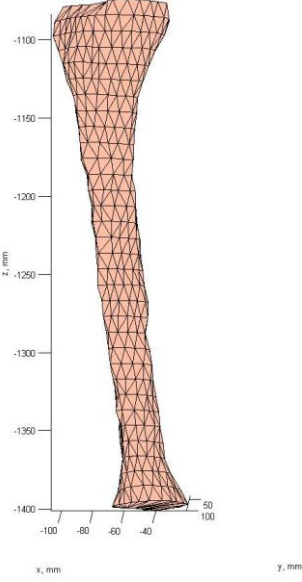

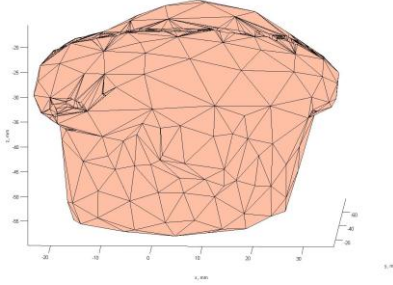
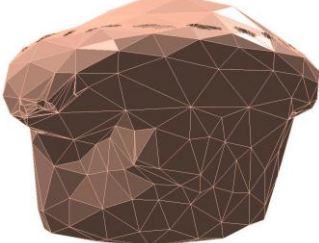
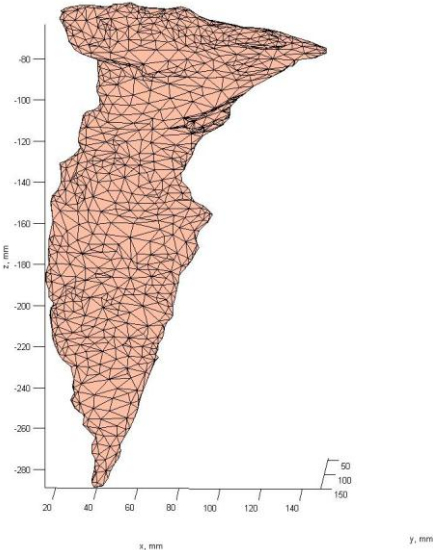

<p>Shin left</p>	 <p>A 3D wireframe plot of the left shin. The vertical z-axis ranges from -1400 to -1150 mm. The horizontal x-axis ranges from 60 to 120 mm, and the y-axis ranges from 60 to 100 mm. The model is a brown wireframe mesh.</p>	 <p>A solid 3D model of the left shin, rendered as a brown mesh.</p>
<p>Shin right</p>	 <p>A 3D wireframe plot of the right shin. The vertical z-axis ranges from -1400 to -1150 mm. The horizontal x-axis ranges from -100 to -60 mm, and the y-axis ranges from 60 to 100 mm. The model is a brown wireframe mesh.</p>	 <p>A solid 3D model of the right shin, rendered as a brown mesh.</p>
<p>Sinuses</p>	 <p>A 3D wireframe plot of the sinuses. The vertical z-axis ranges from -20 to 30 mm. The horizontal x-axis ranges from -10 to 10 mm, and the y-axis ranges from -40 to 0 mm. The model is a brown wireframe mesh.</p>	 <p>A solid 3D model of the sinuses, rendered as a brown mesh.</p>

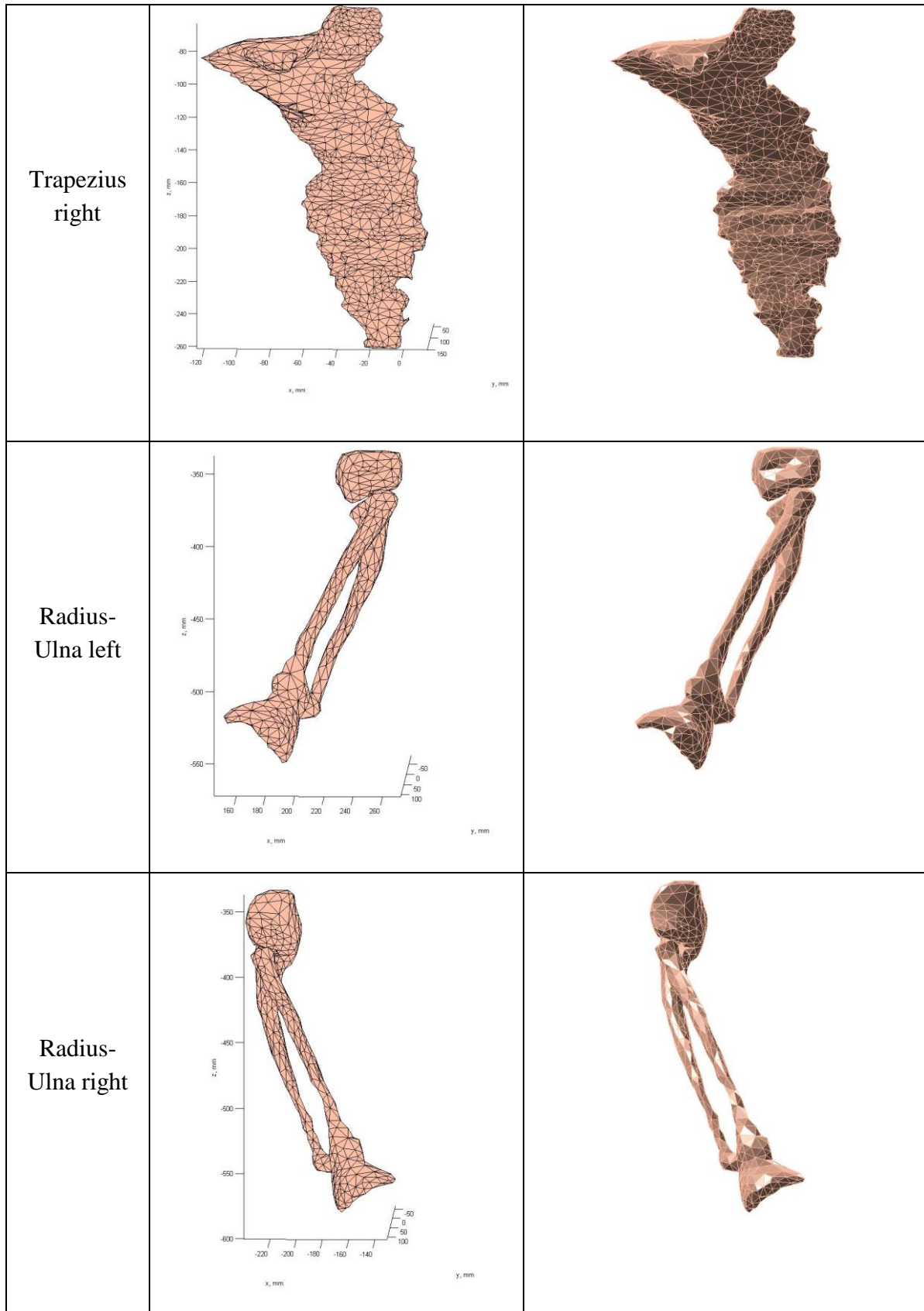
<p>Skull</p>		
<p>Spine</p>		

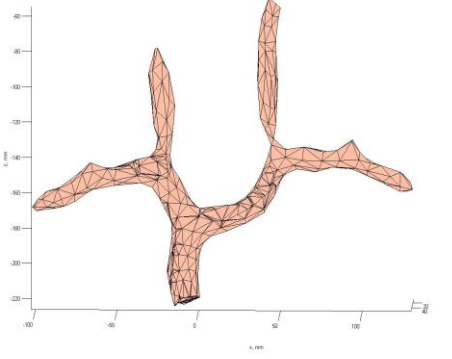
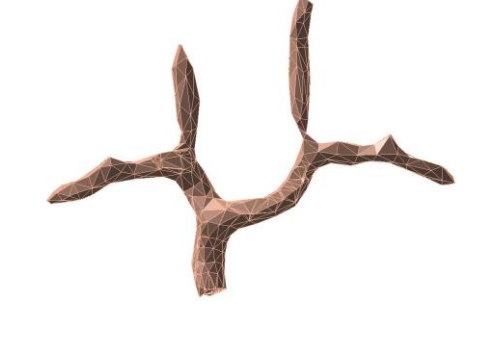
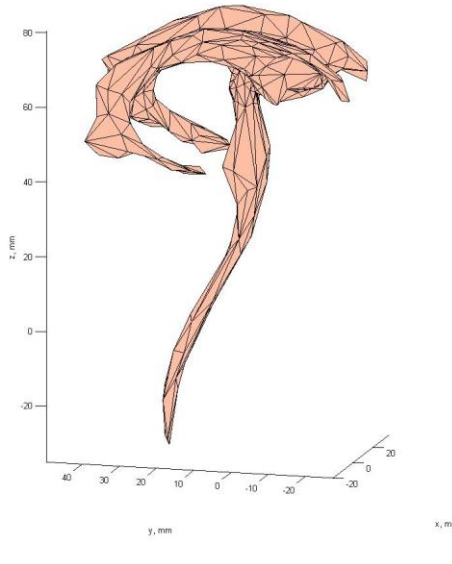

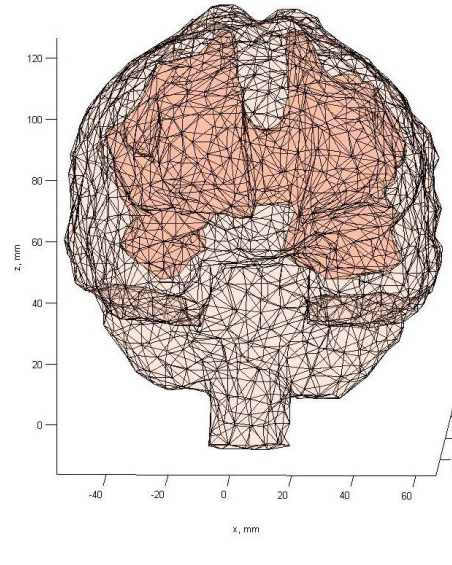

<p>Stomach</p>		
<p>Subcutaneous fat</p>		

Talus left		
Talus right		
Teeth upper row		
Tibia left		



Tibia right		
Tongue		
Trapezius left		



<p>Vena cava superior</p>		
<p>Ventricles</p>		
<p>White Matter</p>		

#### ***4.3. Deformable model for different Body Mass Index (BMI)***

The current VHP – Female body has its arms and legs in fixed position and it typically represents a female aged around 59 – 60 years. This computational model could be potentially used for a wide range of studies if it was BMI dependent. Various studies are being conducted to understand the relation between the fat, muscle and organ size for respective BMI values [11], [4]. Also modeling the organ movements such as heart beating, breathing, blood and CSF flow would be required to use the computational model in various domains [13]. Efforts for developing techniques to deform the existing model to individualized patient specific models have been also around [14]. Deformable model would allow the model to be morphed into having various postures and movable limbs which would be useful for specific simulations, for example, person doing a phone for radiation studies etc.

#### ***4.4. VHP – Female Model in its current form***

The complete VHP – Female model has now been successfully assembled and can be used for simulation studies. The assembly of the human body is done in MATLAB and as a validation step, all meshes have passed the ANSYS High Frequency Structural Simulator (HFSS) mesh check at the strictest setting and Fig. 4.1 shows the present version of the VHP-Female model with over 80 parts. This model has been used for numerous applications over the time frame of development. Chapter 5 details Transcranial Direct Current Stimulation, which is targeted stimulation of primary cortex. Comparison of montages was studied to achieve deeper simulation. Other studies where the model was used are mentioned and potential applications are discussed.



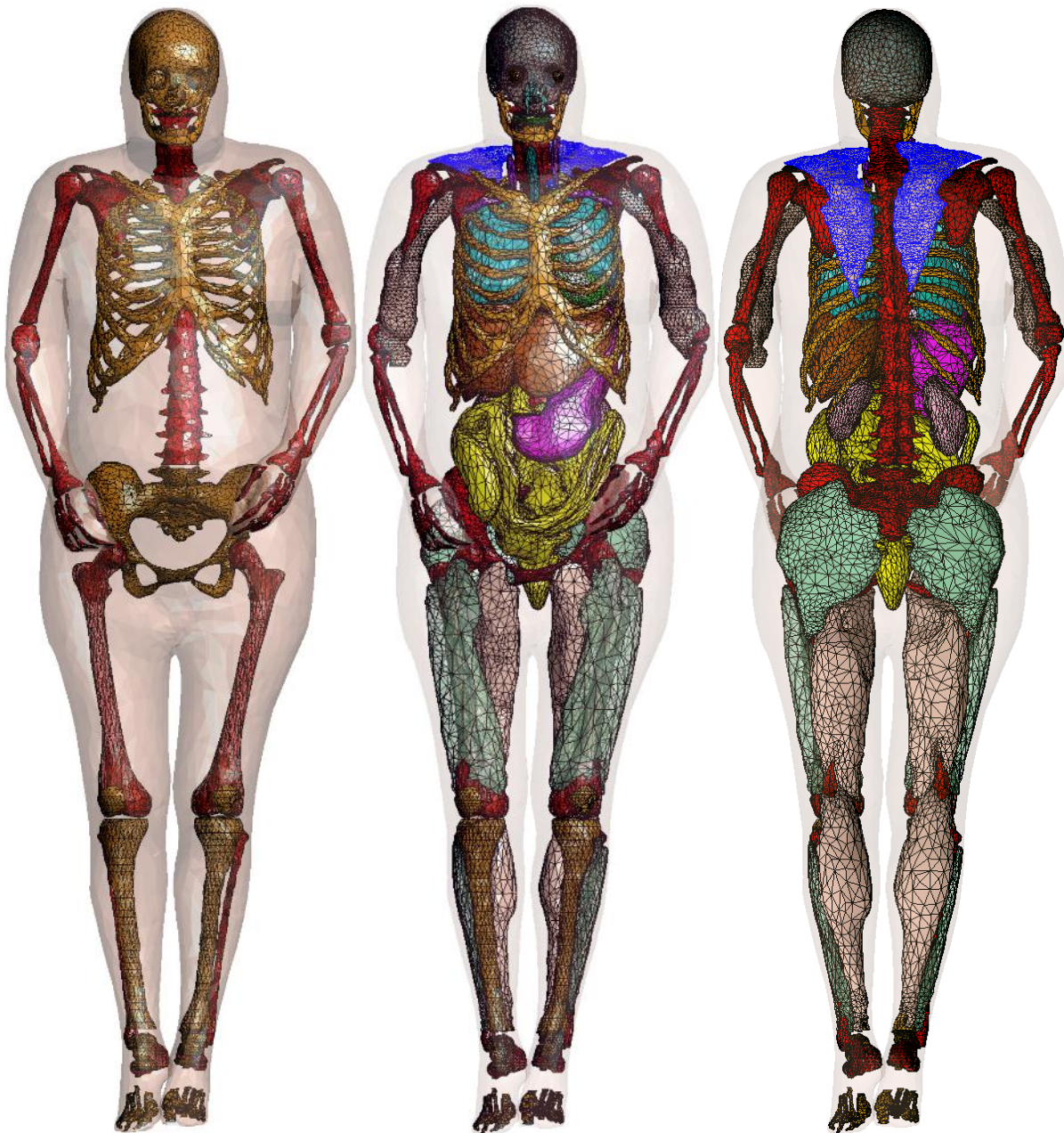


Fig.4.1 VHP-Female model to date: a) – skeleton bones, b) – anterior view of organs and muscles, c) – posterior view of organs and muscles.

## **References**

- [11] Ding A., Mille M. M., Liu T., Caracappa P. F., and Xu X. G., “Extension of RPI-adult male and female computational phantoms to obese patients and a Monte Carlo study of the effect on CT imaging dose,” *Phys. Med. Biol.* 57(9), 2441–2459 (2012).10.1088/0031-9155/57/9/2819.
- [12] Whole-Body Human Database of Japanese Average Adult Males, Females and Pregnant Woman. Online: <http://www.nict.go.jp/> ; see also [http://www.nict.go.jp/en/pdf/NICT\\_NEWS\\_1003\\_E.pdf](http://www.nict.go.jp/en/pdf/NICT_NEWS_1003_E.pdf)
- [13] J. Zhang, X. G. Xu, C. Shi, and M. Fuss, “Development of a geometry-based respiratory motion-simulating patient model for radiation treatment dosimetry,” *J. Appl. Clin. Med. Phys.*, vol. 9, pp. 16–28, 2008.
- [14] Ligo L, Diallo I, Shamsaldin A, Chavaudra J, Bonaiti-Pellie C, de Vathaire F., “Individualized phantom based on CT slices and auxological data (ICTA) for dose estimations following radiotherapy for skin haemangiomas in childhood,” *Radiother Oncol* 1998; 49:279–85.

## Chapter 05 –

# Application example - Transcranial Direct Current Stimulation

### Introduction

Transcranial Direct Current Stimulation (tDCS) has been used for the treatment of various neurological and psychiatric disorders, including depression, anxiety, and Parkinson's disease [1], [2]. Studies have shown that patients undergoing the procedure experience positive behavioral modifications with minimal negative effects that may include skin irritation, mild redness and itching under the electrode, headache, nausea, dizziness or a slight tingling sensation. Additionally, generation of toxins induced by an electrochemical reaction at the electrode-tissue interface are possible and application of tDCS above skull defects or inadequate electrode contact may produce focused current flow that has the potential to cause damage to skin and nerve tissue. Use of tDCS remains a very active area of research with the potential to non-invasively treat many of humanity's long standing disorders.

A number of electrode configurations, known as montages, are in use to control the application of current and concentrate the current density onto a particular area of the brain. These montages have been traditionally constructed based on knowledge of human anatomy and physiology. For example, if stimulation of the visual cortex is desired, an anode and cathode would be placed at the rear center and top center of the head, respectively. In this way, a particular area of the brain is identified for stimulation via tDCS and a montage that activates that area in a targeted manner is selected. One would assume that a large portion of the current leaving the anode would pass through the visual cortex while traveling to the cathode. In-vivo measurements have been reported [3] in the brain of a monkey and were used as the basis of constructing a model of the head that may be used to predict current flow in the brain from surface electrodes. However, real-time measurements and evaluation of individual anatomy remain challenges. To this end, extensive application of modeling and simulation techniques, including the Finite Element Method (FEM) have been used to characterize and understand the impacts of electrode arrangements on the human form, along with other factors including electrode size, the number of anode and cathode locations and current density [4-8]. The FEM has become such an important tool in the realm of tDCS that proposed general and customized, patient specific, and experimental tDCS protocols are examined and optimized using computational tools [9]. The models themselves have even acquired specific terminology and are known as 'forward models' with particular procedures on construction and usage [10]. Clearly, the level of effort demonstrated in model construction and the prevalence of research based on modeling and simulation techniques indicates that conscientious use of FEM and other numerical method based solvers coupled together with anatomically accurate and predictive forward models [11] represents a realistic and efficient means that provides scientists, engineers and medical personnel detailed information on the performance of tDCS hardware in the very complex and multi-variant human body environment. Studies that take into account the effects of anisotropic conductivity in human tissues, including the skull and white matter, have

demonstrated the importance of considering this physical condition when using forward models [12-13].

Despite existing studies and techniques that seek to manipulate the locality and depth of the stimulated area [14-17], open questions remain on the role of the cathode in terms of placement on the body. Field localization is strongly desired to provide tDCS practitioners the ability to treat certain disorders through precise targeting of specific areas or structures of the brain. Extracranial locations (e.g., neck) of the cathode have been examined [18], along with the efficacy of a fronto-extracranial montage in treatment of depression [19]. The impact of extracranial montages on the brain stem and associated organs and tissues remains a concern [20], though the influence of these montages on cardio-vascular and autonomous functionality has been discussed in [21].

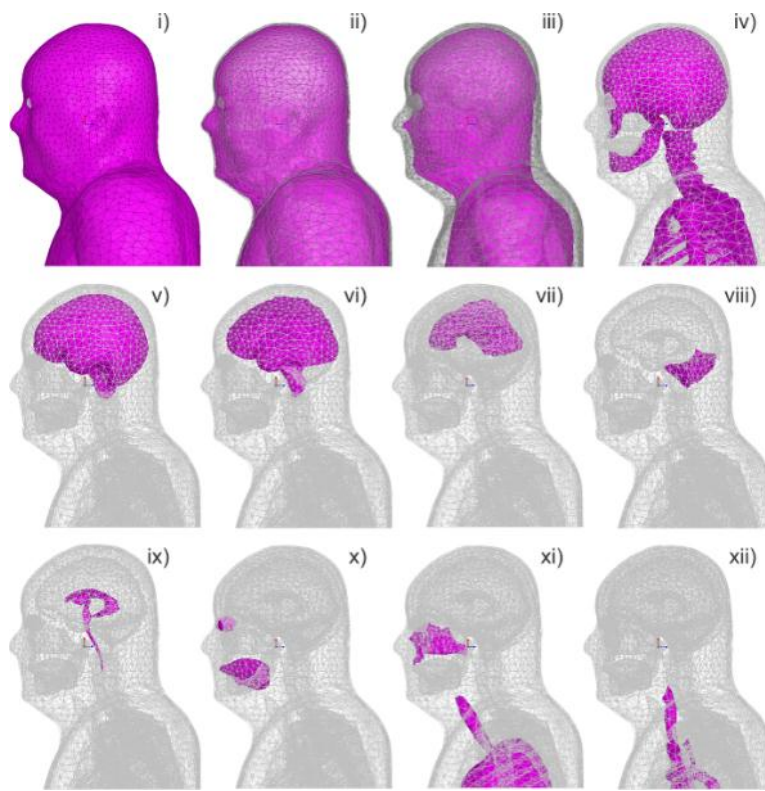


Fig. 5.1. Estimate for separate and distinct components of computational model employed for all tDCS simulations, each with individual material properties, including: i) – Artificial skin shell (2 mm thick); ii) – fat layer shell; iii) – muscle volume; iv) bones (left and right acromion, left and right humerus, jaw, ribs, left and right scapula, skull, spine), v) – closed CSF shell; vi) – cerebral cortex (grey matter); vii) – white matter; viii) – cerebellum; ix) – CSF ventricles; x) – eyes and tongue (separate tissues); xi) – sinus cavity, lungs and trachea; xii) – aorta and cava

The focus of this work is the simulation of the volumetric current density in the brain with electrodes configured in a cephalic (C3-Fp2) versus extracranial manner with evaluations of cathode placement on both ipsi- and contralateral shoulder locations.



The FEM phantom used for this purpose is shown in Fig. 5.1. The anatomical brain segmentation included grey matter, white matter, ventricles, and cerebellum – see Fig. 5.1. The numerical simulation setup is described in Section 5.1. Electrode constitution and assembly is reported in Section 5.2.

The cerebral cortex has been numerically defined as the Boolean difference between the grey matter and the white matter meshes. The cerebral cortex has further been artificially subdivided into individual lobes and cortexes as shown in Fig. 5.2.

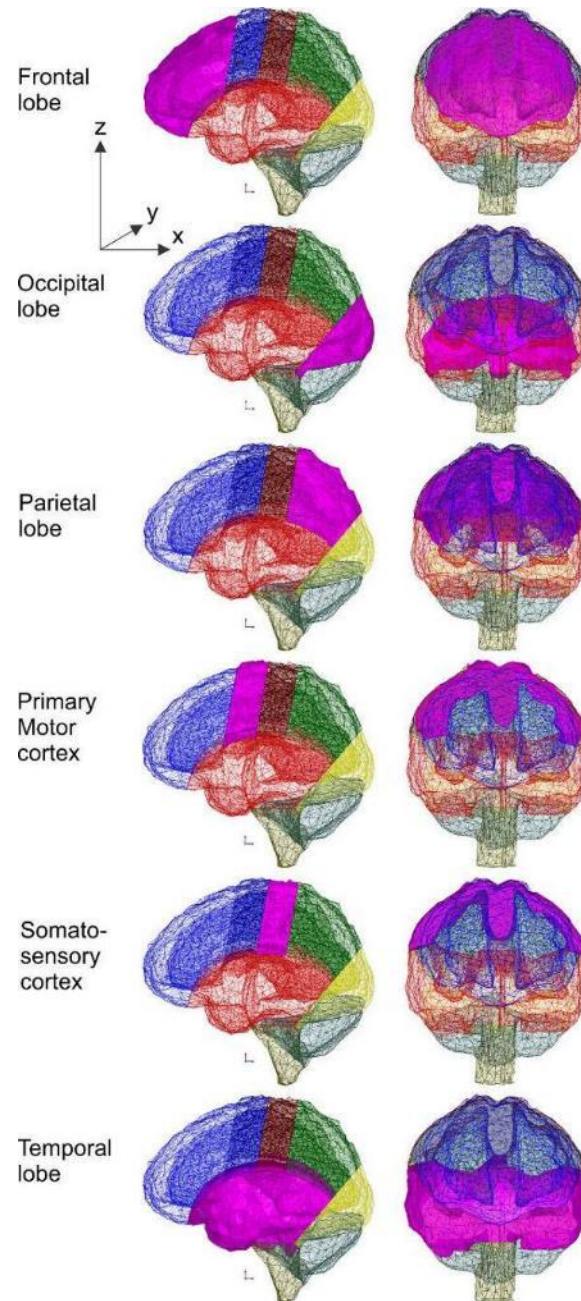


Fig. 5.2. Separation of the cerebral cortex into computational sub regions including the frontal lobe, the occipital lobe, the parietal lobe, the primary motor cortex, the somatosensory cortex, and the temporal lobe.

Section 5.3 provides qualitative and quantitative results for the *local current density magnitude* within the brain volume. We visualize the total current density by plotting current on the surfaces of both the cerebral cortex and white matter. Alternatively, we visualize the total current density using a series of cut planes, each of which is accompanied by the corresponding cut plane atlas. Section 5.3 also discusses the invariance of the *relative* current density magnitudes to significant changes in skin properties. We considered two extreme cases of wet and dry skin, respectively. Along with its primary goal, this study indirectly addresses the effect of changes in the contact between electrode and skin throughout the course of an extended tDCS treatment.

Section 5.4 reports quantitative results for both the *average vertical current density magnitude* and the *average horizontal current density magnitude* in every individual lobe and/or cortex shown in Fig. 5.2 along with the global coordinate system employed. The corresponding current densities are defined by

$$\begin{aligned} J_z^{avg} &= \frac{1}{V} \int_V |J_z(\mathbf{r})| d\mathbf{r}, \\ J_{xy}^{avg} &= \frac{1}{V} \int_V \sqrt{J_x^2(\mathbf{r}) + J_y^2(\mathbf{r})} d\mathbf{r} \end{aligned} \tag{5.1}$$

where  $V$  is the volume of the tissue under study and  $\mathbf{J}(\mathbf{r})$  is the spatial vector current density in this volume.

Section 5.5 estimates the expected electrode voltages and quantifies voltage responses due changes in properties of individual anatomical tissues.

Section 5.6 also compares the results of the present paper with the previous numerical simulations.

Finally, Section 5.7 concludes the chapter.

## **5.1. Simulation setup**

### **5.1.1. Material properties**

Electromagnetic modeling of the human body requires meticulous and cautious definition of the associated material properties resident within the simulation. A wealth of research on the subject is available [22]-[27] demonstrating the variability of values across multiple types of tissues and a high dependence on frequency. For low frequency and static simulations such as the ones described in this work, material conductivity is paramount. A summary of tissue types and conductivity values is given in Table 5.1 [27].

### **5.1.2. FEM Software and Numerical Accuracy**

Static electromagnetic simulations were conducted using ANSYS' Maxwell 3D version 16 product. This software numerically obtains a unique solution to Maxwell's equations at DC via the FEM and user specified boundary conditions. The Maxwell product has extensive mesh analysis and healing capabilities. Most important, solution convergence and the ultimate accuracy is controlled through a rigorous adaptive mesh refinement procedure.

Table 5.1. Electrical properties employed during Stimulation

Structure	FEM Material	Conductivity (S/m)
Sinus	Air	0
Aorta Superior Vena Cava	Blood	0.7
Humerus Jaw Ribs Scapula Skull Spine	Homogenous Bone (a combination of cancellous/cortical types)	0.0756/0.02
Gray Matter	Gray Matter (Brain)	0.0275
White Matter	White Matter (Brain)	0.0277
Cerebellum	Cerebellum	0.0475
Cerebrospinal Fluid (CSF)	CSF	2
Eye	Vitreous Humor	1.5
Fat layer	Fat	0.0377
Lung Trachea	Inflated Lungs	0.0389
Muscle Layer	Muscle	0.202
Skin Layer	Dry Skin	0.0002
Tongue	Tongue	0.8

For the results presented below, five iterations of adaptive mesh refinement were employed, each with a refinement level of 30% per pass. This process grew the total number of tetrahedral elements from approximately 200,000 to over 600,000 with total runtimes on the order of about six hours on a server with 192 Gbytes of RAM. When solving a DC current conduction problem, the Degrees of Freedom (DoF) are the electric scalar potentials at each node of the tetrahedral mesh. Typical values of mesh size per iteration and energy loss are given in Table 5.2 and demonstrate a reduction of the residual error through successive refinement steps, increasing the accuracy of the calculation as it converges.

Table 5.2 Convergence of a typical case based on Tetrahedral mesh size

Adaptive Pass	Number of Tetrahedra	Total Loss (mW)	Loss Error (%)	Delta Loss (%)
1	183,113	0.6	1.10	N/A
2	248,020	0.607	0.33	1.17
3	335,946	0.60915	0.19	0.35
4	455,431	0.61047	0.13	0.22
5	616,856	0.61137	0.09	0.15

### ***5.1.3. Boundary Conditions and Excitation***

The default boundary conditions used by ANSYS MAXWELL 3D during DC conduction type simulations are as follows. Standard (or “natural”) boundaries are enforced at inner object interfaces and ensure the continuity of the normal component of the direct electric current density through the interfaces. Homogeneous Neumann boundaries imposed on all outer boundaries do not allow the normal electric current to pass. The electric field within the conductor is indeed tangential on this outer boundary. We have found that MAXWELL 3D does not implement an ideal hypothetical current source with a fixed current density and a variable voltage across the electrode surface. Instead, a more realistic voltage source model with Dirichlet boundary conditions of a fixed surface electrode voltage is internally used for both voltage and current excitations. Appendix B details the boundary conditions for DC conduction in detail. After completing the simulations, the required total current may be related to voltage. A user can define the total current a priori, which is the current source implementation.

## ***5.2. Electrodes and their Montages***

### ***5.2.1. Electrode Model***

Electrodes were simulated using rectangular blocks of material (sponges) with the conductivity of saline solution (2 S/m). Electrodes were sized consistent with existing procedures and protocols [1] such that the rectangular surface in conformal contact with the skin was 5 cm on a size with a total surface area of 25 cm<sup>2</sup>. Each electrode was constructed in a virtual environment by subtracting larger geometric blocks that intersected the surface of the VHP model with the skin of the model. In this way, the contacting surface of the electrode was made conformal such that, even in areas of high curvature on the model, full contact was maintained and no space existed between the electrode and the skin. A total electrode current of 2 mA (with the equivalent uniform density of 0.08mA/cm<sup>2</sup> [1]) was employed as the source in all cases described below.

### ***5.2.2. Electrode Montages***

Electrodes were arranged in three different configurations: following the Modified Combinatorial Nomenclature (MCN) of the International EEG 10-20 system, we simulate the C3-Fp2 montage, which has been traditionally used to stimulate the primary motor cortex (M1) by placing the stimulation electrode at the top-left portion of the head and the reference electrode at the contralateral supraorbital position; an extracephalic contralateral shoulder montage which retains the original excitation electrode position but shifts the reference electrode to the opposite side shoulder; and extracephalic ipsilateral shoulder montage which also retains the original excitation electrode position but shifts the reference electrode to the shoulder on the same side of the body as the excitation. Electrode positions and a cut plane atlas may be viewed in the upper 2 rows of Figs. 5.4-5.8. The cut plane atlases show that the layer of muscle around the head is essentially non-existent (see Figs. 5.4-5.6) and only contributes to the model at regions midway and below the skull – see Figs. 5.7 and 5.8. Skin and fat layers mostly contribute to conduction around the head.



### ***5.3. Simulation results for total current density***

#### ***5.3.1. Total current density for surfaces of Cerebral Cortex and White Matter***

The total current density magnitude is plotted on the surfaces of the cerebral cortex and white matter in rows 2 and 3 of Fig. 5.3, respectively. The traditional cephalic montage in column 1 demonstrates a significant amount of current at the anterior of the grey matter as it passes to the supraorbitally located cathode. The surface plots of the extracephalic configurations exhibit much lower current densities in this region of the brain with higher concentrations toward the posterior.

When stimulated with an extracephalic configuration, the current on the surface of the white matter appears to be slightly more concentrated directly below the anode, suggesting a relatively deeper penetration with less current passing through the anterior of the frontal lobe.

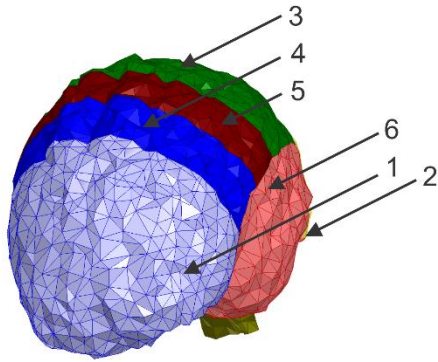
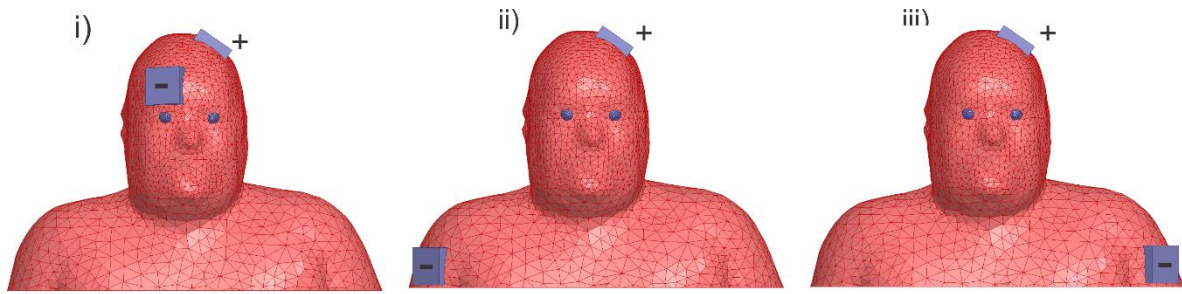
#### ***5.3.2. Total current density for sagittal cut planes***

A series of plots portraying the current densities experienced with each montage are presented in Figs. 5.4- 5.8 and all figures are displayed with the same scale for comparison purposes. Figs. 5.4- 5.6 (similar to Fig. 5.3) are divided into columns i – iii which depict current density results from the traditional, contralateral and ipsilateral shoulder montages projected onto a sequence of sagittal dissecting planes that progressively shift from the anode through the head and towards the right side of the model. In all cases, the shunting nature of the high conductivity CSF is quite apparent as high proportions of the total current are seen passing through this layer surrounding the brain. This characteristic is plainly seen on the third rows of Figs. 5.4-5.6, which provide images of the brain that include the surrounding structures. The high amount of current shown in the third row of Fig. 5.5 is due to the presence of the CSF ventricles at the center of the head.

A sagittal plane passing through the anode is depicted in Fig. 5.4. Relatively higher proportions of the current are observed in the primary motor cortex of the extracephalic cases. Additionally, the depth of stimulation appears relatively greater in both extracephalic configurations.

A second sagittal plane located at the approximate midpoint between the anode and the contralateral supraorbital cathode position is shown in Fig. 5.5. The current levels within the brain depicted in this plane provide evidence that the higher levels of current are present in the frontal lobe in the cephalic arrangement. Both extracephalic arrangements again indicate a slightly deeper level of stimulation. Current density values in Fig. 5.5 indicate that there is some minor stimulation of the brain stem when using extracephalic anode locations versus essentially no stimulation when using the traditional montage with the ipsilateral shoulder arrangement performing marginally better than the contralateral design. While current is present in the brain stem, the values are low and approximately 5 times less than current values in the area of desired stimulation.

A final sagittal plane passing through the contralateral supraorbital cathode position is presented in Fig. 5.6. Again, the cephalic configuration depicts a relatively larger percentage of the current passing through the prefrontal lobe as it moves toward the cathode.



### Cerebral cortex atlas

- 1 - Frontal lobe
- 2 - Occipital lobe (almost entirely masked at this view angle)
- 3 - Parietal lobe
- 4 - Primary motor cortex
- 5 - Somatosensory cortex
- 6 - Temporal lobe

J vs.  $J_{in}$  percentage

1.3	1.6	2.1	2.7	3.4	4.4	5.7	7.3	9.4% and higher

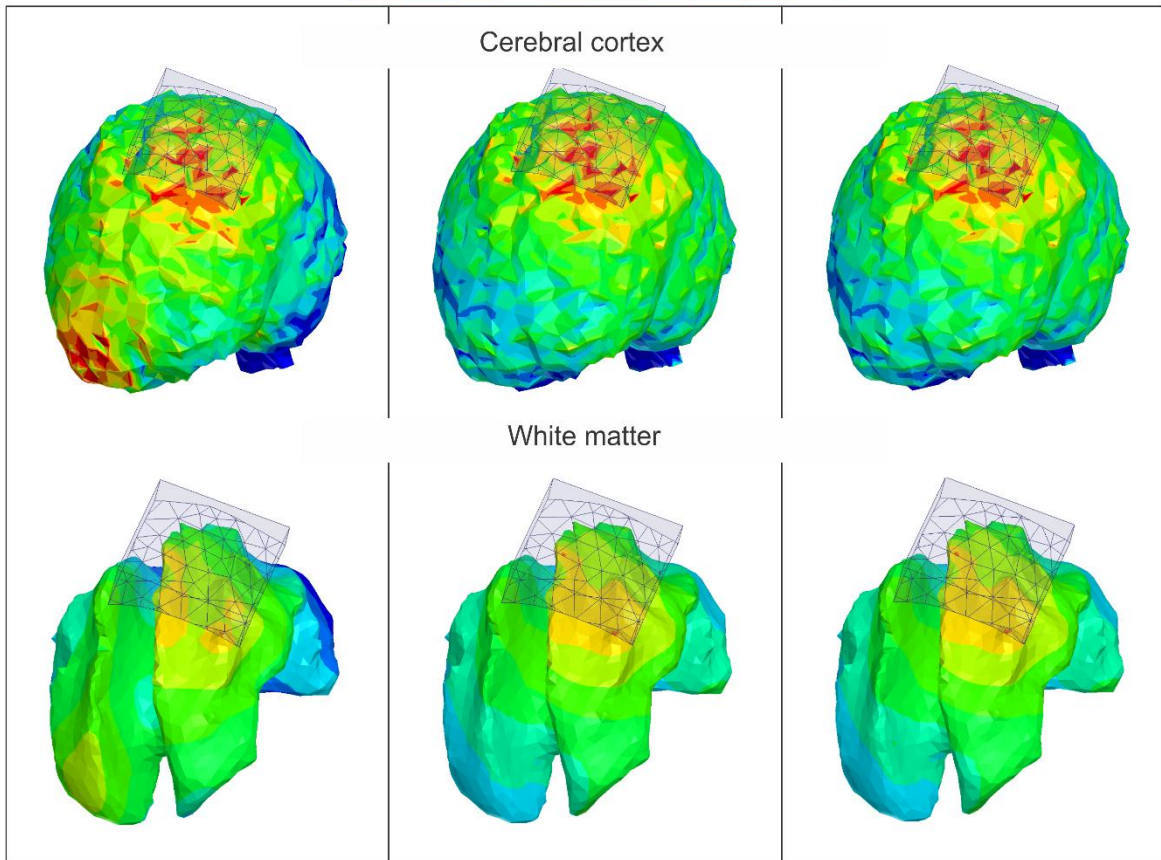


Fig. 5.3. Surface plots of the total current density on the cerebral cortex (row 2) and white matter (row 3). Total current density normalized by the input current density at the electrodes is shown. Column 1 provides results for the cephalic configuration while columns 2 and 3 display the contra-lateral and ipsi-lateral extracephalic results, respectively, using a logarithmic scale.

This would suggest stimulation of this region of the brain, which has been associated with planning and consciousness rather than body movement and coordination.

Special consideration should be given to the extracephalic configurations shown in Fig. 5.4-5.5. The depth of stimulation when using extracephalic cathode locations is visibly greater than that of the traditional cephalic arrangement. This would indicate that a greater percentage of the brain volume would be covered through extracephalic means.

This last observation about stimulation depth raises an interesting question of why electrodes placed in close proximity to what is essentially a highly conductive sphere of CSF encompassing the brain perform less efficiently than electrodes placed at farther locations.

### ***5.3.3. Total current density for axial cut planes***

Fig. 5.7 depicts an axial plane located approximately midway through the brain and intersects with the supraorbital cathode location. Results displayed in this plane indicate relatively deep stimulation regions for both extracephalic designs as compared with the traditional montage. Conversely, the traditional electrode configuration shows a much higher level of current flowing into the cathode.

### ***5.3.4 Total current density for 45 degree cut planes***

A diagonal cut-plane traversing the space between the anode at the top of the head and the traditional location for the cathode is shown in Fig. 5.8. A cephalic cathode configuration seems to show a relative shift in current density from the motor cortex to the frontal lobe. Virtually no stimulation beyond the parietal lobe is seen and while extracephalic configurations seem to somewhat better target the motor cortex, some stimulation of the rear of the brain is evident. This behavior is consistent in previous figures.

### ***5.3.5. Invariance of relative current densities to changes in Skin properties***

Relatively higher total current densities in the brain for extracephalic montages may be observed in Figs. 5.3-5.8. And yet, one potentially critical configuration would correspond to a very highly-conducting skin layer so that the bulk of current might be expected to flow closer to the surface, irrespective of the particular electrode montage (cephalic or extracephalic). As a test case, we consider here a hypothetical isotropic skin layer with the extreme conductivity of 0.25 S/m (wet epidermis) compared with dry skin from Table 5.1 in Fig. 5.9, which would model the electrode/skin interface as the electrode dries during an extended tDCS treatment session. Despite the expected overall decrease of the absolute current density in the brain, the relative patterns of current density distribution remain approximately the same for all three tested montages shown in Fig. 5.9! We think that these results may be directly extrapolated to the anisotropic case. Another justification of this result will be discussed further with reference to Fig. 5.10.

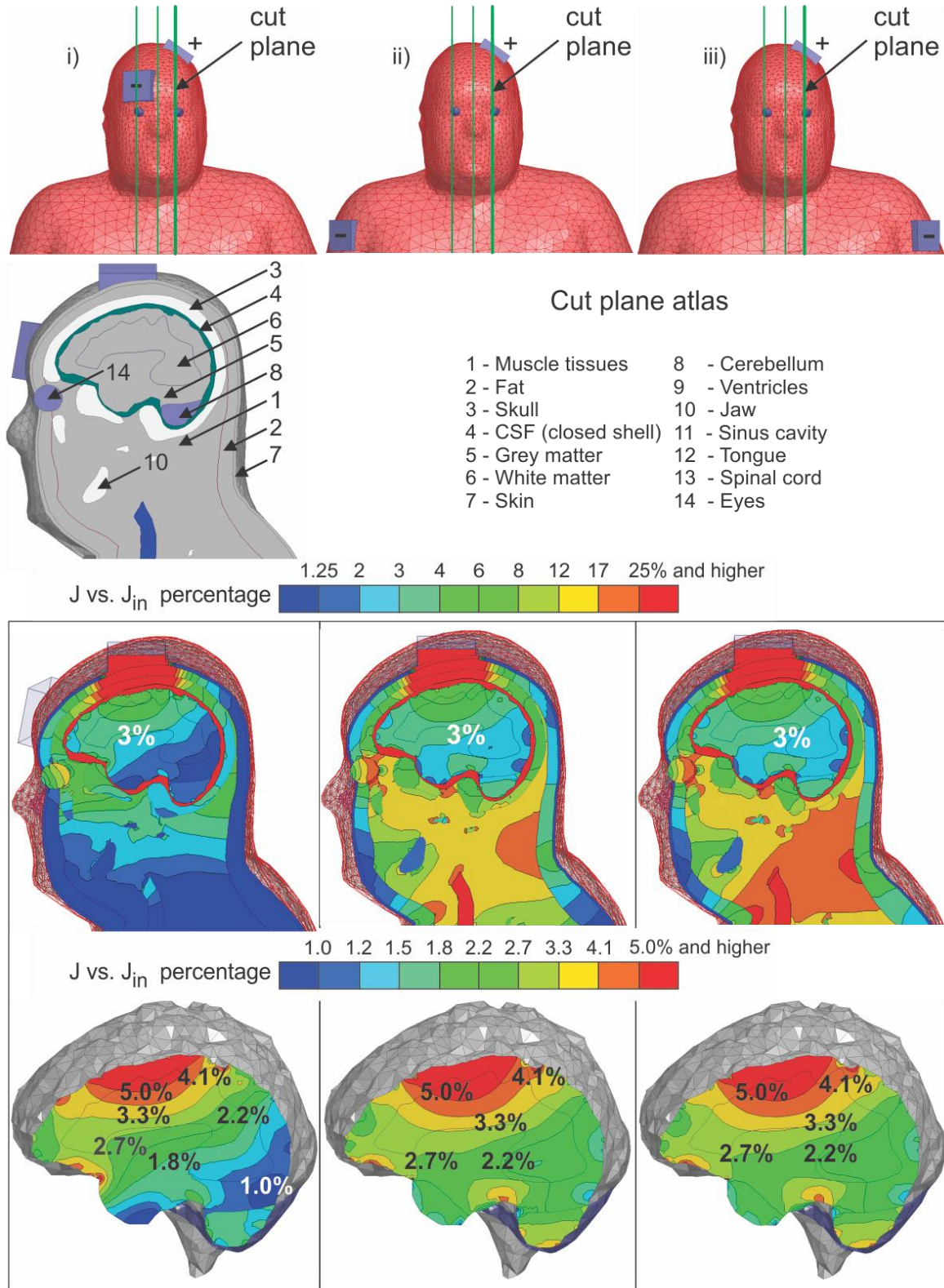


Fig. 5.4. Depictions of the contralateral supraorbital (i), extracephalic contralateral shoulder (ii), and extracephalic ipsilateral shoulder (iii) cathode montages. Total current density normalized by the input current density at the electrodes is shown projected onto three sagittal planes that progressively travel from the left to right on the model using a logarithmic scale.



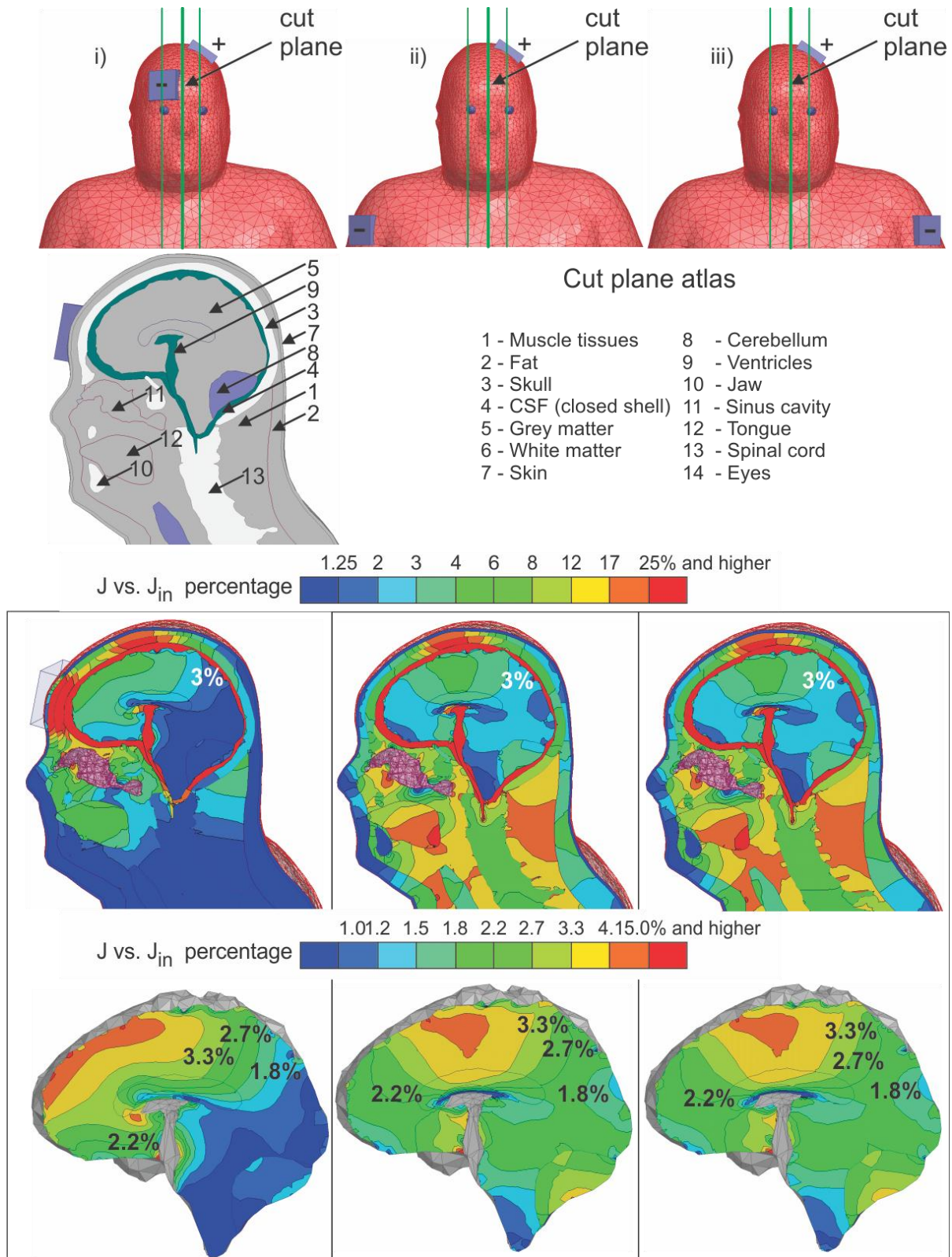


Fig. 5.5. Contralateral supraorbital (i), extracephalic contralateral shoulder (ii), and extracephalic ipsilateral shoulder (iii) cathode montages. Total current density normalized by the input current density at the electrodes is shown with surrounding body structures using a logarithmic scale.

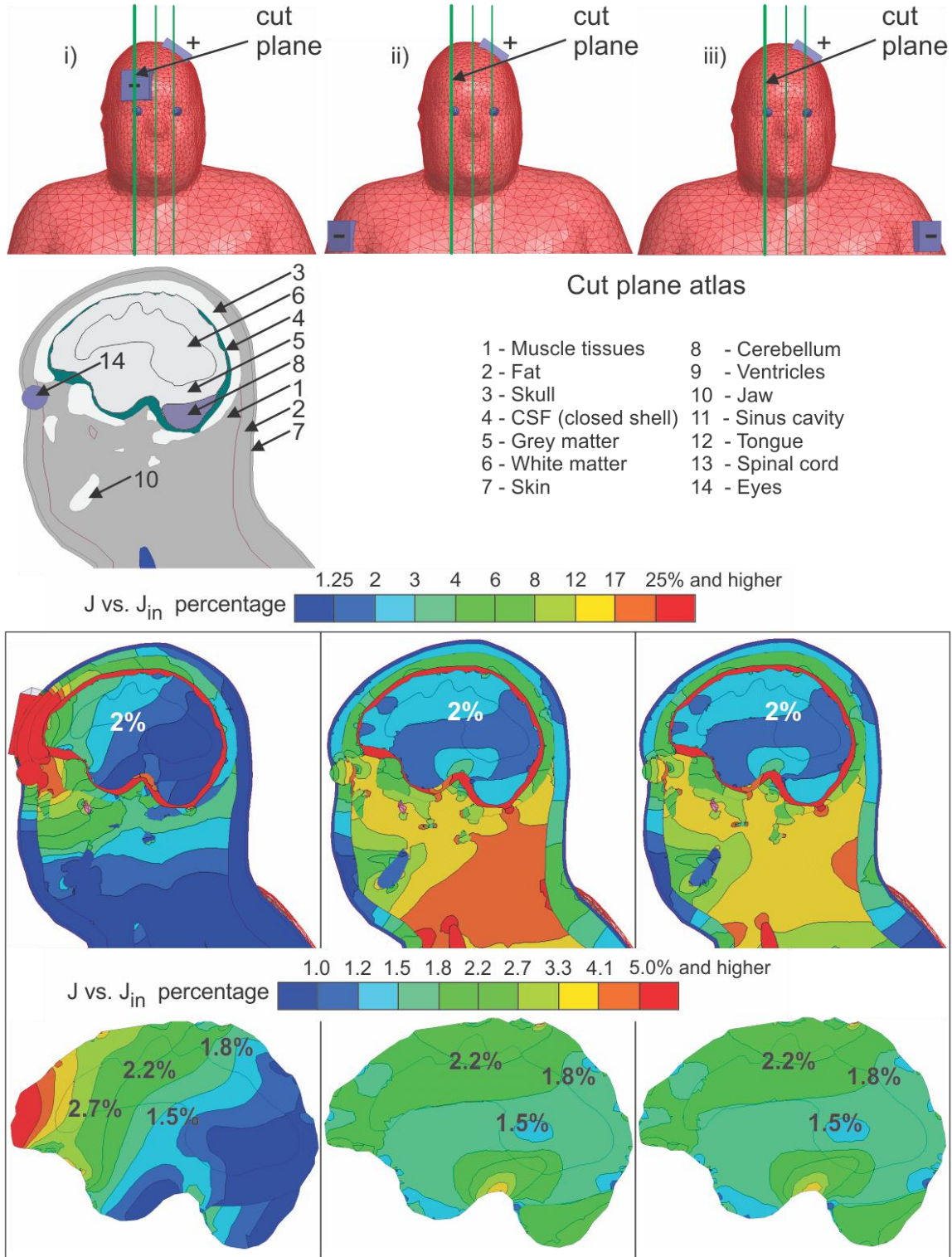


Fig. 5.6. Contralateral supraorbital (i), extracephalic contralateral shoulder (ii), and extracephalic ipsilateral shoulder (iii) cathode montages. Total current density normalized by the input current density at the electrodes is shown with surrounding body structures using a logarithmic scale.



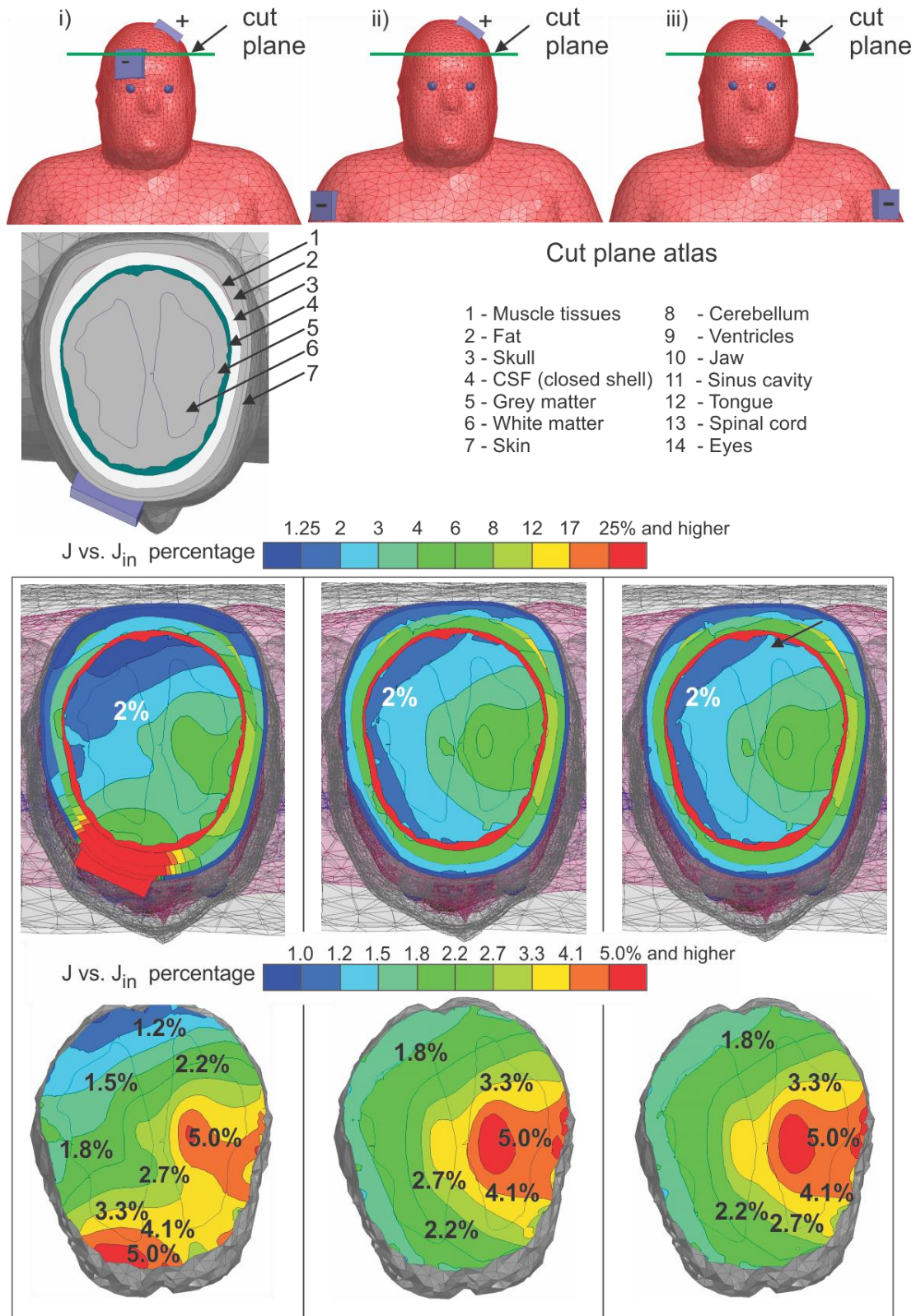


Fig. 5.7. Current densities projected onto an axial plane located halfway down the brain for the contralateral supraorbital (i), extracephalic contralateral shoulder (ii), and extracephalic ipsilateral shoulder (iii) montages. Total current density normalized by the input current density at the electrodes is shown using a logarithmic scale.

#### 5.4. Quantitative evaluation of vertical and horizontal average current densities

Results presented thus far rely upon a visual inspection of the total current density distribution in the different observation planes or on surfaces. It may be useful to separate the total current density into two partial components (vertical and horizontal), and then find the average values of these components,  $J_z^{avg}$ ,  $J_{xy}^{avg}$  for every lobe/cortex following Eq. (5.1). Fig. 5.10 reports numerically found average vertical and horizontal components of current densities in the brain including its individual subregions defined in Fig. 5.2. It can be seen from Fig. 5.10a that the vertical component of current density in every subregion increases when extracephalic montages (the results for both of them are nearly identical and cannot be distinguished in the figure) are used. However, the horizontal component of current density in Fig. 5.10b either decreases or remains nearly the same compared to the cephalic case. This may be instrumental when stimulating brain regions with cell structures that are biased in either the vertical or horizontal directions. The results for extremely wet skin shown in Fig. 5.10c, d, respectively, follow a similar tendency although the vertical current components in the primary motor cortex and in the somatosensory cortex become close to each other for both competing montages. Note that the cephalic montage is much less sensitive to variations in skin properties.

#### 5.5. Expected electrode voltages and their variations

Cephalic and extracephalic configurations require different electrode voltages for the same amount of current. This section provides the corresponding estimates including voltage variation margins. To investigate this and related problems we introduce the voltage response of a tissue/organ to small changes in tissue conductivity. Given the independent current source  $I_{in}$  as an excitation, the dimensionless (dynamic or small-signal) voltage response may be defined as

$$S = -\frac{dV/V_0}{d\sigma/\sigma_0} > 0 \quad (5.2)$$

where  $d\sigma$  is the tissue conductivity variation and  $dV$  is the corresponding electrode voltage variation about the unperturbed state  $V_0$ ,  $\sigma_0$ . If a particular tissue carries a significant current, its corresponding voltage response should be large. This fact follows from the local form of Ohm's law. Table 5.3 summarizes unperturbed electrode voltages and voltage responses of individual tissues for the three electrode configurations. The C3-Fp2 montage possesses a very small voltage response for the muscle tissue since there is virtually no such tissue within the main current path (only the skin, and the fat are two layers around the skull). In this analysis, we consider the brain as one entity. Based on the results of Table 5.3 for individual voltage responses, we estimate the electrode voltages and their extremes given maximum  $\pm 20\%$  conductivity variations for various montages as: (i) cephalic:  $\sim 300 \text{ mV} \pm 60 \text{ mV}$ ; (ii) extracephalic ipsilateral:  $\sim 720 \text{ mV} \pm 120 \text{ mV}$ ; (iii) extracephalic contralateral:  $\sim 710 \text{ mV} \pm 120 \text{ mV}$ .



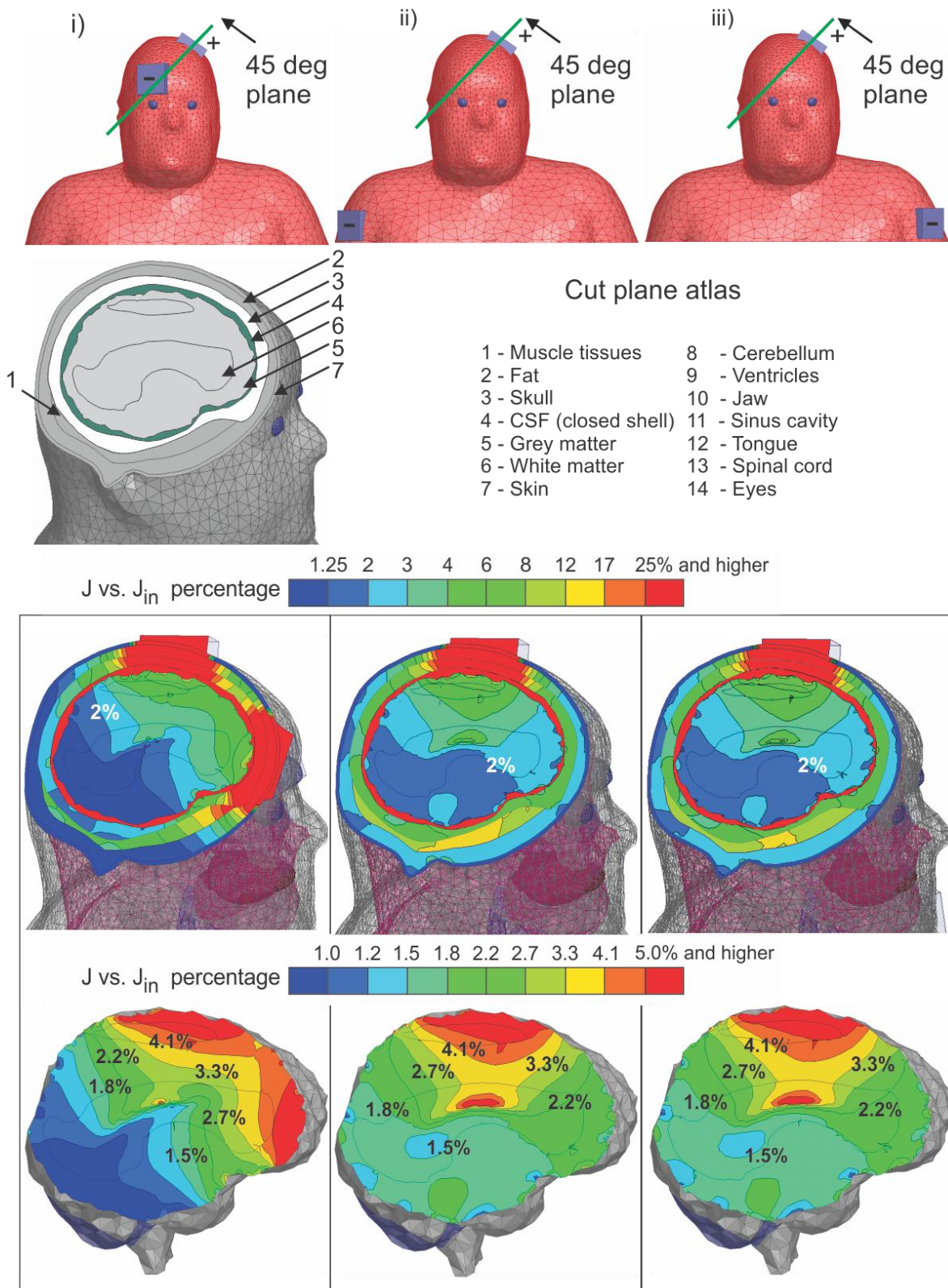


Fig. 5.8. Diagonal cut-plane between the anode and supraorbital cathode displaying normalized total current densities for the contralateral supraorbital (i), extracephalic contralateral shoulder (ii), and extracephalic ipsilateral (iii) montages using a logarithmic scale.

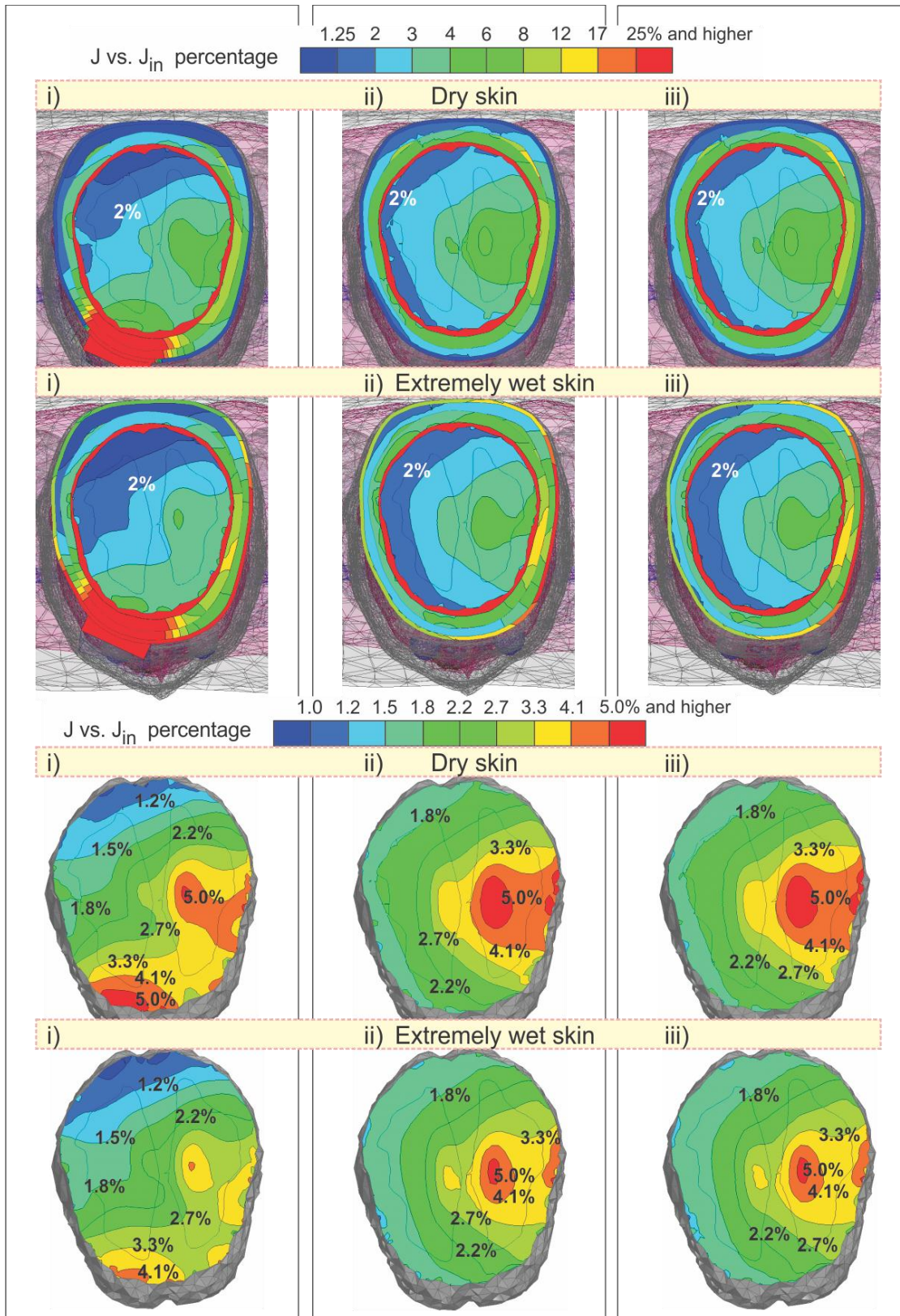


Fig. 5.9. Comparison of tDCS simulation results from Fig. 5.7. as a function of skin conductivity. Total current densities projected onto an axial plane located halfway down the brain for the contralateral supraorbital (i), extracephalic contralateral shoulder (ii), and extracephalic ipsilateral shoulder (iii) montages. Note that the images are employing a logarithmic scale.

Table 5.3 – Electrode voltages and dimensionless voltage response. All dimensional voltage data are related to a current source with the electrode normal current density of  $J_{in} = 0.08mA/cm^2$  and the total source current of  $I_{in} = 25cm^2 \times J_{in} = 2mA$

Parameter	Tissue					
	Skin	Fat	Muscle	Skull	CSF	Brain (GM, WM, Cerebellum)
Conductivity	0.00002	0.038	0.2	0.076	2.00	0.028 0.028 0.048
C3 – Fp2 Montage						
$V_0, V$	19.334					
V for 20% cond. Change, V	16.19	19.29	19.33	19.32	19.32	19.33
$S \times 10^3$	813	11	0	5	3	1
C3 – Extracephalic Ipsilateral Shoulder Montage						
$V_0, V$	21.99					
V for 20% cond. Change, V	18.46	21.91	21.94	21.98	21.98	21.98
$S \times 10^3$	802	17	10	2	3	0
C3 – Extracephalic Contralateral Shoulder Montage						
$V_0, V$	21.84					
V for 20% cond. Change, V	18.41	21.84	21.88	21.91	21.91	21.92
$S \times 10^3$	801	18	9	2	2	0

## 5.6. Discussion

### 5.6.1. General observations

Given the results described in the previous sections, the following observations can be made:

- I. Extracephalic montages might create larger total current densities in deeper brain regions, specifically in white matter as compared to an otherwise equivalent cephalic montage.
- II. Extracephalic montages might create larger average vertical current densities in the primary motor cortex and in the somatosensory cortex. At the same time, the horizontal current density either remains approximately the same or decreases.
- III. The previous observation becomes significantly less apparent for a very wet skin.
- IV. The extracephalic montages may reduce the large percentage of the applied current passing through the frontal cortex when the cathode is located at the contralateral supraorbital location.



Indeed, the data presented in Figs. 5.3 through 5.10 is related to only one particular cephalic electrode configuration studied in this paper. Furthermore, it is clearly dependent on both the model construction and tissue conductivity values.

To address the last concern, we have compared our findings with simulation data from a similar problem (cephalic versus extracephalic configurations) solved numerically in Ref. [28].

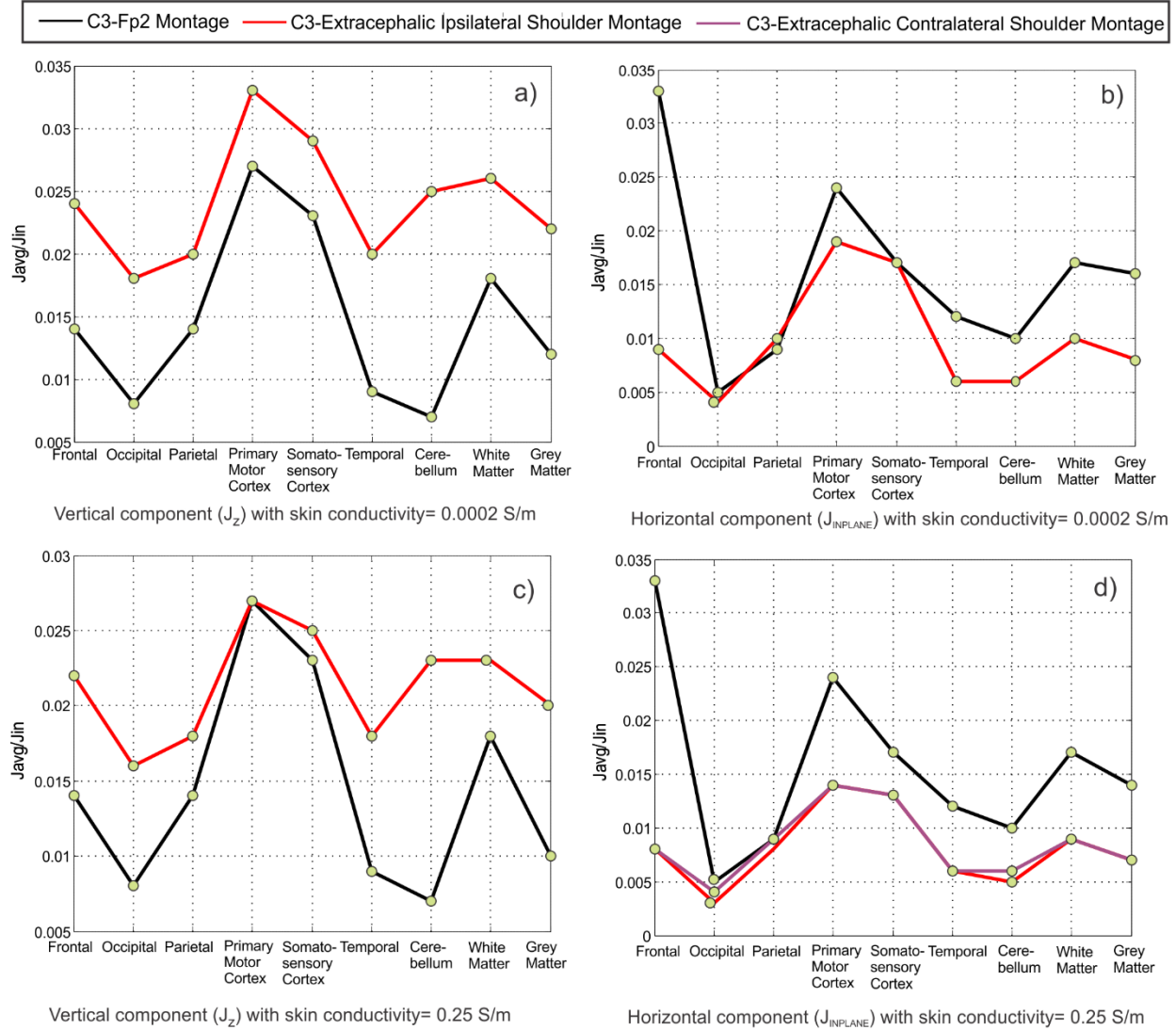


Fig. 5.10. Averaged values of the vertical and horizontal current density components for the brain substructures shown in Fig. 5.2 and total white and grey matter. Rows 1 and 2 depict results for dry and wet skin, respectively. Ipsi- and contralateral results were identical except in the lower right of Fig. 5.10d.

The FEM model used in this work did not include any layer of fat (which has a significantly lower conductivity value [27]) around the skull. Instead, a homogeneous thick skin layer with a high conductivity value of 0.43 S/m has been used. The authors stated that “the use of extracephalic montage does not significantly increase the amount of current penetration through the skull.” The

figure of merit was apparently the current density map at the surface of the cerebral cortex. Such a result is in agreement with our data presented in Fig. 5.10c, d where we see that some potential advantages of the extracephalic configuration may rapidly disappear when the skin conductivity becomes very high.

### ***5.6.2. Invariance of extracephalic montages***

The density of current flow within the body during extracephalic stimulation is weakly dependent on the choice of the shoulder location. In both ipsi- and contralateral cathode montages, current densities in the human head are nearly identical. This makes intuitive sense, as current needs to flow toward the cathode through the neck. Above the neck, the current distribution is insensitive to shoulder electrode positions. This is similar to water flow in a closed container in the form of a human body where the anode is a source, the cathode is a sink, and the neck is acting as a choke point. Thus, there is freedom in choosing the extracephalic electrode location. This may alleviate concerns regarding extraneous stimulation of other body areas (i.e., disrupting the autonomic nature of heart muscle regulation by the sinoatrial node, etc.).

### ***5.6.3. Validation of results across configurations***

Along with the previously reported extreme case, the current density distribution behavior observed in Figs. 5.3-5.10 has been confirmed for:

- i. Different tissue conductivities (every value was separately varied by  $\pm 20\%$  );
- ii. Different body mass values (scaling the entire structure by  $5 \times 5 \times 5\%$  while keeping the electrode size the same);
- iii. Homogeneous versus non-homogeneous brain structures (assigning average conductivity values to white/grey matter/cerebellum).

### ***5.6.4. Conclusions***

It has been shown that extracephalic montages might create larger total current densities in deeper brain regions, specifically in white matter as compared to an equivalent cephalic montage. Extracephalic montages might also create larger average vertical current densities in the primary motor cortex and in the somatosensory cortex. At the same time, the horizontal current density either remains approximately the same or decreases. The metrics used in this paper include either the total local current density through the entire brain volume or the average vertical and horizontal current densities for each individual lobe/cortex.

## References

- [1] M.A. Nitsche, L.G. Cohen, E.M. Wassermann, A. Priori, N. Lang, A. Antal, W. Paulus, F. Hummel, P.S. Boggio, F. Fregni, A. Pascual-Leone, "Transcranial Direct Current Stimulation: State of the Art 2008", *Brain Stimulation*, vol. 1, pp. 206-223, 2008.
- [2] A.R. Brunoni, M.A. Nitsche, N. Bolognini, M. Bikson, T. Wagner, L. Merabet, D.J. Edwards, A. Valero-Cabre, A. Rotenberg, A. Pascual-Leone, R. Ferrucci, A. Priori, P.S. Boggio, F. Fregni, "Clinical research with transcranial direct current stimulation (tDCS): Challenges and future directions", *Brain Stimulation*, vol. 5, pp. 175-195, 2012.
- [3] S. Rush, D.A. Driscoll, "Current distribution in the brain from surface electrodes", *Anaest Analg Curr Res*, vol. 47, pp. 717-723, 1968.
- [4] M. Bikson, A. Rahman, A. Datta, "Computational models of transcranial direct current stimulation", *Clinical EEG and Neuroscience*, vol. 43, pp. 176-183, 2012.
- [5] T. Wagner, F. Fregni, S. Fecteau, A. Grodzinsky, M. Zahn, A. Pascual-Leone, "Transcranial direct current stimulation: a computer-based human model study", *NeuroImage*, vol. 35, pp. 1113-1124, 2007.
- [6] A. Datta, M. Elwassif, F. Battaglia, M. Bikson, "Transcranial current stimulation focality using disc and ring electrode configurations: FEM analysis", *J. Neural Eng.*, vol. 5, pp. 163-174, 2008.
- [7] P.C. Miranda, M. Lomarev, M. Hallett, "Modeling the current distribution during transcranial direct current stimulation", *Clinical Neurophysiology*, vol. 117, pp. 1623-1629, 2006.
- [8] P.C. Miranda, A. Mekonnen, R. Salvador, G. Ruffini, "The electric field in the cortex during transcranial current stimulation", *NeuroImage*, vol. 70, pp. 48-58, 2013.
- [9] M. Bikson, A. Rahman, A. Datta, F. Fregni, L. Merabet, "High-resolution modeling assisted design of customized and individualized transcranial direct current stimulation protocols", *Neuromodulation: Technology at the Neural Interface*, vol. 15, pp. 306-315, 2012.
- [10] M. Bikson, A. Datta, "Guidelines for precise and accurate computational models of tDCS", *Brain Stimulation*, vol. 5, pp. 430-434, 2012.
- [11] A. Datta, X. Zhou, Y. Su, L.C. Parra, M. Bikson, "Validation of finite element model of transcranial electrical stimulation using scalp potentials: implications for clinical dose", *J Neural Engineering*, vol. 10, pp. 2013.
- [12] S. Shahid, P. Wen, T. Ahfock, "Assessment of electric field distribution in anisotropic cortical and subcortical regions under the influence of tDCS", *Bioelectromagnetics*, vol. 35, pp. 41-57, 2014.
- [13] H.S. Suh, W.H. Lee, T.-S. Kim, "Influence of anisotropic conductivity in the skull and white matter on transcranial direct current stimulation via an anatomically realistic finite element head model", *Phys. Med. Biol.*, vol. 57, pp. 6961-80, 2012.
- [14] A. Priori, "Brain polarization in humans: a reappraisal of an old tool for prolonged non-invasive modulation of brain excitability", *Clinical Neurophysiology*, vol. 114, pp. 589-595, 2003.
- [15] M.A. Nitsche, S. Doemkes, T. Karakose, A. Antal, D. Liebetanz, N. Lang, F. Tergau, W. Paulus, "Shaping the effects of Transcranial direct current stimulation of the human motor cortex", *J Neurophysiol*, vol. 97, pp. 3109-3117, 2007.
- [16] M. Bikson, A. Datta, A. Rahman, J. Scaturro, "Electrode montages for tDCS and weak transcranial electrical stimulation: role of 'return' electrode's position and size", *Clinical Neurophysiology*, vol. 121, pp. 1976-1978, 2010.

- [17] A.F. DaSilva, M.S. Volz, M. Bikson, F. Fregni, "Electrode positioning and montage in transcranial direct current stimulation", *J. Vis Exp*, vol. 51, 2011.
- [18] F. Cogiamanian, S. Marceglia, G. Ardolino, S. Barbieri, A. Priori, "Improved isometric force endurance after transcranial direct current stimulation over the human motor cortical areas", *Eur J Neurosci*, vol. 26, pp. 242-249, 2007.
- [19] D.M. Martin, A. Alonzo, P.B. Mitchell, P. Sachdev, V. Galvez, C.K. Loo, "Fronto-extracerebral transcranial direct current stimulation as a treatment for major depression: an open-label pilot study", *J Affect Disord*, vol. 134, pp. 459-463, 2011.
- [20] U. Ziemann, W. Paulus, M.A. Nitsche, A. Pascual-Leone, W.D. Byblow, A. Berardelli, H.R. Siebner, J. Classen, L.G. Cohen, J.C. Rothwell, "Consensus: motor cortex plasticity protocols", *Brain Stimulation*, vol. 1, pp. 164-182, 2008.
- [21] Y. Vandermeeren, J. Jamart, M. Osseman, "Effect of tDCS with an extracerebral reference electrode on cardio-respiratory and autonomic functions", *BMC Neurosci*, pp. 11-38, 2010.
- [22] C. Gabriel, S. Gabriel, E. Corthout, "The Dielectric Properties of Biological Tissues: I. Literature Survey", *Phys. Med. Biol.*, vol. 41, pp. 2231-2249, 1996.
- [23] S. Gabriel, R.W. Lau, C. Gabriel, "The Dielectric Properties of Biological Tissues: II. Measurements in the Frequency Range 10 Hz to 20 GHz," *Phys. Med. Biol.*, vol. 41, pp. 2251-2269, 1996.
- [24] C. Gabriel. Compilation of the Dielectric Properties of Body Tissues at RF and Microwave Frequencies, Report N.AL/OE-TR- 1996-0037, Occupational and environmental health directorate, Radiofrequency Radiation Division, Brooks Air Force Base, Texas (USA), 1996.
- [25] D.Andreuccetti, R.Fossi and C.Petrucci: An Internet resource for the calculation of the dielectric properties of body tissues in the frequency range 10 Hz - 100 GHz. Website at <http://niremf.ifac.cnr.it/tissprop/>. IFAC-CNR, Florence (Italy), 1997. Based on data published by C.Gabriel et al. in 1996.
- [26] D. Miklavcic, N. Pavselj, F.X. Hart, "Electric Properties of Tissues", in Wiley Encyclopedia of Biomedical Engineering, M. Akay, ed., New York: John Wiley & Sons, 2006.
- [27] *IT'IS Material Property Database*, Retrieved Oct. 2<sup>nd</sup> 2013 from <http://www.itis.ethz.ch/itis-for-health/tissue-properties/overview/>
- [28] C.H. Im, J.H. Park, M. Shim, W.H. Chang, Y.H. Kim, "Evaluation of local electric fields generated by transcranial direct current stimulation with an extracerebral reference electrode based on realistic 3D body modeling," *Phys Med Biol*, vol. 57, pp. 2137-50, 2012.



## Chapter 6

# Future work and potential applications of the VHP – Female Model

### Introduction

The appendix discusses applications which are in the initial stages of development that vary from high frequency to low frequency. Primarily, we discuss the possible and potentially unexplored areas of transcranial Direct Current Simulation (tDCS). In specific, we are interested in how tDCS would impact a patient with an implant. Later, techniques aimed at developing noninvasive methods to examine the body quality are discussed. This preliminary study has been performed on the Ansoft male human body model and further stages of development are planned to be executed on VHP – Female model. The development and simulations of these ideas would enable us to study by varying the desired variables in the VHP – Female model. For example, we can deform a particular tissue based on the application.

### *6.1. Potential areas to be explored in tDCS*

In Chapter 05, we see that the stimulation of the brain through tDCS is very much dependent on the conductivity of the tissues. The cases of dry and wet skin were discussed in Chapter 05. All studies around the world have specific requirements for subjects such as no brain anomalies, no implants, no stents or metal parts in brain etc.[1]. Most of the age groups who require tDCS have a good probability to have an implant such as a pacemaker.

In the initial study, we are trying to understand the impact of a pacemaker when the patient is under tDCS treatment. Currently, Altrua60 S603, a product of *Boston Scientific* is being modelled in MAXWELL 3D [2]. The modelling needs to be close to the actual dimensions to understand the impact of the pacemaker.

Ideally, when metal parts are implanted we can anticipate that the current flow would be altered due to this implant. This metal can cause dense currents that result in heating. For example, a metal piece in the shoulder blade or spine when extra cephalic based tDCS configuration is used can cause heating of surrounding tissues.

In case of pacemaker, the casing is insulated and so is the most part of the leads which run from the casing to the heart. The only part which is not insulated is the tip of the lead which is in direct contact with the heart. Pacemakers can be unipolar or bipolar, that is, one or two leads depending on the patient's requirement. The area of concern is if any potential difference would be created between the lead tips in case of a bipolar pacemaker. This would result in a current flow in the cardiac muscle. An illustration of how a model of the pacemaker within the human body would look like is shown in Fig. 6.1. Currently, the battery and circuit casing have been designed to scale. The connector has not been included for preliminary studies and the leads are not accurate to scale.

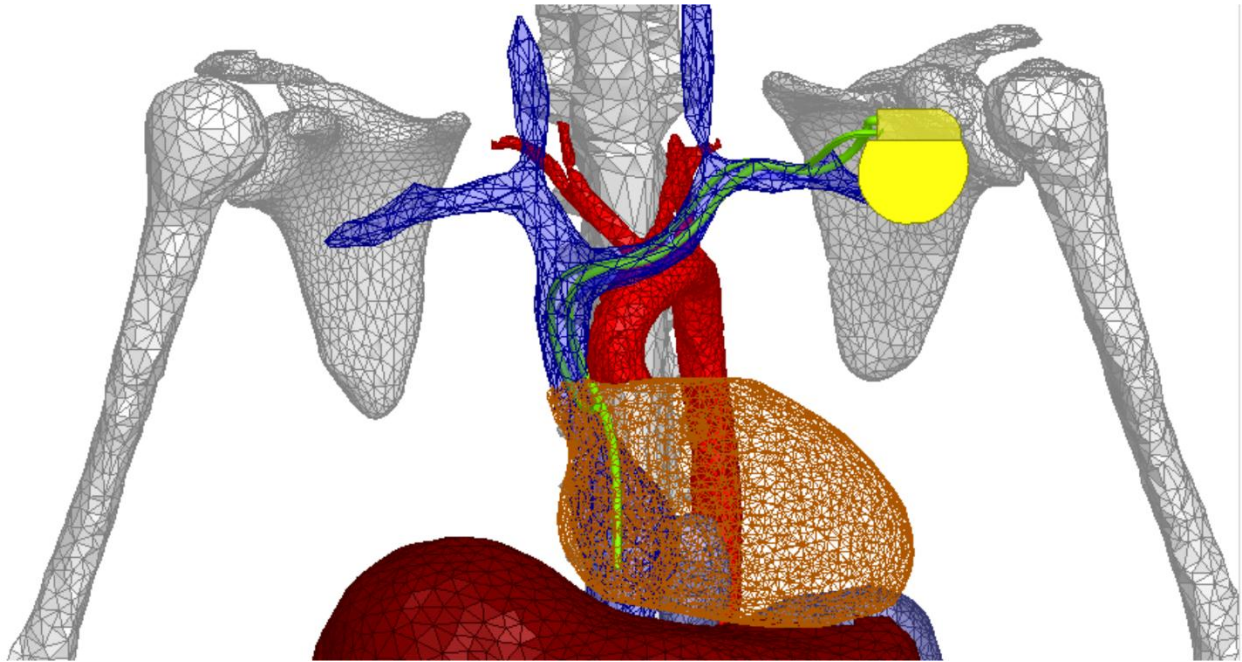


Fig.6.1. Illustration of the pacemaker Altrua 60 S 603 is shown in yellow and the leads in green. Note the tissues and organs are hidden for demonstration.

Other areas of interest are to study the placement of multiple electrodes and its optimization [3], variation of fat and skin thickness and to examine the impact of anisotropic material properties [4].

## ***6.2. Potential application in non-invasive study of bone quality***

The primary focus of this preliminary study is to find a non – invasive electromagnetic tomographic approach, which can be applied to patients suffering from osteoporosis. In this case, the femur bone become porous and weakens resulting in change in material property. The key is to detect this change in the material property of the inner part of the bone. This appendix outlines various potential techniques which might be the future of non-invasive bone studies.

To emphasize on the magnitude by which the material properties change in an osteoporotic bone, where the yellow bone marrow replaces the spongy cancellous bone, Fig 6.2 shows the dielectric constant and Fig 6.3 shows the conductivity of various tissues changing with respect to frequency in the area of interest [5].

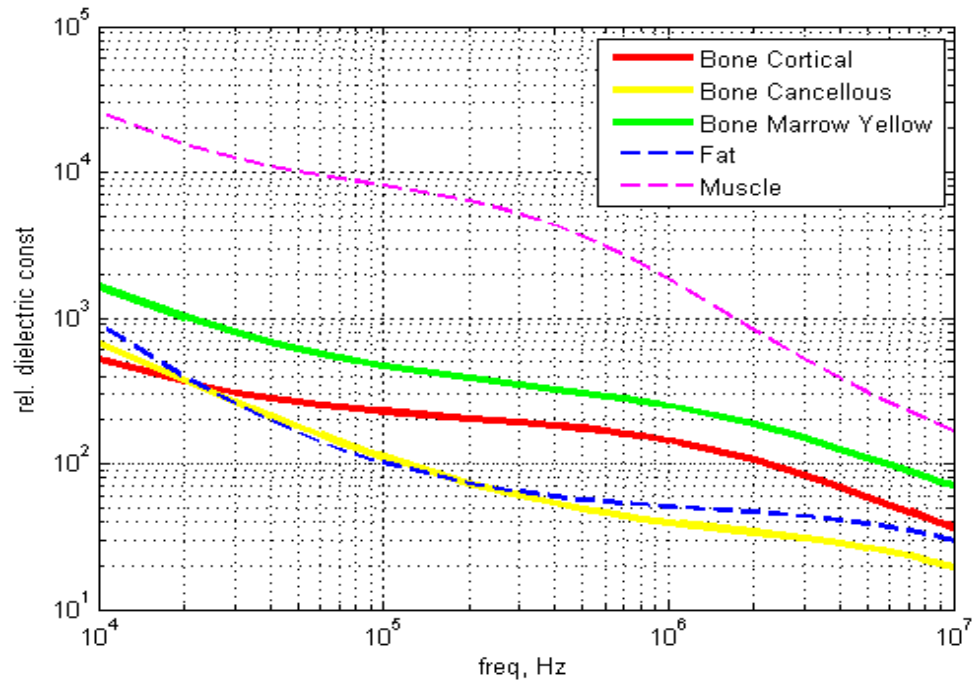


Fig 6.2. Relative dielectric constant of various tissues such as cancellous bone and yellow bone marrow are plotted with respect to frequency.

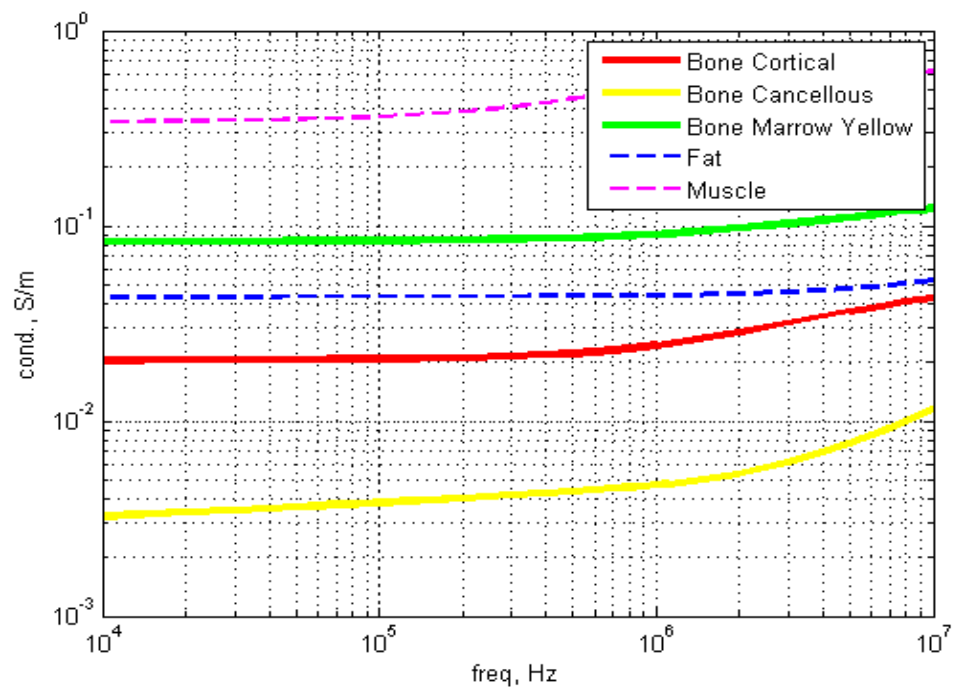


Fig 6.3. Conductivity of various tissues such as cancellous bone and yellow bone marrow are plotted with respect to frequency.

### 6.2.1. Electric Impedance Tomography (EIT)

Electric Impedance Tomography (EIT) is a well-known biomedical research tool for extracting the volumetric conductivity map of an unknown composite tissue from surface electrode measurements using electrode arrays of different sizes (from 2 up to 100 or so) [6], [7]. Here, current is injected and the distribution profile is studied. Using reconstruction techniques including but not limited to back-projection method, iterative method and one-step linearized method, you can create the impedance map of the subject under consideration [6]. Hence, we might be able to use this proposed method to detect any abnormalities. For preliminary studies, we use a ring of 8 electrodes attached externally to the body and the opposite electrodes are excited one pair at a time, in round robin fashion. The idea is to measure the voltages across electrodes and to use a suitable back propagation method to detect the abnormality in the material properties contained in the body. Fig. 6.4 illustrates how the set up in this experiment would look like in MAXWELL 3D. EIT has a great potential as it is an inexpensive and quite flexible technique.

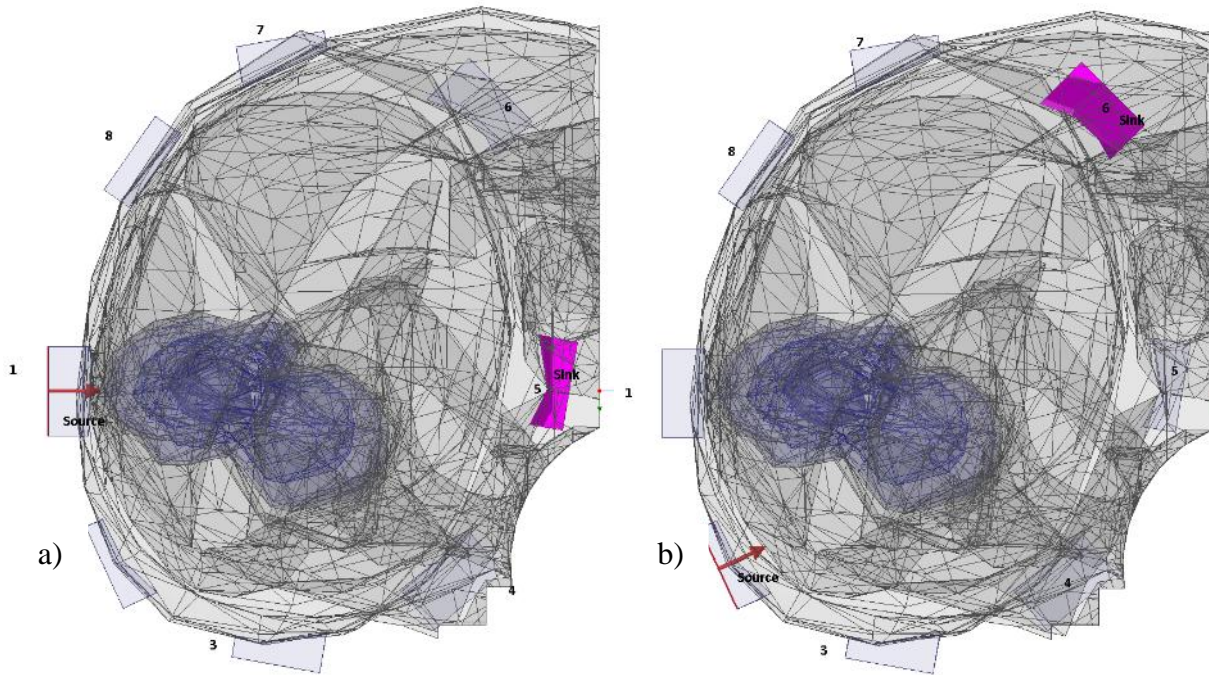


Fig 6.4. Illustration of EIT applied to the thigh region of the ANSOFT human body containing the femur bone, a) – Shows electrode 1 as anode and electrode 5 as sink/cathode highlighted b) – electrode 2 as anode and 6 as sink.

### 6.2.2. Magnetic Induction Tomography

Now, we will use a quasi-static magnetic field, which easily penetrates the cortical bone. This methodology has been inspired by Nondestructive Testing (NDT) of conducting materials. Eddy currents are excited in a material of interest by the “exciting coils”. The exciting coils are located in close proximity to the target. The magnitude of eddy currents depends on the internal structure (conductivity) of different material parts. The current magnitude can be directly be correlated to



the deteriorating femur. After being excited the eddy currents create their own magnetic field, which is recorded by a pickup coil or coils.

The pickup coils sample the magnetic fields and in this study they will simply be replaced by the magnetic- field probes. The exciting coil will have a bent figure - eight shape. The frequency range is from 100 Hz to 10000 Hz.

Fig. 6.5 shows the proposed methodology where the two exciting coils (or one figure-eight coil) are placed around the femur region of a healthy individual (ANSYS Human Body Model).

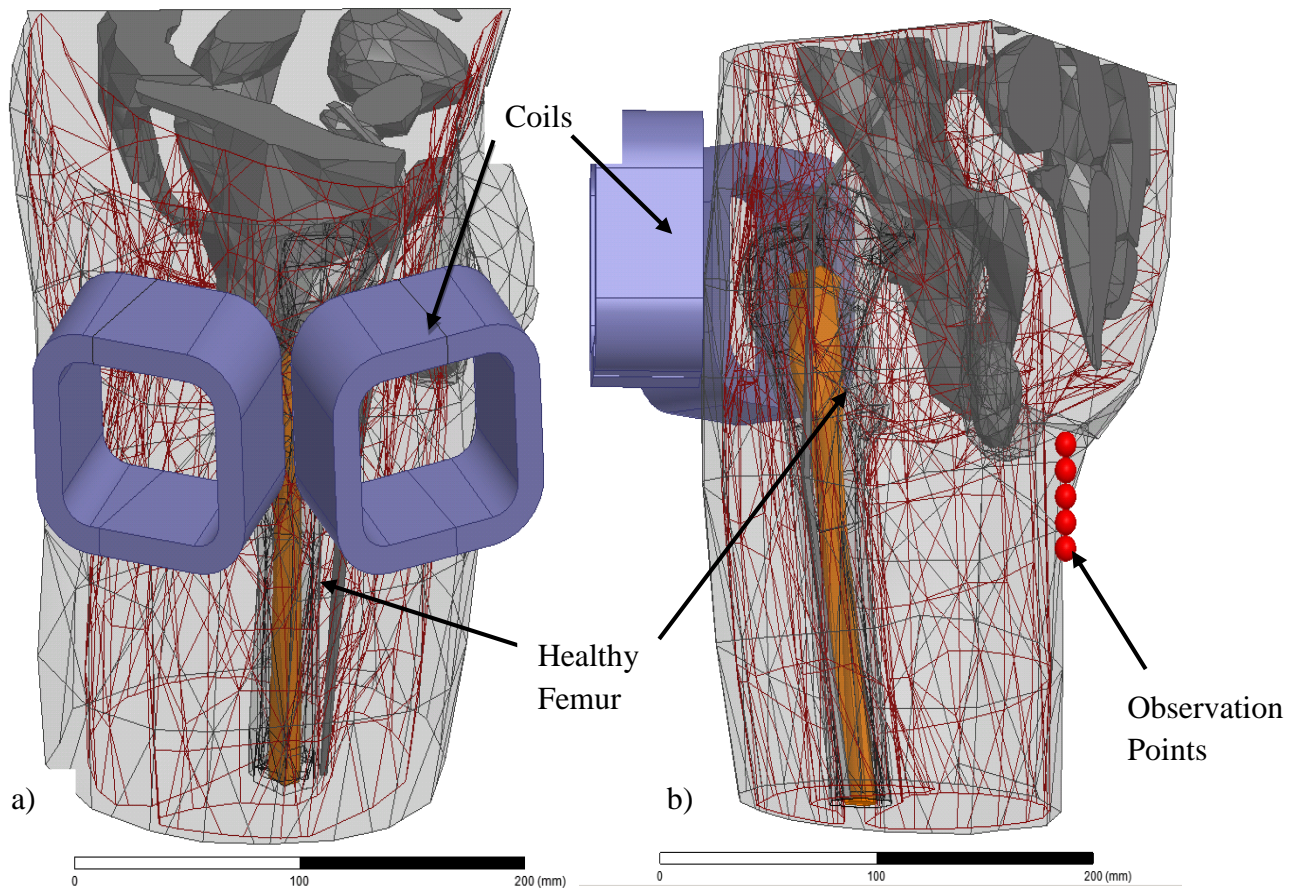


Fig. 6.5. a) - 3 D view of the selected region of the thigh depicting the coils around the femur of a healthy individual  
b) - 3 D view of the coils surrounding the femur of a healthy individual for magnetic induction tomography.

Similarly, Fig. 6.6 shows a similar set up around the femur region for an osteoporotic individual. The observation points are also marked.

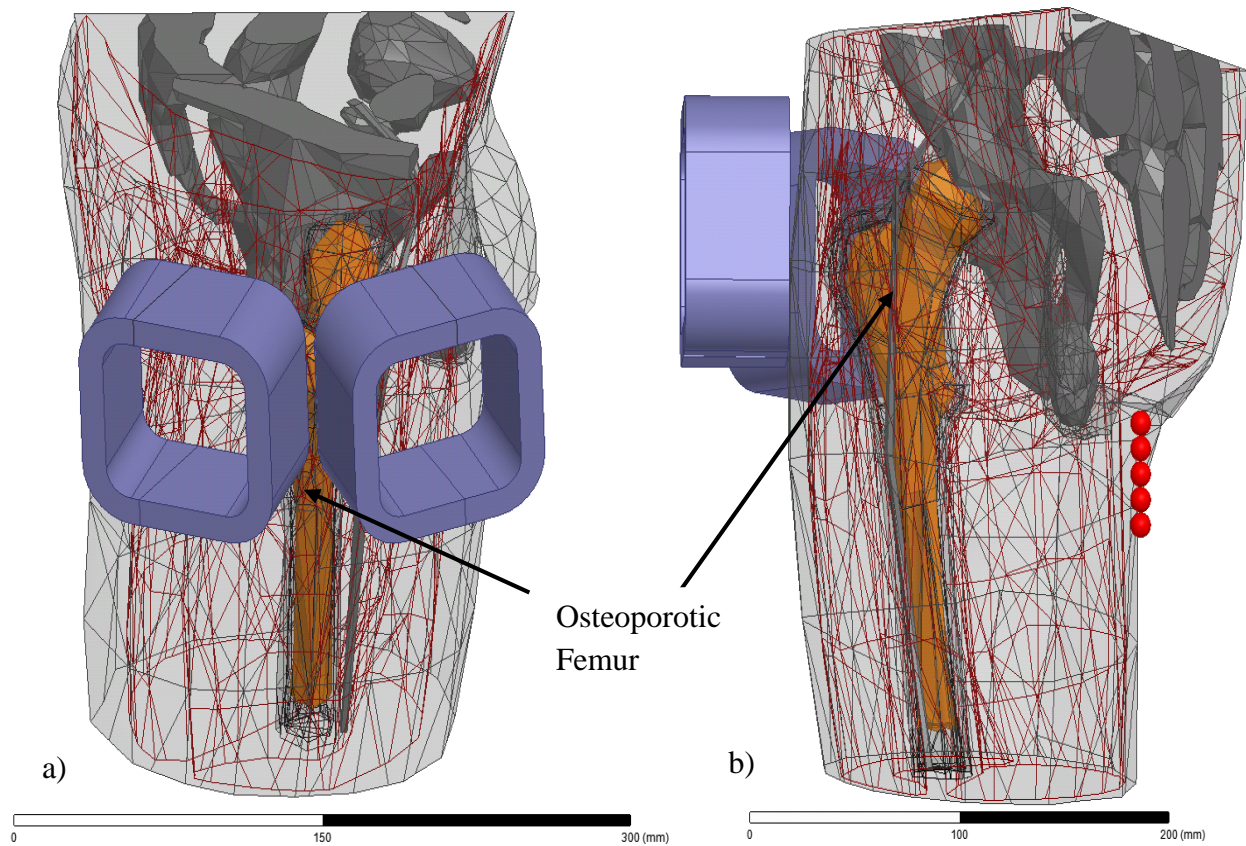


Fig.6.6. a) - 3 D view of the selected region of the thigh depicting the coils around the femur for an osteoporotic individual b) - 3 D view of the coils surrounding the Femur for an osteoporotic individual for magnetic induction tomography.

The magnetic field  $\Delta \vec{B}$  (magnetic induction) is the secondary signal due to the eddy currents present at the reference points. The conduction currents induced in the sample cause a component in phase of  $\Delta \vec{B}$  which is proportional to frequency and lags the primary field by 90 degrees. In general,  $\Delta \vec{B}$  will have real and imaginary components representing the permittivity and conductivity of the sample respectively. For biological tissues, the imaginary component will normally dominate. Hence we can compare the imaginary value of the secondary signal to detect the inner materials [8]. Though there are challenges such as interference, screens may be used to reduce this to an extent. Fig 6.7 shows the magnetic field distribution from a sample simulation.



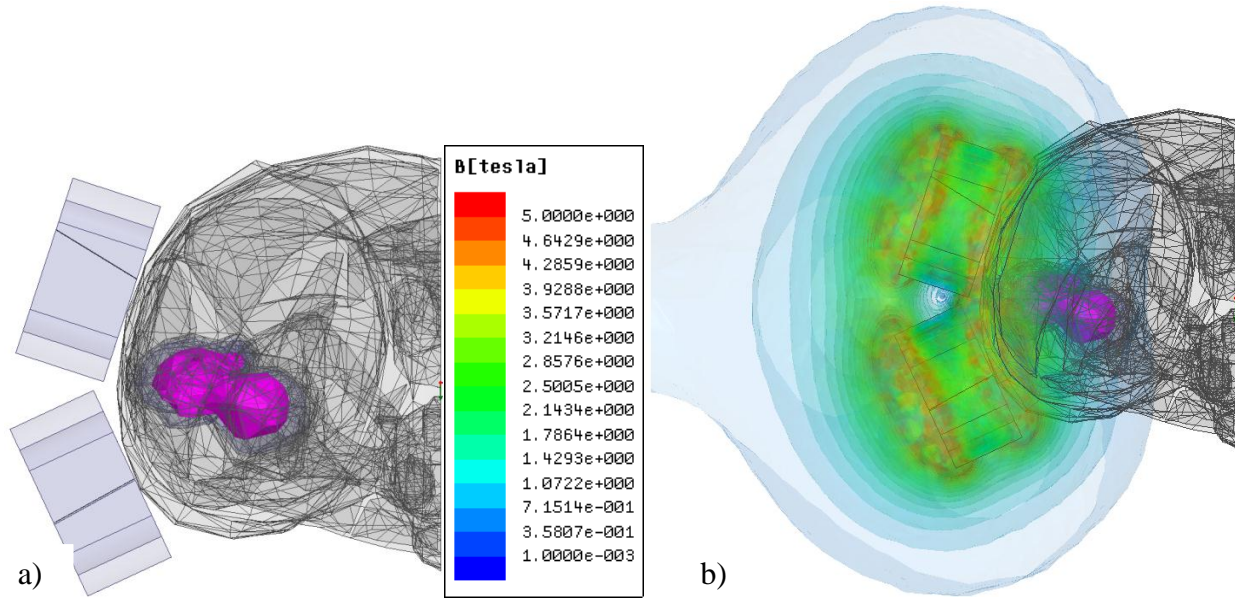


Fig. 6.7. a) - Top view of the selected region of the thigh depicting the coils around the Femur for an osteoporotic individual (highlighted) b) - Top view of the magnetic field surrounding the Femur for an osteoporotic individual.

### 6.2.3. Electromagnetic Tomography- RF Approach

Two loop antennas are used as a part of preliminary study, which radiate magnetic field which easily penetrates the cortical bone. The loop antennas are placed conformal to the human body [9]. The resonance frequency depends on the internal structure (conductivity and permittivity) of different material parts. The resonance frequency of a loop antenna in a dielectric material occurs at a lower frequency when compared to an antenna in air. Hence, the changes in the deteriorating femur can be a direct reflection of the resonant frequency for the antenna setup. Simulation setup in HFSS and sample results are presented.

The loop antennas act as a transmitter antenna and receiver antenna and vice versa. The first loop antenna is inclined at an angle of 30 degrees to the transverse plane such that the top end of the copper loop surrounds the head of the femur. The second loop antenna is about 9 mm away from the bottom of the first loop. The width of each copper strip of each antenna is 10 mm. The frequency range is from 100 MHz to 1.5 GHz. Fig. A.7 shows the proposed methodology where the two loop antennas are placed around the femur region (from ANSYS Human Body Model). Fig. 6.8 shows the location of the excitation for each antenna and copper conductor strips which form the structure of the model.

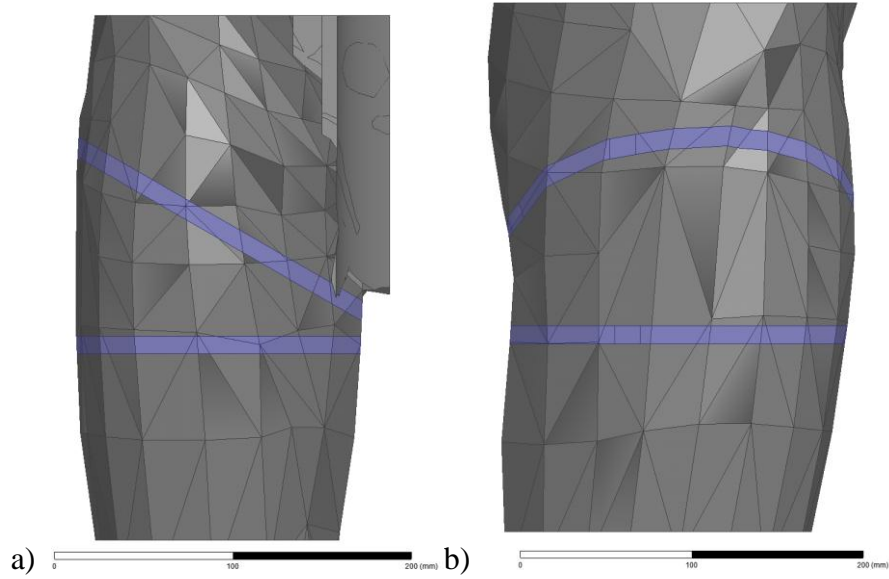


Fig.6.7. a) - 3D Front view of the selected region of the thigh depicting the antennas around the femur of an individual under examination. B) - 3D Profile view of the selected region of the thigh depicting the antennas around the femur of an individual under examination.

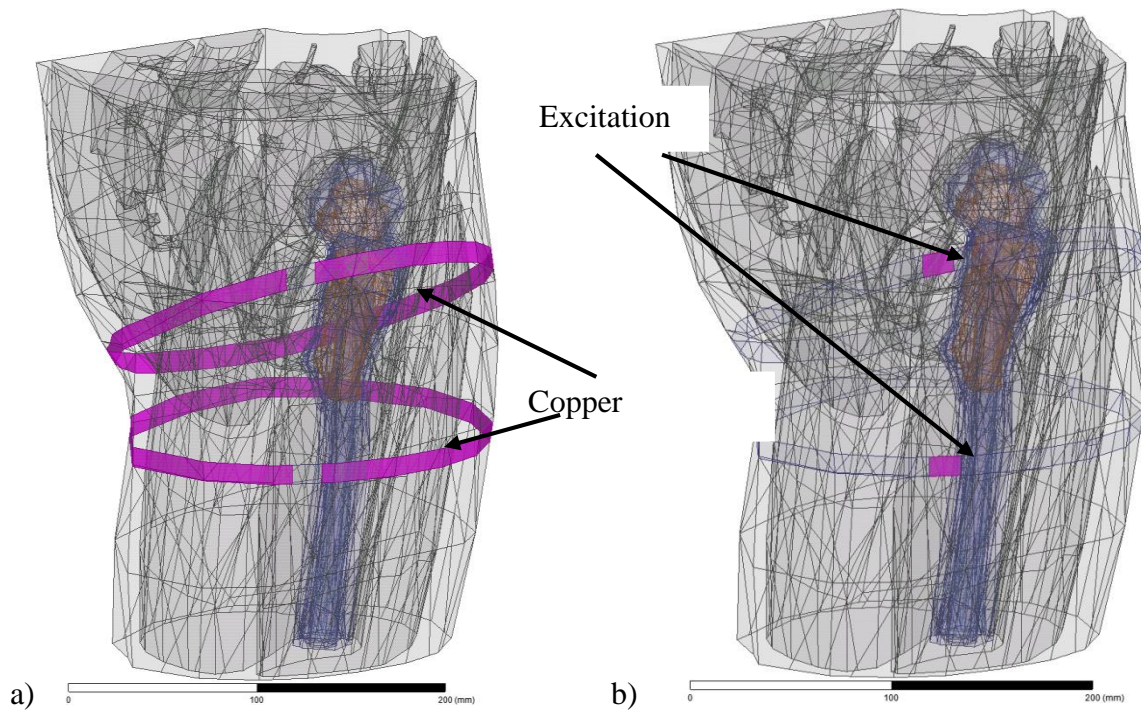


Fig. 6.8. a) - Side view of copper conductor surrounding human thigh. B) - Side view of excitation on the sheet surrounding human thigh.

Fig. 6.9 shows the plot which relates the  $S_{21}$  (dB) across the frequency sweep [9]. As anticipated the resonance frequency of the osteoporotic case shifts owing to the change in material properties. Standard\_H depicts the healthy case and Standard\_O depicts the osteoporotic case.

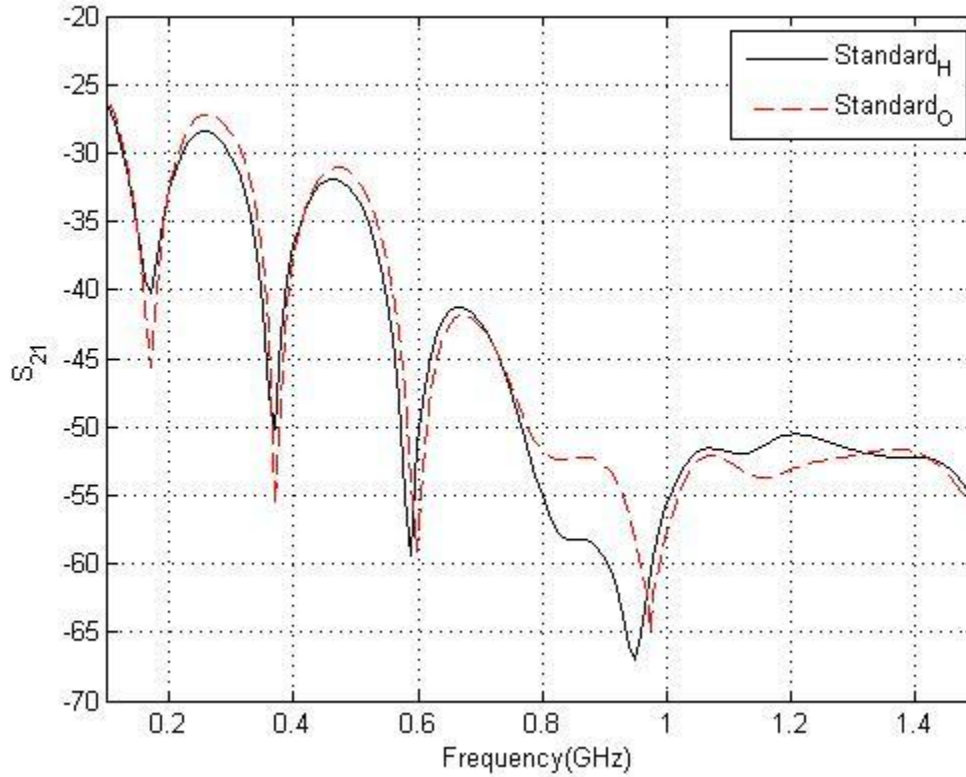


Fig.6.9. Resonant frequency behavior of standard human tissues for healthy and osteoporotic cases.

All the discussed techniques are in initial stages of development and would require working prototypes to validate the idea and its working.

### 6.3. Other applications

The VHP Female phantom has recently been used for RF modeling of CW fields around and within the human head [10]. The following problem has been addressed: find the ideal radio-frequency path through the brain for a given receiver position located on the top of the sinus cavity. The two parameters, transmitter position and radiating frequency, should be optimized simultaneously such that (i) the propagation path through the brain is the longest; and (ii) the received power is maximized. To solve this problem, we have performed a systematic and comprehensive study of the electromagnetic fields excited in the head by small on-body magnetic dipoles (coil antennas). The base radiator is constructed of two orthogonally oriented magnetic dipoles excited in quadrature, which enables us to create a directive beam into the head, as this novel antenna type generates a beam at 45 degrees into a dielectric interface. The CSF and ventricles inside the head form what approximates a dielectric waveguide to channel this beam into the sinus cavities. We

have found at least one optimum solution. This solution implies that a distinct RF channel may be established in the brain at a certain frequency and transmitter location. In addition to microwave tomography of the human body, such an antenna can potentially be used to screen for detrimental conditions such as Alzheimer's disease.

The VHP – Female model can be also used for many other applications and research work. As mentioned in Chapter 1, the model can be used for SAR studies and now can also be used for simulation the VHP – Female model in a whole body MRI coil. Also, development of deformable model with variable BMI and flexible limbs would be future initiatives to broaden the scope of utilization. The expansion of inventory, for example, the reproductive system, endocrine and exocrine gland systems would be also planned. Applications related to Body Area Networks can also be studied using the VHP – Female model. The range of applications is wide and is open to researchers around the globe to utilize it for their respective studies.

## References

- [1] Barry Gordon, (2012, May 14) , Transcranial Direct Current Stimulation (tDCS) and Cognitive Processing Online: <http://clinicaltrials.gov/show/NCT01602263>
- [2] ALTRUA™ 60 Pacing System, Online: [http://www.bostonscientific.com/content/dam/bostonscientific/ep/portfolio-group/C2-180-0409\\_ALTRUA60\\_specsheet.pdf](http://www.bostonscientific.com/content/dam/bostonscientific/ep/portfolio-group/C2-180-0409_ALTRUA60_specsheet.pdf)
- [3] J.P. Dmochowski, A. Datta, M. Bikson, Y. Su, L.C. Parra, “Optimized multi-electrode stimulation increases focality and intensity at target,” *J. Neural Eng.*, p. 046011, August 2011.
- [4] Rampersad SM, Janssen AM, Lucka F, Aydin U, Lanfer B, Lew S, et al. Simulating transcranial direct current stimulation with a detailed anisotropic human head model. *IEEE Trans Neural Syst Rehabil Eng.*, vol 22, no 3, pp.441–52, May 2014.
- [5] IT'IS Material Property Database, Retrieved Oct. 2nd 2013 from <http://www.itis.ethz.ch/itis-for-health/tissue-properties/overview/>
- [6] R.Harikumar, R.Prabu, S.Raghavan, “Electrical Impedance Tomography (EIT) and Its Medical Applications: A Review”, *Int. J. of Soft Computing and Eng. (IJSCE)*, vol 3, pp 193- 98, September 2013.
- [7] D.C. Barber and B.H. Brown, “Applied potential tomography,” *J. Phy. E: Sci. Instrum.* vol. 17, 1984, pp. 723-733.
- [8] H. Griffiths, “Magnetic induction tomography,” *Meas. Sci. Technol.*, vol. 12, no. 8, pp. 1126–1131, Aug. 2001.
- [9] M. R. Kamarudin, Y. I. Nechayev, and P. S. Hall, “Performance of antennas in the on-body environment,” in *Proc. IEEE Antennas Propag. Soc. Int. Symp.*, vol. 3A, pp. 475–478, Jul. 3–8, 2005.
- [10] J.M. Elloian, G.M. Noetscher, S.N. Makarov, A. Pascual-Leone, “Continuous wave simulations on the propagation of electromagnetic fields through the human head”, *IEEE Trans. Biomedical Engineering*, vol. 61, no. 6 (June 2014) 1676-1683.

# Summary

- 1) I created a significant part (up to 40%) of the VHP-F raw and processed triangular surface meshes.
- 2) Based on the computational phantom, I performed numerical study of cephalic versus extracephalic electrode configuration in the cranium and established new and important advantages of the extra cephalic configuration.
- 3) I developed MATLAB-based mesh processing tools including new modifications of the existing mesh intersection algorithm.



## Appendix A –

# Direct Current Flow - Boundary conditions and integral equations

### A.1.1 Boundary conditions for a conducting body

Theory of DC conduction currents in volumetric conductors is the well-established subject of research – see, for example, Ref. [1]. Consider a conducting body #1 with conductivity  $\sigma_1$  and with three attached electrodes – see Fig. A-1. The body may contain some inner boundaries, which correspond to subvolumes (or subbodies) #2 and #3 with other values of the conductivity:  $\sigma_2$  and  $\sigma_3$ , respectively. The outer normal vector to the body surface,  $\mathbf{n}_1$ , is shown in Fig. A-1. For inner boundaries, the normal vector will be always pointing from the main volume to the subvolume. The body #1 is located in vacuum (air). The dielectric permittivity of the body is irrelevant in the DC steady state.

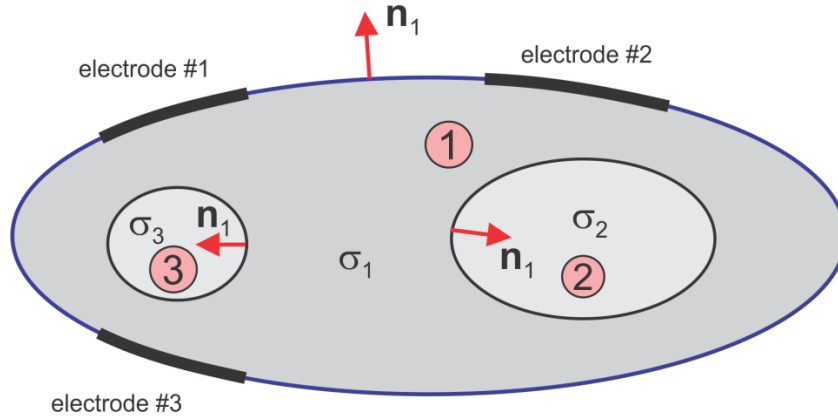


Fig. A-1. Evaluation of boundary condition for a conducting body with attached electrodes.

Consider the body surface in contact with air or with a subvolume. Everywhere on the body surface, the normal component of the electric current density,  $\mathbf{j} = \sigma \mathbf{E}$ , measured in A/m<sup>2</sup> shall be continuous across the boundary. Otherwise, the charges will constantly accumulate at the boundary, which is impossible. Therefore, the required boundary conditions in Fig. A-1 become

$$\begin{aligned} \sigma_1 \mathbf{n}_1 \cdot \mathbf{E}_1(\mathbf{r}) - \sigma_{\text{air}} \mathbf{n}_1 \cdot \mathbf{E}_{\text{air}}(\mathbf{r}) &= 0, & \mathbf{r} \in S_{\text{body}\#1\text{air}} \\ \sigma_1 \mathbf{n}_1 \cdot \mathbf{E}_1(\mathbf{r}) - \sigma_2 \mathbf{n}_1 \cdot \mathbf{E}_2(\mathbf{r}) &= 0, & \mathbf{r} \in S_{\text{body}\#1\text{body}\#2} \\ \sigma_1 \mathbf{n}_1 \cdot \mathbf{E}_1(\mathbf{r}) - \sigma_3 \mathbf{n}_1 \cdot \mathbf{E}_3(\mathbf{r}) &= 0, & \mathbf{r} \in S_{\text{body}\#1\text{body}\#3} \end{aligned} \quad (\text{A-1})$$

Since the air conductivity is clearly zero, the boundary condition at the conductor-air interface simplifies to  $\sigma_1 \mathbf{n}_1 \cdot \mathbf{E}_1(\mathbf{r}) = 0$ .



Eq. (A-1) implies that the normal electric field is discontinuous across every boundary between regions of different conductivity. This means that there is always *free charge density*,  $\sigma_F(\mathbf{r})$ , that resides on those boundaries. There is also free charge density,  $\sigma_F(\mathbf{r})$ , on the electrode surfaces. The rest of the volume is *electrically neutral* while the electric current density,  $\mathbf{j}$ , exists everywhere within the volume with a non-zero conductivity.

### A.1.2 Integral equations for a conducting body except on electrode surfaces

The entire surface of the body in Fig. A-1 including outer boundary, inner interfaces, and the electrode surfaces will be denoted by  $S$ . The electric potential due to the free surface charge density on  $S$  becomes

$$\varphi(\mathbf{r}) = \int_S \frac{\sigma_F(\mathbf{r}') dS'}{4\pi\epsilon_0 |\mathbf{r} - \mathbf{r}'|} \quad (\text{A-2})$$

The total electric field everywhere in the conducting volume or in free space surrounding that volume is given by

$$\mathbf{E}(\mathbf{r}) = -\nabla\varphi(\mathbf{r}) = -\int_S \frac{\sigma_F(\mathbf{r}')}{4\pi\epsilon_0} \nabla \frac{1}{|\mathbf{r} - \mathbf{r}'|} dS' \quad (\text{A-3})$$

where  $\epsilon_0$  is the dielectric constant of vacuum. Taking the limit of Eq. (A-2) as  $\mathbf{r}$  approaches the surface  $S$  we may find that this limit will be different if  $\mathbf{r}$  approaches  $S$  from *inside* (medium #1) or from *outside* (medium #2, #3, or air). This property of the integral (A-3) is well known in mathematical physics, where the integral in Eq. (A-3) is known as a *double layer potential* [2]. The physical meaning is that the normal component of the electric field indeed undergoes a break when passing through an infinitesimally thin layer of charges. With reference to Fig. A-1, one has for two limiting values [2]

$$\begin{aligned} \mathbf{E}_{\text{justinsidebody\#1}}(\mathbf{r}) &= -\int_S \frac{\sigma_F(\mathbf{r}')}{4\pi\epsilon_0} \nabla \frac{1}{|\mathbf{r} - \mathbf{r}'|} dS' - \mathbf{n}_1 \frac{\sigma_F(\mathbf{r})}{2\epsilon_0} \\ \mathbf{E}_{\text{justoutsidebody\#1}}(\mathbf{r}) &= -\int_S \frac{\sigma_F(\mathbf{r}')}{4\pi\epsilon_0} \nabla \frac{1}{|\mathbf{r} - \mathbf{r}'|} dS' + \mathbf{n}_1 \frac{\sigma_F(\mathbf{r})}{2\epsilon_0} \end{aligned} \quad \mathbf{r} \in S \quad (\text{A-4a})$$

The normal component of the electric field at both sides of the boundary is of interest, that is,

$$\begin{aligned} \mathbf{n}_1 \cdot \mathbf{E}_{\text{justinsidebody\#1}}(\mathbf{r}) &= -\left( \mathbf{n}_1 \cdot \int_S \frac{\sigma_F(\mathbf{r}')}{4\pi\epsilon_0} \nabla \frac{1}{|\mathbf{r} - \mathbf{r}'|} dS' \right) - \frac{\sigma_F(\mathbf{r})}{2\epsilon_0} \\ \mathbf{n}_1 \cdot \mathbf{E}_{\text{justoutsidebody\#1}}(\mathbf{r}) &= -\left( \mathbf{n}_1 \cdot \int_S \frac{\sigma_F(\mathbf{r}')}{4\pi\epsilon_0} \nabla \frac{1}{|\mathbf{r} - \mathbf{r}'|} dS' \right) + \frac{\sigma_F(\mathbf{r})}{2\epsilon_0} \end{aligned} \quad \mathbf{r} \in S \quad (\text{A-4b})$$

We further plug Eqs. (A-4b) into the boundary condition given by Eq. (A-1). The result has a form of an integral equation for the unknown bound surface charge density,  $\sigma_F(\mathbf{r})$  on a conductor-conductor (or conductor-air) interface,

$$\frac{\sigma_F(\mathbf{r})}{2\varepsilon_0} + \frac{\sigma_1 - \sigma_{\text{outside}}}{\sigma_1 + \sigma_{\text{outside}}} \left( \mathbf{n}_1 \cdot \int_S \frac{\sigma_F(\mathbf{r}')}{4\pi\varepsilon_0} \nabla \frac{1}{|\mathbf{r} - \mathbf{r}'|} dS' \right) = 0 \quad \mathbf{r} \in S, \text{ but not on electrode surface} \quad (\text{A-5})$$

Here,  $\sigma_{\text{outside}} = \sigma_2, \sigma_3$ , or 0 depending on the boundary. Note that the factor  $\varepsilon_0$  may be canceled out; it is only kept for convenience.

### ***A.1.3 Complete integral equations for a conducting body. Dirichlet and Neumann boundary conditions***

Eq. (A-5) is incomplete as it does not specify the boundary conditions on the electrode surfaces. Three possible cases for those boundary conditions are shown in Fig. A-2.

#### ***A. Voltage power sources or Dirichlet boundary conditions***

In the first case – Fig. A-2a – the boundary conditions imply the use of a voltage power supply (or supplies). The value of the electric potential (voltage),  $\varphi = V_1, V_2$ , or  $V_3$  is to be given for every electrode surface. One has, according to Eq. (A-2)

$$\varphi(\mathbf{r}) = \int_S \frac{\sigma_F(\mathbf{r}') dS'}{4\pi\varepsilon_0 |\mathbf{r} - \mathbf{r}'|} = V_{1,2,3} \quad \mathbf{r} \in \text{electrode surfaces \#1, \#2, and \#3} \quad (\text{A-6a})$$

Eqs. (A-5) and (A-6a) constitute the complete set of integral equations. All boundary conditions on all surfaces/interfaces are thus defined. Eq. (A-6a) is known as the *Dirichlet boundary condition* – the electric potential (the unknown function) is given at the electrode boundaries.

#### ***B. Constant-current density power sources or Neumann boundary conditions***

In the second case – Fig. A-2b – we specify the current sources – current power supplies. Every electrode is characterized by the total current,  $I = I_1, I_2$ , or  $I_3$ . Indeed, it must be  $I_1 + I_2 + I_3 = 0$ . Knowing electrode areas gives the prescribed current densities,  $j_1 = I_1 / A_1$ ,  $j_2 = I_2 / A_2$ ,  $j_3 = I_3 / A_3$ . Therefore,

$$\sigma_1 \mathbf{n}_1 \cdot \mathbf{E}_{\text{just inside body \#1}}(\mathbf{r}) = \sigma_1 \left[ - \left( \mathbf{n}_1 \cdot \int_S \frac{\sigma_F(\mathbf{r}')}{4\pi\varepsilon_0} \nabla \frac{1}{|\mathbf{r} - \mathbf{r}'|} dS' \right) - \frac{\sigma_F(\mathbf{r})}{2\varepsilon_0} \right] = j_i \quad i = 1, 2, 3 \quad (\text{A-6b})$$

where the constant normal current density  $j_i$  is taken positive when the current leaves body #1 and negative otherwise. Eqs. (A-5) and (A-6b) again constitute the complete set of integral equations. All boundary conditions on all surfaces/interfaces are now defined.

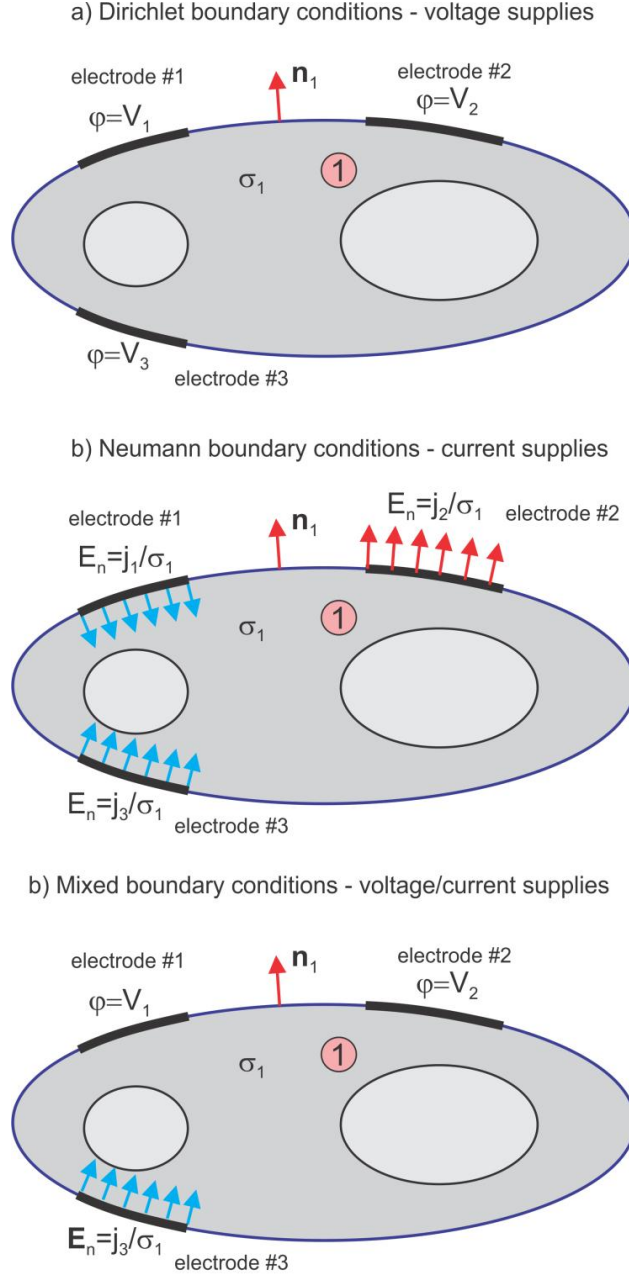


Fig. A-2. Different boundary conditions at the electrode surfaces.

Eq. (A-6b) is known as the *Neumann boundary condition* – not the electric potential but *its normal derivative* (normal electric field) is given at the electrode boundaries. The Neumann boundary conditions result in a simpler formulation for the present problem than the Dirichlet boundary conditions. In the particular, yet important case of electrodes on the air-conductor boundary, Eqs. (A-5), (A-6b) may be rewritten in the form:

$$\begin{aligned}
\frac{\sigma_F(\mathbf{r})}{2\epsilon_0} + K \left( \mathbf{n}_1 \cdot \int_S \frac{\sigma_F(\mathbf{r}')}{4\pi\epsilon_0} \nabla \frac{1}{|\mathbf{r} - \mathbf{r}'|} dS' \right) &= 0 \quad \mathbf{r} \in S, \text{ but not on electrode surface} \\
\frac{\sigma_F(\mathbf{r})}{2\epsilon_0} + K \left( \mathbf{n}_1 \cdot \int_S \frac{\sigma_F(\mathbf{r}')}{4\pi\epsilon_0} \nabla \frac{1}{|\mathbf{r} - \mathbf{r}'|} dS' \right) &= -j_i / \sigma_1 \quad \mathbf{r} \in \text{electrode surfaces \#1, \#2, \#3}
\end{aligned} \tag{A-6c}$$

Here,  $K = (\sigma_1 - \sigma_{\text{outside}}) / (\sigma_1 + \sigma_{\text{outside}})$  is the “conductivity contrast” at the boundary. For an air-conductor boundary, which is the electrode boundary,  $K = 1$ . Thus, all the integral equations are of the same kind; only the right-hand-side is different.

### C. Mixed power sources or mixed boundary conditions

In the last case – Fig. A-2c – we may specify the electrode voltages and electrode currents simultaneously. Some of the electrodes may be voltage-defined; some – current-defined. In that case, we use Eqs. (A-6a) or (A-6b) for every individual electrode. This formulation corresponds to the *mixed boundary conditions*: both the electric potential and its normal derivative (normal electric field) are given at the electrode boundaries.

### D. Practical constant-current electrodes

Neumann boundary conditions represent the ideal hypothetic current electrodes. Voltages across the surface of such electrodes will change. This is not the case for any metal or well-conducting electrodes in practice, which are subject to a constant voltage. Therefore, the current-injection sources are often modeled in a different way. We still use Dirichlet boundary conditions of a fixed surface electrode voltage. However, after completing the simulations, the required total current may be related to voltage and vice versa. A user can define the total current *a priori*, which is the typical current source implementation. The well-known current singularity at the voltage electrode edges may be eliminated via matching sponges. The current sources in MAXWELL 3D of ANSYS are implemented exactly in the same form.

### E. Current singularity for voltage electrodes

Constant-voltage electrodes produce current singularity of the type  $1/\sqrt{(a^2 - r^2)}$  at its edges. For an analytical solution, please see Ref. [4]. The charge density experiences a similar singularity.

## References

- [1]. W. R. Smythe, *Static and Dynamic Electricity*, McGraw Hill, New York, 1950, Chapter 6.
- [2]. R. Courant and D. Hilbert, *Methods of Mathematical Physics*, Volume II, Wiley-Interscience, New York, 1962.
- [3]. C. A. Balanis, *Advanced Engineering Electromagnetics*, Wiley, New York, 2<sup>nd</sup> Ed., 2012.
- [4]. J. D. Wiley and J. G. Webster, “Analysis and Control of the Current Distribution under Circular Dispersive Electrodes,” *IEEE Trans. Biomedical Engineering*, vol. BME-29, no. 5, May 1982.